Nanofluidic Coupled Membrane Devices for Single Molecule Sensing and Imaging

Yuning Zhang

Supervised by Dr. Walter Reisner

Doctor of Philosophy

Department of Physics

McGill University

Montreal, Quebec

July, 2017

A Dissertation Submitted to the Faculty of Graduate Studies in Partial Fulfillment of the Requirements for the Degree of Doctor of Philosophy

DEDICATION

⌈ This dissertation is dedicated to my beloved parents and my angel.

Thanks for everything! ⌋

ACKNOWLEDGEMENTS

This work would not have been possible without the encouragement and generous help from many people. First and foremost, I would like to thank my supervisor Prof. Walter Reisner. His careful instruction and acute intuitive insight into physics guided me through my Ph.D. I sincerely appreciate the help from my co-supervisors over different projects: Prof. Michael Hilke with the graphene related projects, Prof. Robert Sladek with the graphene in *situ* TEM liquid cell project, Prof. Peter Grutter with the AFM nanopore project, from whom I gain not only wisdom but also the passion and spirit of science. I would like to thank Wayne Yang, who worked with me for more than three years on the graphene related projects, Carlos Ruiz-Vargas and Martin Lee, who helped me with the TEM graphene encapsulation experiment. I would like to thank Yoichi Miyahara who provided me enormous help with the AFM nanopore project. I would also like to thank the other members of the Reisner group, Alexander Klotz, Ilja Czolkos, Ahmed Khorshid, Sara Mahshid, Philip Zimny, Mohammed Jalal Ahamed, Susan Amin and Yi Cao for providing me invaluable help during my Ph.D years. I am enormously indebted to the McGill Nanotools staffs, who provided me systematic training on the micro/nanofabrication tools. I also deeply appreciate Jean-Philippe Masse from $(CM)^2$, David Liu and other staffs from FEMR who offered me training on scanning electron microscope and transmission electron microscope. Sincere thanks to the doctoral committee members, who devoted their time and energy in correcting my dissertation. Lastly, I wish to thank all of my friends, from whom I received ultimate loving support.

ORIGINALITY AND CONTRIBUTION

This dissertation includes the work I have done at McGill university over the past four and half years. The dissertation is written in the publication based format, including four manuscripts (two published and two ready for submission).

❄ Chapter 1 – a general introduction with motivations.

❄ Chapter 2 – background.

❄ Chapter 3 – a published manuscript on nanopore embedded nanofluidic devices:

Nanopore Embedded Nanofluidic Devices for Single-molecule DNA Analysis and Manipulation

Yuning Zhang and Walter Reisner, Nanotechnology 26, no. 45 (2015): 455301.

❄ Chapter 4 – a manuscript on AFM nanopore fabrication ready for submission:

Nanopore Fabrication via Conductive Atomic Force Microscope based Dielectric Breakdown

Yuning Zhang, Yoichi Miyahara, Peter Grutter and Walter Reisner.

❄ Chapter 5 – a published manuscript on graphene liquid cell for SEM:

Dynamic Imaging of Au-nanoparticles via Scanning Electron Microscopy in a Graphene Wet Cell

Wayne Yang[†], Yuning Zhang[†], Michael Hilke, and Walter Reisner, Nanotechnology 26, no. 31 (2015): 315703. ([†] equal contribution)

❄ Chapter 6 – a manuscript on in *situ* TEM graphene liquid cell ready for submission:

Micron Scale Graphene Liquid Cell for in *situ* Transmission Electron Microscopy

Yuning Zhang, Martin Lee, Carlos Ruiz-Vargas, Wayne Yang, Robert Sladek, Michael Hilke and Walter Reisner.

❄ Chapter 7 – Conclusion.

The work included in this dissertation mainly focuses on innovations and applications in the nanopore/nanofluidics and graphene liquid cell field. It includes:

A project on nanopore embedded nanofluidics, which pioneers the integration of nanopore structure into complex nanochannel systems for single-molecule DNA analysis. The research is published on Nanotechnology in 2015 with myself as the first author under the supervision and guidance of Prof. Walter Reisner.

A project on nanopore fabrication via conductive AFM assisted dielectric breakdown. This technique combines the nanometer positioning, surface characterization capability of AFM and simplicity of the dielectric breakdown method. The manuscript for this research is ready for submission with myself as the first author. The subject of this work is covered under a provisional patent:Yuning Zhang, Yoichi Miyahara, Peter Grutter, Walter Reisner. "METHOD AND APPARATUS FOR MAKING A NANOPORE IN A MEMBRANE USING AN ELECTRIC FIELD APPLIED VIA A CONDUCTIVE TIP." U.S. Provisional Patent No. 62/507,502, May 17th, 2017. Both Dr. Yoichi Miyahara and myself contributed to the AFM experiments. I performed the data analysis and wrote the manuscript. This project is under the supervision and guidance of Prof. Peter Grutter and Prof. Walter Reisner.

A project on graphene liquid cell for SEM, which demonstrated the successful development of a graphene liquid cell for SEM, enabling real time imaging of nanoparticles undergoing diffusive motion in aqueous solution in liquid. This research is published on Nanotechnology in 2015 with myself as the co-first author. Both Wayne Yang and me contributed to the liquid cell experiments and data analysis. Wayne Yang wrote the manuscript. This project is under the supervision and guidance of Prof. Michael Hilke and Prof. Walter Reisner.

A project on graphene liquid cell for TEM, which demonstrated the successful development of a micron-sized graphene liquid cell for TEM. The graphene liquid cell

enabled real time imaging of nanoparticles and nanoparticle-DNA conjugates undergoing diffusive motion in aqueous solution under nano-confinement. In this research we observed dramatic slowing down of nanoparticle diffusive movement under confinement as well as a broad distribution of the particle diffusion coefficients. We proposed a sandwich model to describe the liquid layer, which is possibly the physical origin of our experimental observations. The manuscript for this research is ready for submission with myself as the first author. Wayne Yang, Martin Lee, Carlos Ruiz-Vargas and myself contributed to the experiments. Martin Lee and myself contributed to the data analysis. I wrote the manuscript. This project is under the supervision and guidance of Prof. Robert Sladek, Prof. Michael Hilke and Prof. Walter Reisner.

ABSTRACT

We developed a nanopore embedded nanofluidic device for single-molecular DNA analysis and manipulation. Utilizing the nanofluidic device, we pre-stretched ds-DNA molecules in nanochannel (quasi-1D confinement) and successfully translocated and recaptured DNA molecules through the nanochannel embedded nanopore.

We developed a novel nanopore fabrication technique based on conductive atomic force microscopy and dielectric breakdown. We demonstrated the successful fabrication of single nanopore/nanopore array on thin nitride membranes in ambient conditions. We have also developed a model to explain the pore formation mechanism.

We developed two different graphene liquid cells for both scanning electron microscopy and transmission electron microscopy. With the new liquid cells, we are able to record real-time nanoparticle dynamics in aqueous conditions under both SEM and TEM. The dramatic slowing down of nanoparticle diffusive movements are observed and analyzed for nanoparticles under nano-scale confinement.

ABRÉGÉ

Nous avons développé un nanofluidic nanopore encastré pour l'analyse et la manipulation de l'ADN moléculaire unique. En utilisant les dispositifs nanofluidiques, nous avons pré-étiré les molécules d'ADN-d dans les nanochannels, sous confinement quasi-1D, et transposé et recapturé avec succès des molécules d'ADN à travers le nanopore nanochannel embarqué.

Nous avons développé une nouvelle technique de fabrication nanopore basée sur la microscopie de force atomique conductrice et la rupture diélectrique. Nous avons démontré la fabrication réussie de réseaux nanopore / nanopore sur des membranes minces de nitrure avec un positionnement de précision nanométrique dans des conditions ambiantes. Le mécanisme de formation de pores est également discuté en détails.

Nous avons développé deux différentes cellules de liquide de graphène pour la microscopie électronique de balayage et la microscopie électronique de transmission. Avec ces techniques, nous sommes en mesure d'enregistrer en temps réel la dynamique des nanoparticules dans des conditions aqueuses à la fois avec SEM et TEM. Le ralentissement spectaculaire des mouvements diffusifs des nanoparticules est observé et analysé pour les nanoparticules sous confinement nanométrique.

TABLE OF CONTENTS

LIST OF TABLES

LIST OF FIGURES

CHAPTER 1
Introduction

1.1 Introduction

Over the past decade, nanochannel coupled membrane devices have become an increasingly important application area in nanofluidics due to their great potential in single molecule sensing and imaging [1, 2]. Nanofluidic coupled membrane devices include a broad range of structures such as solid state nanopores, biological nanopores and graphene based liquid cells. Solid state nanopores on thin membranes (e.g. SiN_x, SiO_2, Al_2O_3 and graphene) are an effective approach for single molecule DNA sensing [3], protein detection [4] and microRNA characterization [5]. Graphene based liquid cells enable electron microscopy to be applied in fluid environments and have been successfully applied for a range of studies in materials science and characterization of biological samples, including studying colloidal nanocrystal growth [6], Au-nanoparticle conjugates [7] and wet biological samples (viruses and cells) [8]. The combination of nanofluidic features (e.g. nanopores, nanochannels) with thin membranes (e.g. silicon nitride membrane, single layer graphene) gives rise to a broad range of novel systems with unique properties and application possibilities. Application possibilities include the capability to combine transverse nanofluidic devices with electrical sensing capability, extract analytes from a nanoconfined environment into a large microchannel reservoir, perform high signal electronic imaging in a liquid environment and finally modify the local chemical environment inside a nanofluidic channel via buffer exchange

through a large macroscopic reservoir interfaced to the channel via an array of nanoscale membrane embedded pores.

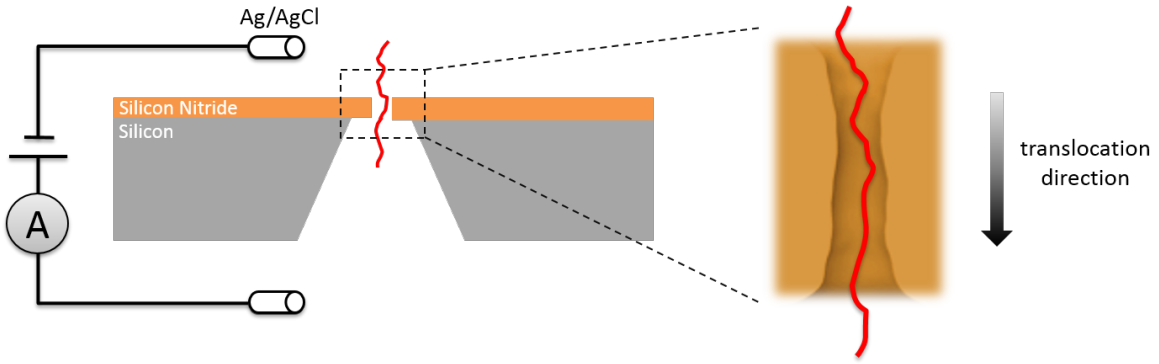

Figure 1–1: The diagram of a conventional solid state nanopore (silicon nitride) for DNA sensing. A voltage bias is applied across the electrolyte through a pair of Ag/AgCl electrodes creating a local high electric field across the nanopore ($\sim 10^6$ V/m). DNA molecules which are negatively charged are captured by the e-field and translocate through the pore.

This dissertation summarizes my work including four different research projects. Each project lead to a successful application or technique, which is written as an individual chapter in my dissertation. This dissertation is divided into seven chapters. Chapter 1 is a general introduction and motivations. Chapter 2 is the background. Chapter 3 summarizes the nanopore/nanochannel project. Chapter 4 summarizes the AFM nanopore project. Chapter 5 summarizes the SEM graphene liquid cell project. Chapter 6 summarizes the TEM graphene liquid cell project. Chapter 7 provides a conclusion and perspective.

1.2 Motivation for Nanopore embedded Nanofluidic Devices

A nanopore, defined as a small hole with an internal diameter of the order of 1-10 nm, is becoming one of the most promising candidates for bio-molecular sensing and next generation sequencing technologies. Nanopore detectors work on the principle of ionic current blockade or Coulter-counter effect [9, 10]: the bio-polymer threading

through the pore creates a transient decrease in the trans-pore ionic current. By analyzing the current traces due to the translocating molecules, nanopore detectors can obtain the molecular conformation [11] and structural and chemical properties of the transiting biomolecules [12].

Even though nanopore based devices have proven to be very effective and promising candidates for biomolecular sensing, a major unsolved problem is the rapid translocation speed of DNA molecules through the nanopore. Because of the ultra fast translocation speed (1-3 μs per base pair), there is an unfavorable trade-off between signal and sequence resolution [13]. Even with the most advanced commercially available nanopore sequencing device MinION from Oxford Nanopore, researchers reported an error rate of 38.2% after re-sequencing three bacterial genomes [14], which is not optimal for both industrial and academic level applications.

Achieving translocation slow-down is a major objective of nanpore research. Various approaches have been attempted, including reducing traslocation voltage [3], increasing buffer viscosity [15], increasing salt concentration [16] and decreasing the solution temperature [15]. While slow-down has been achieved, the improved sensing resolution and accuracy is still not sufficient for single nucleotide level sequencing. In particular, these attempts did not solve the fundamental problem of 'entanglement' between translocation speed and sensing signal. For the traditional nanopore construct, there is only one voltage source which drives the DNA molecule through the pore, performing DNA 'translocation', as well as providing the voltage source for current/conductance measurement. Consequently, there is no independent control over translocation speed and sensing signal. Even though lower voltage allows lower translocation speed, the driven voltage need to be set above a critical value (usually in the order of 100 mV, depending on the buffer condition as well as constructs of

bio-molecules and nanopores). Below the critical value, the electric potential is insufficient to overcoming the entropic free energy barrier (the bending energy) of threading molecules through the nanopore tunnel. Furthermore, coiling and knotting of DNA molecules will also increase the critical voltage.

A different nanofluidic device concept, *nanochannels*, have also been proven to be a very powerful single molecular analysis tool. Nanochannels are simply long nanoscale channels, typically with diameter in the 30-100 nm range. Acting as a quasi-1D confinement, nanochannels are able to stretch DNA molecules close to their full extension [17]. Nanochannel devices combined with enzymatic or denaturation-based barcoding techniques provide a powerful approach for high-through genomic mapping [18]. DNA molecules confined in nanochannels are usually analyzed via high-resolution fluorescent microscopy, an alternative sensing approaching to pore blockade based methods, but limited in sequence resolution (to around 1 kbp).

Devices combining nanopores with nanochannels may lead to various of new applications based on the ability to combine optical and blockage-based electrical detection methodologies. Direct visualization of the translocation process, as well as independent control over translocation speed and sensing signal, in principle should greatly improve the resolution and accuracy for bio-molecular sensing by slowing down DNA translocation speed. In addition to electrical bio-molecular sensing, the nanopore embedded nanofluidic devices also have various potential applications in the field of physics, chemistry and biology. From polymer physics point of view, the nanopore embedded nanochannel system is an unique system allowing the direct visualization of quasi-1D confinement to bulk transit of bio-molecules, with tunable threshold achieved by varying nanopore size. The nanopore-nanochannel device also has a "coarse filtering capability": a certain DNA molecule can be selected optically and pulled through the

nanopore to a spatially separated chamber. The selected molecule can then be further analyzed. For example, a DNA molecule selected coarsely on the basis of an optical barcode can be sequenced. This saves time and cost: it is much cheaper and faster to sequence a single small preselected region of the genome than the entire genome. Another potential application of nanopore embedded nanofluidic devices is that the nanoscale pore allows small molecules/ions to diffuse through the pore creating a local chemical environment inside the nanochannel that only affects molecules close to the pore. This might allow for localization of chemical reactions at molecular regions in the vicinity of the pore.

1.3 Motivation for AFM nanopore

Developing reliable, cost effective methods of making nanopores is of significant importance to the nanopore field. Biological nanopores, which are constructed by protein molecules, often have limited lifetimes due to the weak mechanical stability of the supporting lipid membrane. Biological nanopores also require dedicated experimental conditions (such as specific temperature and pH range) and have poor CMOS and micro/nanofluidic device compatibility. To over come this problem, researchers developed approaches for fabricating nanopores on artificial thin membranes (such as silicon nitride, silicon dioxide and graphene). These nanoscale pores on artificial thin membranes, referred to as "solid state nanopores", have outstanding mechanical and chemical stability. However, the main solid state nanopore production approaches (e.g. FIB and TEM milling) use high energy beam bombardment of substrate material. The high energy beam approaches are necessarily serial (one pore made at a time) and require expensive instrumentation, including high vacuum systems, increasing cost per pore and pore production times.

Recently, a simple method for fabricating nanoscale pore was proposed by Kwok *et al* [19]. By directly applying a voltage across an insulating membrane in electrolyte solution they were able to fabricate a single nanopore down to 2 nm in size through dielectric breakdown. While dielectric breakdown method can produce inexpensive and high quality nanopores, there are two key disadvantages: (1) the position of the nanopore is random, determined randomly by the inhomogeneity of the nitride films; and (2) this technique can not produce multiple nanopores or nanopore arrays consecutively, thus greatly reducing the yield.

In this dissertation we will present a novel method for nanopore fabrication combining the simplicity of dielectric breakdown as well as the nanoscale positioning and characterization capability of conductive atomic force microscopy. We will demonstrate the successful fabrication of nanopore/nanopore array on thin nitride membrane under ambient conditions with this technique.

1.4 Motivation for Graphene Liquid Cell

Silicon nitride liquid cells are mechanically strong, chemically inert, and also allow for modulation of several in *situ* environmental variables such as electric bias, temperature and pressure [2]. Yet, the fundamental resolution of nitride cells are limited to a few nanometers by the relatively thick (in the order of tens and hundreds of nanometers) viewing window as well as the relatively high atomic number of the material (silicon atomic number Z=14), giving rise to the scattering and poor beam transmission [2]. In 2012, researchers from Alivisatos group at UC Berkeley developed a new liquid cell technique [6]. Instead of using relatively thick amorphous membranes (typically silicon nitride or silicon dioxide) as the viewing window, they sandwiched small droplets (from 6 to 200 nm) between two single atom thick membranes – graphene – to fabricate a liquid cell. The new graphene liquid cell is straightforward to make as

graphene membranes are highly flexible, with outstanding mechanical tensile strength and impermeable to small molecules [20, 21], making them ideal for encapsulating gas, liquid and soft materials either for experiments in ambient or high vacuum conditions. In addition, graphene is reported to have excellent electrical conductivity that helps discharge the surface and reduce free electrons in the liquid cell leading to less electron radiolysis damage to the specimen [22]. High thermal conductivity of graphene (5300 $W \cdot m^{-1} \cdot K^{-1}$ [23]) will also help minimizing heating effects (e.g. liquid overheating, bubble generation) under electron beam.

The graphene liquid cell approach, over the past four years, has been used to study a broad range of systems including colloidal nanocrystal growth, 3D motion of DNA-Au nanoconjugates, growth dynamics and gas transport mechanism of nanobubbles, and wet biological samples (viruses and cells) [6, 7, 24, 8]. However, due to the fundamental limitation of the graphene liquid cell design, the cell size is limited to the range of 10-100 nm. Once the cell is extended to micron size, the free standing CVD grown graphene, containing multiple domains, can be easily broken due to the weakness introduced by grain boundaries, thus causing a liquid leakage in the high vacuum.

In this dissertation we will introduce new graphene liquid cell techniques for both SEM and TEM, which are proven to be novel, straightforward and effective platforms to study the dynamics of gold nanoparticles as well as DNA/gold nanoparticles conjugates. (chapter 5, graphene liquid cell for SEM; chapter 6, graphene liquid cell for TEM)

In Chapter 5, Graphene liquid cell for SEM, we will demonstrate that single layer CVD grown graphene is very promising for SEM based liquid cell imaging, enabling dynamic imaging of Au-NP undergoing Brownian motion in aqueous solution with a sub 5 nm resolution and EDX measurements in liquid. We are the first to record a

video of the Brownian motion of a Au nanoparticle in a micron wide graphene liquid cell using both secondary and backscattering electron mode.

In Chapter 6, Graphene liquid cell for TEM, we will first investigate multiple methods of labeling double-stranded DNA molecules. Furthermore, we will demonstrate the successful fabrication of micron-scale graphene liquid cell with the support of thin nitride grids, enabling dynamic imaging of free gold nanoparticles and DNA/gold nanoparticle conjugates.

In summary, we are motivated by the improvement of graphene liquid cell technology itself, providing a new technique of fabricating micron-scale graphene liquid cell with the support of nitride TEM grids. In addition, we are also interested in the fundamental physical science involved in the graphene liquid cell project: the direct visualization of nanoparticle diffusive dynamics in a EM liquid cell with nanometer resolution and the dramatic slowing down of nanoparticle diffusive motion under nanoscale confinement.

CHAPTER 2
Background

2.1 Introduction

Chapter 2 covers the general background related to this dissertation, including nanopores (chapter 3 and 4), nanofluidic devices (chapter 3), DNA (chapter 3 and chapter 6), polymer theory under confinement (chapter 3) and electron microscopy (chapter 5 and 6).

2.2 Nanopore

Currently, there are three types of nanopores: *solid state nanopores*, typically made by focused electron/ion beam in thin oxide or nitride films; *biological nanopores*, formed by pore-forming proteins [25], usually in the shape of a mushroom with a hollow core; and *hybrid nanopores*, constructed by coating the inner surface of a solid state nanopore with a functionalized lipid bilayer [26].

2.2.1 Solid State Nanopore

Solid state nanopores are the most interesting and widely researched nanopore structure, due to their straightforward fabrication, outstanding stability under different chemical environments, mechanical durability and CMOS and micro/nanofluidic system compatibility. Solid state nanopores are usually made on thin membranes such as silicon nitride, silicon dioxide and aluminum oxide. Graphene nanopore have also been explored [27] due to the potential improvement in sensing resolution by reducing

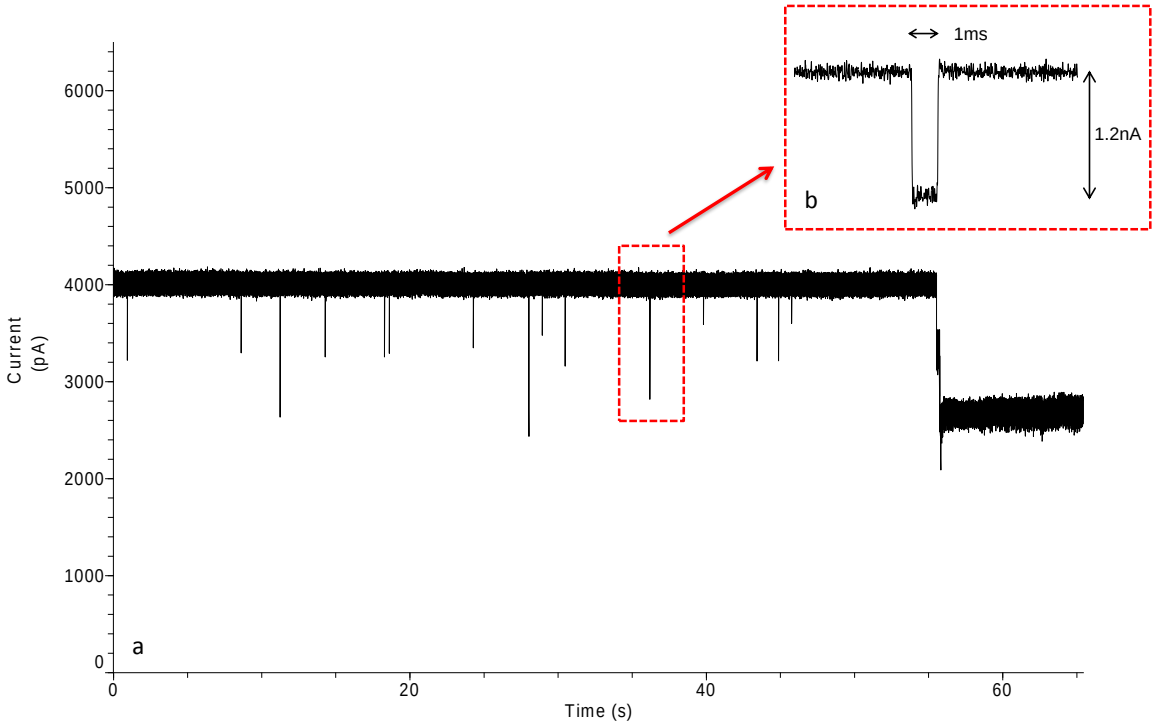

Figure 2–1: a) Voltage applied to the electrolyte through Ag/AgCl electrodes drives a flow of ions through the nanopore, resulting a baseline current trace. b) A transient dip in the trans-current trace, created while negatively charged DNA molecules driven through the pore, blocking the ions.

the membrane thickness to a single atomic sheet. There are three standard methods of fabricating a solid state nanopore:

High Energy Beam Drilling based on either ionic or electronic bombardment is by far the most widely used technique: In 2001, Golovchenko group at Harvard reported that 3 KeV Ar^+ beam focused to a nanoscale spot can be used to fabricate single nanopore in a thin silicon nitride membranes with true nanometer control [28]. Two years later, the Dekker group at Delft reported that focused electrons beams in a transmission electron microscope (TEM) can be used to make sub-10 nm holes in thin

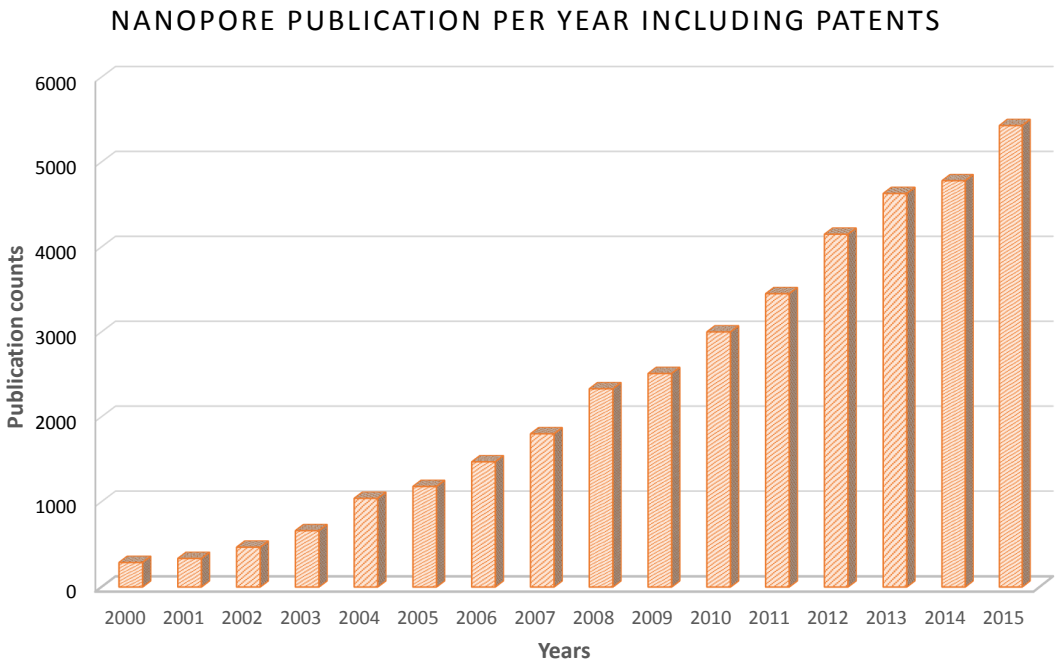

Figure 2–2: A 16-year trend of nanopore publication counts per year including patents, starting from 2000 to 2015. Data collected from google scholar.

nitride membranes. The pores made with this approach can be fine-tuned with sub nanometer precision by either focusing or spreading out the 200 keV electron beam [29]. Even though different energy beams are utilized for pore fabrication, both techniques share a similar mechanism: high energy e-beam or ion beam bombard the surface on the thin nitride film, knocking atoms away to create a nanometer-sized hole. The fine tuning of nanopore size is performed by locally "melting" the membrane material in the vicinity of the pore, this will expand nanopore size if the pore is greater than a critical initial size.

Wet chemical etching is an alternative fabrication technique that does not require high energy beams and is designed for the production of wafer scale nanopore arrays as well as for improved CMOS compatibility [30]. A typical wet-etch process begins

with standard photo/e-beam lithography to create micron-sized pattern arrays, and then is followed by an anisotropic wet etching process to create an inverted pyramid structure with a sharp apex at the bottom. Lastly, nanopores are created with an extra step of wet etching using alkaline solutions (TMAH(Tetramethylammonium hydroxide) or KOH) to thin down the substrate from the backside. The nanopore size can be controlled via monitoring the etching process through a custom made feed back system [30].

The *dielectric breakdown technique*, developed by the Tabard-Cossa group at University of Ottawa, is one of the most recently reported nanopore fabrication techniques [19]. In this approach, a voltage is applied across an insulating membrane immersed in conductive aqueous solution (eg. 1 M KCl). Driven by the electric field, structural defects inside the thin membrane will accumulate in a highly localized region, creating a conductive path that will result in physical damage to the membrane due to Joule power dissipation and resultant heating. This technique has been successfully used to fabricate nanopores below 2 nm in size. The dielectric breakdown technique is by far the easiest and cheapest pore fabrication technique as no high energy beams are required and experiments can be performed in ambient conditions.

2.2.2 Biological Nanopore

Pore-forming proteins used by bacteria to battle against rival bacteria and also to attack human cells, have the ability of punching nano-sized holes in target-cell membranes [25]. The biological nanopores constructed by pore-forming proteins, also called transmemebrane protein channels, are usually inserted into substrate such as planar lipid bilayers and liposomes. Compared with solid state nanopores, they have the advantages of well-defined size and structure, the capability of being easily modified and functionalized via molecular biology techniques, and can spontaneously form pores on

lipid bilayer supports via a self-assembly based process. However, biological nanopores are only stable in specific environment (e.g. specific ranges of salt concentration, pH and temperature) greatly shortening their lifetime as well as limiting their CMOS and micro/nanofluidic compatibility. Here are some of the more promising biological nanopores:

α-Hemolysin (α-HL, also called α-toxin) is a type of toxin secreted by *Staphylococcus aureus*, a type of bacterial frequently found in our nose, respiratory system and on our skin. The toxin binds with the cell membrane opens pores, and then kills the cell via osmotic swelling and rupture of the cell membrane. With the shape of a hollowed mushroom, α-Hemolysin consists of a 3.6 nm diameter cap and a 2.6 nm diameter transmembrane β-barrel [31]. It is also the first and most commonly used biological nanopore, currently adapted for commercial usage by Oxford Nanopore Technologies. The inner diameter of the α-Hemolysin is around 1.4 nm which is very close to the width of a single-stranded DNA molecule (1.3 nm), thus making α-Hemolysin an effective tool for analyzing biomolecular structures and interactions.

MspA (*Mycobacterium smegmatis* porin A) is a membrane porin produced by *Mycobacteria*. MspA allows hydrophilic nutrients to enter the bacterium and is the second most investigated biological nanopore for DNA sequencing. Due to the special funnel shape with a narrow and thin opening ($\sim$ 1.2 nm wide and 0.6 nm long) at the bottom of the interconnected octamer, MspA nanopores are reported to have an improved spatial resolution and accuracy for sequencing ssDNA [32]. In addition, MspA is also reported to remain robust under extreme experimental conditions, such as maintaining the temperature at 100C for 30 minutes and varying the pH from 0 to 14 [33].

Lastly, *Bacteriophage phi29* is another biological nanopore that has proven to be effective in molecular sensing. With a much larger inner diameter(3.6 nm), the phi29 nanopore enables the measurement of larger biomolecules, such as proteins, peptides, double-stranded DNA and DNA complexes. The large opening also enables molecular level modification and functionalization of the phi29 nanopore via insertion or conjugation of chemical groups [34].

2.2.3 Applications

Church, Deamer and Akeson proposed the concept of nanopore sequencing in the early 1990s [3] (shown in figure 2–3). Starting in 1996, with the first nanopore paper published in PNAS by the Deamer group [3], a whole new sensing technique for biomolecules - nanopore-based sensing - emerged and has became one of the most promising next generation sequencing technologies. While, the first and second generation sequencing techniques often require complex molecular labeling procedures for fluorescent detection, limiting maximum DNA length that can be sequenced (read-length), nanopore sequencing is label-free, high throughput and has potentially unlimited DNA read-length.

Single Nucleotides and Single-stranded DNA Detection

The very first nanopore DNA sequencing attempt was performed by Kasianowicz *et al.* in 1996 [3]. While they were not able to obtain resolution sufficient for distinguishing single nucleotides, they demonstrated that a phospholipid bilayer embedded α-Hemolysin nanopore could detect individual ssDNA and ssRNA molecules. In 2009, Clarke *et al.* from Oxford Nanopore Technologies Ltd, demonstrated that a modified α-Hemolysin nanopore (attaching an adapter inside the β-barrel) was able to identify unlabeled single nucleotides (dAMP, dCMP, dGMP, and dTMP) and even able to distinguish the 'fifth base', 5-methylcytosine, which could be useful in epigenetics for

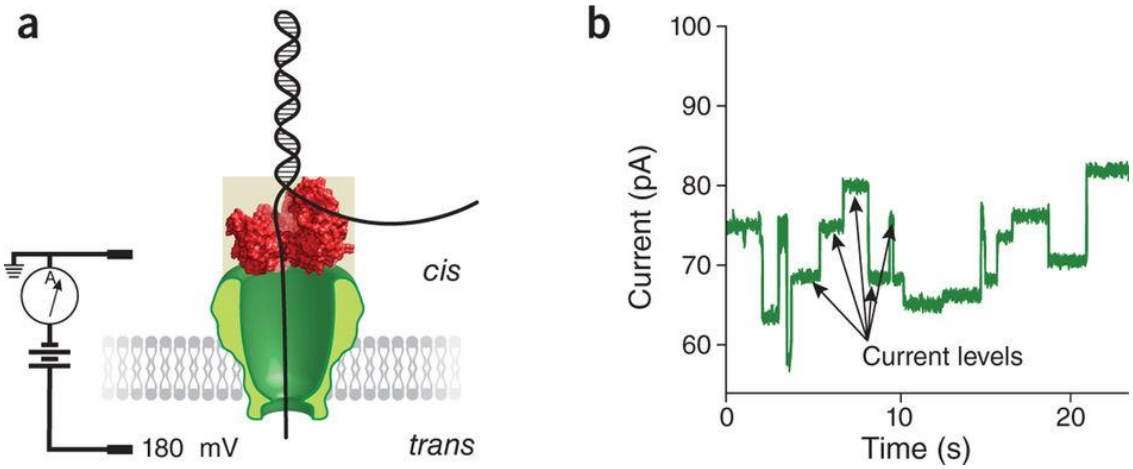

Figure 2–3: Nanopore sequencing. (a) A bias voltage is applied across the double lipid membrane which separates two chambers filled with electrolyte. The single-stranded DNA is electrophoretically driven through an MspA nanopore (green). The nanopore provides the only path through which ions and DNA can move across the membrane and entering different chambers. Translocation of the single-stranded DNA through the nanopore is controlled by an enzyme (red). (b) A recorded ionic current of single-stranded DNA translocating through a nanopore measured by a sensitive ammeter (pA level). Different current levels correspond to different bases (A, T, G, C) of the nucleotides. Exceptionally low ATP concentrations is applied to slow down the helicase activity (stepping rate), thereby increasing sequencing resolution. Figure adapted from [35].

the investigation of methylation patterns [36]. MspA, with the advantage of having a narrower and thinner opening inner channel, was also demonstrated to be a promising nanopore sensor for the purpose of DNA sequencing. In 2010, Derrington *et al.* reported that MspA nanopore can be used to distinguish all four DNA mucletides and resolve single nucleotides in single-stranded DNA while double-stranded DNA will temporarily pause the translocation and hold the nuclotides in the pore constriction [32].

Double-stranded DNA Detection

Even though α-Hemolysin and MspA nanopores are proven to be effective detectors

for small molecules such as single nucleotides, ssDNA and ssRNA, they have a limited channel size which makes the translocation of larger molecules (such as dsDNA and proteins) impossible. The bacteriophage phi29, however, has a minimum channel diameter of 3.6 nm that allows the detection of dsDNA and proteins. In 2010, Wendell *et al.* demonstrated that phi29 inserted in planar lipid bilayers were able to detect linear 5.5 kilobase plasmid DNA, allowing dsDNA translocation from the narrower to the wider-end of the pore [37]. Solid state nanopores, with tunable size, are also demonstrated to be capable of electronically characterize dsDNA molecules. The first solid state nanopore translocation experiment was performed by Li *et al.*. They successfully translocated DNA molecules through a 3 nm hole on 5-10 nm thick nitride film [11]. By analyzing the ionic current blockade induced by the DNA molecule they revealed the folding configuration of dsDNA molecules. Nanopores made in Al_2O_3 membranes have also been investigated for dsDNA translocation. In particular, Al_2O_3 nanopores made via atomic layer deposition are reported to have improved mechanical properties and much better noise performance over silicon nitride/silicon dioxide nanopores [38]. Furthermore, the average translocation speed of dsDNA through Al_2O_3 nanopores is an order of magnitude lower than for silicon based nanopores, greatly improved sensing resolution [39].

Protein Detection

In addition to DNA, a wide variety of substances have also been electronically characterized by nanopores, including cations [40], anions [41], microRNAs [5], peptides [42] and proteins [40]. Protein sequencing in particular is one of the most important topics for structural biology. Proteins are large biomolecules, consisting of one or more chains of amino acids. The sequence of amino acids is crucial for understanding the three-dimensional structure of proteins. Protein sequence can be potentially

determined using nanopore sensors. In 2008, Mohammad *et al.* demonstrated the successful translocation of single protein through an *alpha*-hemolysin nanopore [4]. In 2013, Nivala *et al.* demonstrated the enzymatic control of unfolding and translocation of proteins through *alpha*-hemolysin nanopore using the AAA+ unfoldase ClpX (a type of human enzyme unfolds protein) [43], a milestone for nanopore protein sequencing technology.

Challenges

Although nanopore sensors have been proven to be a very promising tool for sequencing, several issues remain unsolved. *Rapid translocation speed* of DNA molecules through the nanopore is one of the most fundamental and challenging problems. The typical translocation speed of DNA molecules is $\sim$ 1-3 μs per nucleotide, greatly limiting the resolution and accuracy of single nucleotide base identification measured via the single-channel recording technique [13]. Over the past decade, various strategies have been developed to slow down the translocation speed: modifying bio-nanopores [36, 13], reducing translocation voltage [3], increasing buffer viscosity [15], increasing salt concentration [16] and even decreasing the solution temperature [15]. Yet despite this significant work, the sensing resolution and accuracy improvement is still not sufficient for single base pair level sequencing. *Large-scale, cost-effective approaches for mass-production of solid state nanopores* is another challenge for the commercialization of instruments based on solid state nanopores. To ensure high throughput and accuracy, solid state nanopores with diameters small than 20 nm need to be produced in massively produced in massively parallel arrays. However, solid state pores are typically made by focused ion beam sculpting or TEM e-beam drilling, techniques that can achieve either the goal of massive production or small diameter easily, but not both.

2.3 Nanofluidic Devices

Nanofluidic devices are fluidic systems containing nano-sized features (e.g. nanochannels, nano-slits, nano-cavities, nano-posts and nanopores, by nanoscale is meant a dimension in the 1-100nm range). With at least one dimension in the range of nanometer scale (typically 1 to 100 nm). Compared with conventional less well-defined porous media (e.g. electrophoresis gels), nanofluidic devices with the size of biomolecules, such as DNA or proteins, enable the study of various properities (physical, chemical and biological) of biomolecules and also allow researchers to understand the fundamental transport phenomena at nanoscale. Nanofluidic devices have the advantages of ultra small sample volume requirement, CMOS compatibility and massive production potential, which will potentially enable various industrial applications.

2.3.1 Nanofluidic Device Fabrication

Top-down Fabrication Methods

The basic principle of top-down fabrication is similar to the idea of sculpting from a block of stone. Starting from a base material (silicon, glass or plastic), through different kinds of 'sculpting' techniques, we carve the stone until the desired shape is achieved. Four major top-down lithography methods for nanochannel device fabrication will be briefly discussed:

E-beam Lithography

In the e-beam lighography technique, a beam of electrons is scanned over a thin layer of e-beam resist, such as PMMA and ZEP520A, typically in the thickness of ~ 100 nm deposited via spin coating. Chemical bonds are broken after e-beam exposure, the exposed e-beam resist (positive resist) is dissolved and washed away in a 'developer' solvent leaving nanoscale features in the resist layer. In a typical EBL system, a resolution of 20 nm can be achieved routinely. While EBL can achieve 5nm resolution,

this requires a very careful state-of-the-art characterization process [44]. In order to transfer the nanochannel features from the resist layer into the substrate, a follow up reactive ion etching (RIE) process is needed. The resist coated substrate is placed into an RIE system and the exposed region is etched (typically fluorine-based plasma is used for removing silicon based material). After striping e-beam resist, the substrate is then cleaned with RCA2 (1:1:5 diH_2O:H_2O_2:HCl) and RCA1 (1:1:5 DI-H_2O:H_2O_2:NH_4OH) process for direct bonding.

FIB Technique

As already mentioned, FIB is a widely used technique for fabricating solid state nanopores on thin membranes; FIB can also be used for nanochannel device fabrication. In FIB systems, quite distinct from the EBL process, nano-features are directly formed in the substrate using a beam of Ga^+ ions (so no further etching step is required). This technology is very flexible. In a dual-beam FIB system, the FIB is coupled with an SEM, so that structures produced with FIB can be immediately imaged in an SEM and modified (if necessary) with a second FIB step. However, the FIB milling time is much longer than exposure of an equivalent pattern via EBL, drastically limiting throughput. In addition, limited by the minimum focus spot size of the ion beam, FIB is not optimized for creating sub 20 nm features routinely. While successful fabrication of channels with 5 nm dimensions has been demonstrated via FIB, in this case a specialized process was used, based on FIB drilling through a thick 300 nm Cr masking layer [45].

Nanoimprint Technique

The nanoimprint lithography technique was pioneered by the Chou group at Princeton [46]. In nanoimprinting, a thin layer of imprint resist (thermoplastic polymer)

is spin-coated on the substrate. Then a hard mold with raised predetermined nano-patterns (fabricated typically via EBL/RIE), is pressed into the resist under a set uniform pressure. The substrate is then heated, raising the resist temperature above its glass transition temperature, so that the resist softens and conforms to the mold. The mold is then released from the resist after being cooled down resulting in transfer of the nano-pattern from the mold into the resist. A further pattern transfer process (typically RIE) is required to transfer the nano-features into the substrate layer. This technique is also described as thermal nanoimprinting lithography (T-NIL).

In 1999, a variant of the NIL process was developed by Willson group at UT Austin. The Willson group used a UV sensitive polymer as the imprint resist [47]. The photocurable resist is applied on the substrate via spin coating and the mold is typically made of transparent material such as glass and PDMS. After the mold and the substrate are pressed together, the resist is cross-linked by UV exposure and hardens around the mold features, transferring nanopatterns from the mold into the resist. A further pattern transfer process is required to transfer the nanofeatures into the substrate layer. This NIL variant is named as photo nanoimprinting lithography (P-NIL).

Soft Lithography

Soft lithography, which has revolutionized microfluidics, has also been adapted as a powerful technique for nanoscale feature fabrication. The soft lithography technique is based principally on a polymer known as polydimethylsiloxane (PDMS). When mixed with a curing agent (Silane precursor) and heated at $\sim$ 70C for at least 1 hour, PDMS hardens to form a flexible silicon rubber. In soft lithography, first a hard mold is produced containing pre-made reversed nano/microscale features (the mold is usually etched in silicon or made using SU-8 photoresist). Then a layer of pre-mixed PDMS

is poured onto the mold and degassed for $\sim$ 20 minutes in order to remove trapped air bubbles. The PDMS is then heated up in an oven where it hardens into a rubber elastomer. The released PDMS contains the reversed nano-features from the mold. In order to seal the fluidic device, an oxygen plasma is used to activate the PDMS surface. The PDMS will then bond irreversibly to a glass surface (forming the device lid) after being brought into contact. [48]

Bottom-up Fabrication Methods

The basic principle of bottom-up fabrication is similar to the idea of building a brick house. Instead of building a 'house' from bricks, we are using atoms or molecules to build the final structure we desire. Structures such as carbon nanotubes (CNT) are readily usable nanochannels. Carbon nanotubes are rolled-up sheets of graphene held in shape via sp2 bonds, which are stonger than the sp3 bonds found in diamond, proving them unique mechanical strength and stability. In 2003, researchers reported the successful translocation of DNA molecules through a 77 nm diameter multi-wall CNT (MWNT) observed by fluorescent microscopy [49]. Follow up work demonstrated that 60-120 base pair dsDNA can successfully translocate through 1-2 nm diameter single wall carbon nanotubes (SWCNTs) [50]. The translocation process is detected electronically via monitoring the current after applying a voltage drop of around hundreds of millivolt across the tube [50]. Even though nanochannels created via bottom-up processes are often atomically smooth and uniform over the required length scales, the challenge lies in their interconnection and their integration into a fluidic device.

2.3.2 Transport in Nanofluidic Devices

The term 'nanofluidics' is defined as the study and application of fluid flow in and around nanometer-sized objects with at least one characteristic dimension below

100 nm. At the length scales of below 100 nm, which only contains hundreds of atoms at a certain dimension, new physical phenomena which have never been observed at marcro/microfluidic scale emerge [51, 52, 53].

Capillary Effects. Capillary action is caused by the combination of surface tension and adhesive forces between the liquid and container wall. Mathematically, the Laplace pressure P_L, arising at the interface of any two-phase system, can be expressed:

$$P_L = \gamma(1/R_1 + 1/R_2) \tag{2.1}$$

where γ is the surface tension of the interface and R_1 and R_2 are the principle radii of curvature. For a cylindrical nanochannel with a radius r, $P_L = 2\gamma cos\theta_c/r$, where θ_c is the contact angle. Given that water has a surface tension of 72.8 mN/m at room temperature, the channels have a diameter ranging from 10 - 100 nm and the channel surface is hydrophilic surface ($\theta_c = 50°$), the corresponding capillary pressure will be in the range of 10 - 100 bar. Capillary pressures up to -17 bars are reported by Tas *et al.* in 2003, thus allowing the spontaneous filling of nanochannels with liquid. However, in the case of a hydrophobic surface ($\theta_c = 105°$), the capillary pressure is in a range of 4 - 40 bar, indicating that a large pressure will be required to fill a hydrophobic nanochannel.

Electrokinetic Effects. Electrokinetics is defined as the study of the dynamics of fluids containing electrolyte species (e.g. contain dissolved ions). Electrokinetics encompasses a family of different phenomena including electrophoresis, electro-osmosis, diffusiophoresis, capillary osmosis, sedimentation potential, streaming potential/current, colloid vibration current, and electric sonic amplitude [54]. Essentially, these phenomena arise in systems containing electrolyte solution in contact with charged surfaces and involve coupling between electrical and hydrodynamic phenomena. Electrokinetic

effects are commonly used in microfluidic systems to create fluid flow and drive particle transport via applied electric fields.

The electric double layer (EDL) is the source of electrokinetic effects. Surfaces in contact with an aqueous solution typically gain a net surface charge density. This surface charge density may originate from chemical reactions, absorption, or defects in a crystalline structure [55]. In particular, the charge of glass originates from the disassociation of surface associated silanol groups (-SiOH to -SiO^-). In a liquid with free cations and anions, counterions (ions with opposite charges, together with an ionic species to maintain electric neutrality) will be absorbed to the surfaces due to chemical interactions forming an immobilized layer, the Stern layer. In addition, a second layer of charge, composed of mobile ions attracted to the charged surface by the electric field, extends into solution. This layer is called the diffuse layer and completely screens the surface charge. The diffuse layer and the surface charge (including the immobilized ions in the Stern layer) together form the electric double layer. We define the zeta potential ζ_0 as the electric potential at the surface of shear between the liquid and the surface (the surface of shear is located at the edge of the Stern layer). The equilibrium distribution of the electrostatic potential near the surface follows the Poisson-Boltzmann equation [51]:

$$\nabla^2\psi = \frac{d^2\psi}{dz^2} = -\frac{e}{\epsilon_0\epsilon_r}\sum_i n_i^\infty z_i \exp[-z_i e\psi(z)/k_B T] \tag{2.2}$$

For small surface potential, the exponential can be Taylor expanded and Poisson-Boltzmann equation can be expressed (Debye-Huckel approximation):

$$\nabla^2\psi = \frac{d^2\psi}{dz^2} = \kappa^2\psi(z) \tag{2.3}$$

Where ψ is the electric potential, k_B is the Boltzmann constant, z_i is the valance of the ith ionic species, ϵ_0 is the vacuum permittivity, ϵ_r is the relative permittivity, n_i^∞

is the bulk number density of the ith ionic species, T is the temperature and κ is the Debye-Huckel parameter. From equation 2.3, we have:

$$\kappa = \left(\frac{e^2 \sum_i n_i^\infty z_i^2}{\epsilon_0 \epsilon_r k_B T} \right)^{1/2} = \left(\frac{e^2 I}{2\epsilon_0 \epsilon_r k_B T} \right)^{1/2} \tag{2.4}$$

where $I = \frac{1}{2} \sum_i z_i^2 n_i^\infty$ is ionic strength of the solution (for a one-one electrolyte such as KCl, $I = n_i^\infty$). The Debye-Huckel parameter κ is mainly dependent on the bulk number density n_i^∞. In the diffuse layer the potential decays exponentially over a characteristic distance defined as the Debye length $\lambda_D = \kappa^{-1}$. The Debye length quantifies the thickness of the electric double layer. Due to the screening effects of free ions, the higher the ion concentration the smaller the Debye length. Table lists the EDL thinkness as a function of solution molarity for KCl at 25°C.

Solution	Debye length λ_D (nm)
pure water	1000
10^{-3} M KCl	9.6
10^{-2} M KCl	3.1
10^{-1} M KCl	1.0
10^{0} M KCl	0.3

Table 2–1: Electric double layer thickness λ_D as a function of solution molarity for KCl at 25°C

Electrophoresis and Electroosmosis Electrophoresis relates to the motion of charged particles in a stationary fluid induced by an electric field. Electrophoresis is widely used to move ions and molecules in micro- and nanofluidic systems. A typical application is DNA gel electrophoresis. Electroosmosis is the motion of liquid, with respect to a stationary charged surface, induced by an external electric field applied across the fluidic channel. If the surface is positively charged, the net excess of negative ions in the EDL will move towards anode, viscously entraining liquid and giving rise to net fluid flow in the channel [56]. For high ionic strength solution in a nanochannel, the

liquid velocity is zero close to the channel wall, and then increases to a maximum value over the Debye length, after which it remains constant. The electroosmotic velocity profile can be described via:

$$v_{eo} = -\frac{\epsilon_0 \epsilon_r \zeta_0 E_x}{\eta} \tag{2.5}$$

Where ζ_0 is the zeta potential, η is the dynamic viscosity of the fluid and E_x is the electric field in the x direction. Electro-osmosis is commonly used in micro/nanofluidic devices, typically involves fluidic systems with highly charged surfaces. In analytic seperation processes, the electroosmotic flow is reported to have an effect on the elution time of the analytes [57]. Researchers also demonstrated that coating the surface with polyelectrolytes can lead to suppression or the inversion of electro-osmotic flow [58].

2.4 DNA as A Polymer

DNA molecules, constructed by repeating nucleotides, can be considered as a polymer chain. There are four key parameters to characterize a polymer chain: contour length (L), radius of gyration (R_g), persistence length (P), and effective width (w). The contour length describes the total length of a polymer when fully extended. A λ-DNA molecule (48.5 kbp) has a contour length of around 16 um [48]. The radius of gyration is defined as the average squared distance of any point in the chain from the chain center of mass and quantifies the spatial extent of the polymer coil. The gyration radius of λ-DNA molecule at 10 mM ionic strength is around 0.7 μm [48]. The persistence length represents a length scale below which the chain behaves as a rigid rod, it quantifies the bending rigidity of the chain. DNA has a persistence length of around 50 nm [48] in high salt conditions. The effective width, arising from a combination of steric and electrostatic repulsion, describes the closest distance of approach of two back-folding polymer segments before their interaction energy exceeds thermal energy ($k_B T$). The effective width of DNA molecule at 10 mM ionic strength is around 10 nm [59].

Flory theory in bulk. The simplest model to describe a polymer is the ideal chain. The ideal chain is modeled as a random walk neglecting the interactions between chain monomers. However, a "real" polymer chain, such as single DNA molecule, cannot pass trough itself. This effect is known as "self-avoidance". The self-avoiding effect also depends on the effective width and contour length of the DNA molecule. If the molecule is sufficiently "thin" (w is small) or the contour length is sufficiently short (L is small), the probability of the DNA molecule overlapping with itself is negligible. Under these circumstances, a single DNA molecule can still be considered as an ideal chain. A single DNA molecule short than around 10 kbp can be considered as an ideal chain. Accordingly, the scaling between radius of gyration (R_g) and the contour length (L) in three dimesions, can be written as [48]

$$R_g \sim L^{\frac{1}{2}}. \tag{2.6}$$

A single DNA molecule greater than around 10 kbp will be considered as a self-avoiding chain. A self-avoiding chain is a chain occupies a finite volume and the segments can not overlap with each other.

When considering the effect of self-exclusion, the scaling between radius of gyration (R_g) and the contour length (L) can be written [48]

$$R_g \sim L^{\upsilon} \tag{2.7}$$

where υ is the scaling exponent (also called Flory exponent). The scaling exponent is strongly depend on the dimensionality (d) of the space. Previous analytical calculations and simulations show that [60]

$$\upsilon = \frac{3}{2+d} \tag{2.8}$$

For d=1, $R_g \sim L$. Obviously, the chain can only extend linearly due to self-avoidance. For d=3 (a bulk environment), $R_g \sim L^{0.6}$. A more detailed theoretical estimation gives 0.588 [61].

Flory theory provides a simple way to understand the effect of excluded-volume interactions on chain conformation. The total free energy of the polymer chain can be written as the sum of entropic (F_{En}) and excluded volume (F_{Ex}) free energy terms. Considering the simpler case of an ideal chain (no self-avoidance), the entropic energy of the chain can be written [62]

$$F_{En} \cong \frac{3}{2lL}R^2 \tag{2.9}$$

where l is the length of each chain segment. R is the end to end length of the chain.

The excluded volume free energy arises from the segment-segment interactions (neglecting higher order terms that arise from interactions of more than two-segments) [48]

$$F_{Ex} \cong \frac{1}{2}k_B T\chi\frac{N^2}{R^3} \tag{2.10}$$

where $\chi = wl^2$ is the excluded volume of each segment. Adding the two energy terms together gives us the total free energy:

$$F = \frac{3}{2lL}R^2 + \frac{1}{2}k_B T\chi\frac{N^2}{R^3} \tag{2.11}$$

The equilibirum extension (R_F) can be obtained by minimizing the free energy (Eq. 2.11):

$$\frac{dF}{dR} = 0 \Longrightarrow R_F \sim (wP)^{1/5}L^{3/5} \tag{2.12}$$

which is consistent with the expected value $\nu = 0.6$ for a self-avoiding polymer in 3D.

2.4.1 DNA under Confinement

The effect of confinement on single molecule DNA conformation has implications for two fields: polymer physics, where DNA molecules is a model for developing polymer theory under confinement and nanofluidics, where confinement is applied as an approach for single-molecule manipulation [63]. Chapter 3 of this dissertation presents a novel nanofluidic device design based on confining DNA molecule in a pore embedded nanochannel. In this design, DNA molecule is pre-stretched in a quasi-1D confinement (nanochannel width=100-220 nm, depth=120 nm). The total extension of the DNA molecule inside nanochannel can be predicted by polymer theories [48]. Depending on the relative size of nanochannel width (d) compared to the key molecule polymer parameters (e.g. radius of gyration R_g, persistence length P), the effect of confinement can be divided into different physical regimes shown in figure 2–4.

For a channel width greater than R_g, the DNA molecule cannot feel the effect of confinement, so the molecule behaves the same as in bulk. For channel width $D_{\star\star} < D < R_g$, DNA molecule is confined in the classic de Gennes regime, where the molecule can be treated as a string of isometric Flory blobs. Inside each blob (diameter D), the molecule can be considered as an unconfined self-avoiding polymer. For channel width $2P < D < D_{\star\star}$, DNA molecule is confined in the extended de Gennes regime, where the molecular conformation is characterized by a string of elongated blobs. $D_{\star\star}$ is the critical channel width, below which DNA molecule can be considered as an **ideal chain** instead of a self-avoiding chain inside each blob. For channel width $D < P$, DNA molecule is confined in the Odijk regime. In the Odijk regime, the DNA molecule can no longer coil due to the bending energy cost of forming a hairpin turn in the nanochannel. In the Odijk regime the DNA molecule can be characterized by a series of deflections (deflection length λ) with the wall (figure 2–4).

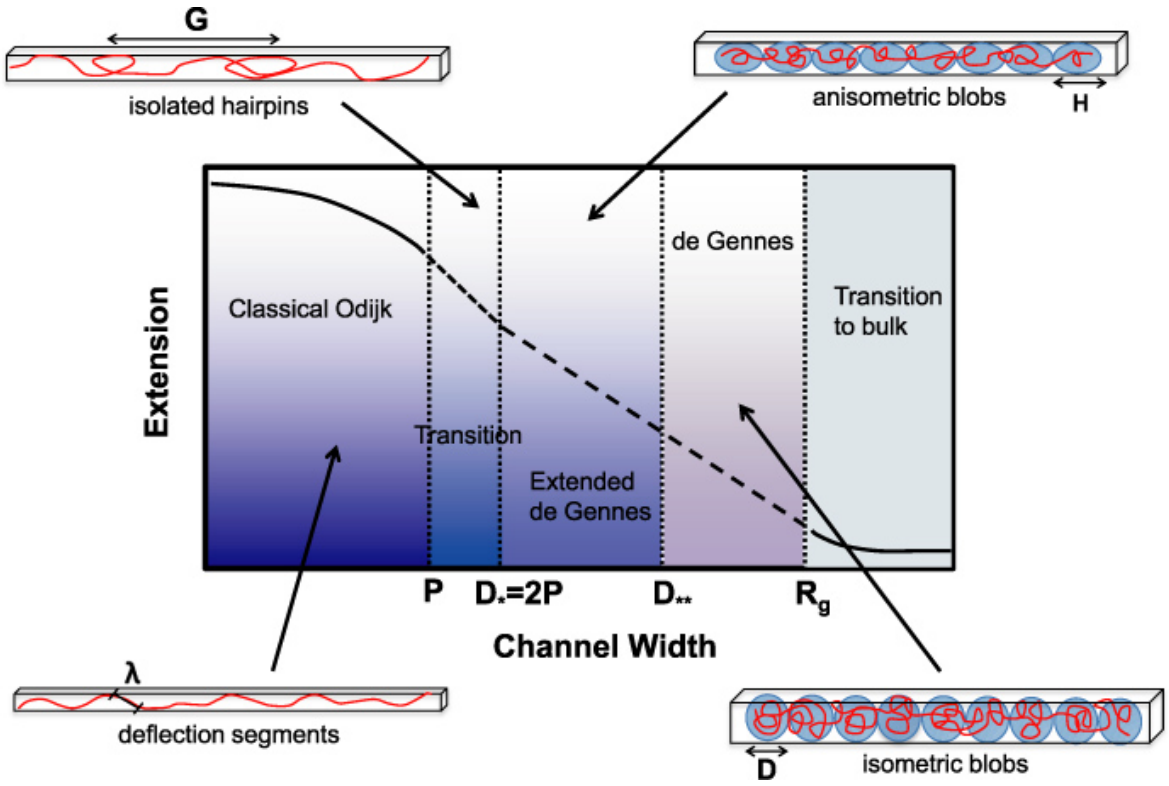

Figure 2–4: Physical regimes of a polymer in nanochannel confinement in relation of nanochannel width. Channel width $D \geq R_g$, polymer behaves the same as in bulk. Channel width $D_{\star\star} < D < R_g$, polymer is in the classic de Gennes regime. Channel width $2P < D < D_{\star\star}$, polymer is in the extended de Gennes regime. Channel width $P < D < 2P$, polymer is in the transition regime. Channel width $D < P$, polymer is in the classical Odijk regime. Figure adapted from [48].

2.4.2 Experimental Studies and Applications

As the fluidic device dimensions are scaled down, fewer molecules present inside the volume defined by the nanochannel. In the limit where the nanochannel dimensions approach that of a single molecule (e.g. polymer gyration radius, particle diameter) trapping, isolating and sensing single molecules became feasible with nanochannel devices. Consequently, the physical and chemical behavior of individual molecules can be accessed instead of obtaining values averaged over large populations of molecules (ensemble average).

Over the past decade, biophysicists have used nanofluidic devices as platforms to study and test the models of motion of individual DNA molecules. In 2002, Craighead group at Cornell directly counted and measured the length of DNA fragments via fluorescence correlation spectroscopy in submicrometer-sized (10 μm width, 270 nm height) closed fluidic channels [64]. In 2005, Riehn from Austin group at Princeton reported the successful restriction mapping of DNA molecules using restriction endonucleases in nanochannels with diameters of 100-200 nm [65]. In the same year, Wang from yje Austin group performed single-molecule studies of repressor proteins binding to λ-DNA confined in nanochannels via using high-resolution fluorescene microscopy techniques[66]. This study marks the start of a new era of nanofluidic platform based DNA-protein interaction study, which is of great interest to biologist and opens a door for them to direct visualize the inter-molecular reactions through fluorescence microscopy technique. Nanochannels can also be used as quasi-1D confinement to study DNA molecules. In 2005, Reisner from Austin group reported the successful fabrication of silica based nanochannel devices and the study of statics and dynamics of single DNA molecules stretched in nanochannels [67]. Later in 2007, Reisner *et al.* studied the response of confined single DNA molecules to the changes in ionic environment, and they also reported longer extension of DNA than expected in a nanochannel, due to the interactions between DNA molecules and the walls [17]. The reducing of ionic strength of the buffer will increase the persistence length of DNA molecules, thus allowing scientists to stretch DNA molecules at similar extension in larger PDMS channels [68].

2.5 Electron Microscopy

2.5.1 Resolution

An electron microscope, using accelerated electrons as the illumination source, can reach atomic level resolution due to the ultra small electronic wavelength. The resolution of an imaging system is given by the Abbe diffraction limit:

$$d = \frac{\lambda}{2n \sin \theta} \tag{2.13}$$

Here d is the smallest distance between two distinguishable dots (also referred as resolution), λ is the incident wavelength, n is the index of refraction of the medium, θ is the half-angle subtended by the optical objective lens. According to the de Broglie relationship, the wavelength of electrons being accelerated through a voltage drop V is determined by:

$$\lambda = \frac{h}{\sqrt{2meV}} \tag{2.14}$$

Where h is the Planck constant, e is the net charge of an electron and m is the electron mass. If the acceleration voltage is sufficiently high, relativistic effects have to be taken into account. For example, for a typical V $\sim 200\,\text{keV}$, electrons are accelerated to $\sim 70\%$ of the speed of light. The relativistically corrected wavelength is:

$$\lambda = \frac{h}{\sqrt{2meV}} \cdot \frac{1}{\sqrt{1 + \frac{eV}{2mc^2}}} \tag{2.15}$$

For V $= 200\,\text{keV}$, Eq. 1.8 gives $\lambda = 2.5{\times}10^{-3}\,\text{nm}$ (compare to 400-700 nm range for visible light). Thus theoretically, an electron microscope has sub-atomic resolution. Practically, the resolution of TEM is $\sim 0.1\,\text{nm}$ limited by the objective lens system (due to the spherical aberration of the magnetic lenses) [69].

An electron microscope can operate in two fundamentally different modes: scanning and transmission. In a transmission electron microscope (TEM), the direct electronic analogue to an inverted light microscope, the electron beam is passed through a thin sample and imaged on a detector. In a scanning electron microscope (SEM), the electron beam is raster scanned and the image formed by measuring the collected electrons as a function of beam position. SEM's have detectors for collecting electrons back-scattered from the sample (back-scattered electrons) and electrons generated via interactions with the sample (secondary electrons). An SEM image contains information related to surface topography and surface chemical composition. The resolution of an SEM is not limited by the diffraction limit or spherical aberration of lenses. Instead, the spatial resolution of the SEM depends on two major factors: the size of the electron spot and the size of the electron-specimen interaction volume. The resolution of SEM, is typically between 1 nm and 20 nm depending on the instrument. In 2009, Hitachi launched the SU9000 SEM demonstrating the successful imaging of the lattice structure of graphite at 30 kV, which is by far the highest resolution ever achieved ($\sim$ 0.4 nm) [70].

2.5.2 Operating Conditions

Scanning Electron Microscope. SEM typically operates at a vacuum level of better than 10^{-4} torr. A dry specimen is usually required for conventional SEM to prevent liquid evaporation and outgassing. The specimen surface also needs to be electrically conductive and grounded to prevent the accumulation of electrostatic charge that can bend the electron beam and distort the image. Non-conductive specimens are typically coated with a thin layer of electrically conducting material, such as amorphous carbon, Au and Ti, by either low-vacuum sputtering coating or high-vacuum evaporation. Biological samples, such as living cells, tissues and soft-bodied organisms can also be

imaged after chemical fixation and dehydration [71]. Recent development of the environmental SEM (E-SEM) allows specimens to be imaged without conductive coating under native "wet" conditions. The E-SEM is equipped with specialized electron detectors with differential pumping systems allowing the electron beam to be generated from high vacuum in the gun area and be transfered to low vacuum in the specimen chamber. The specimen chamber is usually purged and filled with water or atmospheric gas. Gas molecules will be ionized during exposure to the high energy electron beam. The ionization leads to an increased conductivity that prevents electrostatic charging on the specimen surfaces, enabling the direct imaging of non-conductive material. As a result of introducing extra gas molecules into the chamber, the contrast and resolution of E-SEM is slightly decreased compared to a conventional SEM: the higher the chamber pressure, the lower the system contrast and resolution.

Transmission Electron Microscope. Similar to SEM, dry specimens are typically required for TEM due to the restriction of operating at ultra high vacuum condition (typically on the order of 10^{-7} torr). Biological specimens, which often contain a high percentage of water and have soft and undefined dimensions, are typically dehydrated or frozen (e.g. cryo-TEM) and fixated onto TEM grids before being imaged. High voltage, typically in the 80-200 keV range, is required to achieve beam transmission through the sample. The specimen will also need to be sufficiently thin ($\sim$ 100 nm, several hundreds of atoms thick) to enable electron transparency. Sample preparation for TEM is very demanding. Critically, the sample must be very thin (¡100nm thick) to ensure electronic transparency. Nanomaterials in solution (e.g. nanotubes, nanowires) can be prepared rather conveniently for TEM imaging by distributing the diluted sample containing solution onto special supporting film grids. The support film grid contains a copper grid and a thin amorphous membrane, usually carbon with a

thickness ranging from 2 – 100 nm, which is mechanically stable and electron transparent. However biological samples, often soft and with undefined shapes, needs to be dehydrated or frozen under low temperature before imaging with TEM. On the other hand, for a standard TEM, the interaction between electron beam and specimen increases roughly with atomic number squared (z^2) [72]. Biological samples principally contain of light low z atoms such as H, C, O, P and S, limiting contrast and making the direct imaging of biological structure with TEM very challenging. In order to overcome this problem, biological specimens are typically stained with heavy metals, such as uranyl acetate and lead citrate, which can produce high electron density contrast for TEM imaging.

2.5.3 Liquid Cell Electron Microscope

Liquid cell electron microscopy is an electron microscopy technique allowing the direct imaging of liquid samples in a microscopic vacuum system. It is becoming an increasingly attractive option. Liquid cell electron microscopy enables the dynamical imaging of specimens with subnanometer resolution while keeping biological samples in their native condition from dehydration. Over the past several decades, liquid cell electron microscopy has been applied in diverse fields such as materials science, physics, chemistry and biology [73, 74], including the growth mechanism and assembly dynamics of nanocrystals [75], tracking and manipulation of nanoparticles [76], and imaging of biological materials [77].

The first generation of liquid cell electron microscopy can be traced back to 1934 right after the invention of TEM. Biological samples sandwiched between two thin aluminum foils were imaged with the first TEM [78]. Over the following several decades, liquid cell electron microscopy developed relatively slowly due to technical challenges of keeping liquid samples intact in the high vacuum of an electron microscope. In recent

years, due to the rapid development of semiconductor industry and the development of nanofabrication technology, researchers were able to sandwich samples between two ultra thin silicon nitride membranes and image them via a TEM. These nitride films are sufficiently thin to enable transmission of electron beam. The advantages of the nitride liquid cell also include excellent mechanically stability, homogeneity in thickness and biocompatibility, allowing for the direct culture of cells. In 2003, Williamson *et al.* observed the nucleation and growth of nanoscale copper clusters during electrodeposition at the solid-liquid interface using a double layer 80 nm thick silicon nitride liquid cell [79]. This research marked the beginning of a new era of the modern liquid cell electron microscopy. Various designs of liquid cells have been reported, by using these customer liquid cells, researches were able to study nanoparticle motion in solution[75, 80, 76, 81]; liquid nanodroplets and bubble formation [82, 83]; biomineralization [84]; biological materials, such as DNA molecules and the whole COS7 fibroblast cell in liquid environment [77]. Liquid cell electron microscopy has key advantages compared with conventional approaches that use dried or frozen samples. Liquid cell approaches allow for direct observation of dynamic behavior in materials at high spatial and temporal resolution and the imaging of biological materials (such as DNA, proteins, cells) in their native aqueous environment.

CHAPTER 3
Nanopore Embedded Nanofluidic Devices for Single-molecule DNA Analysis and Manipulation

Chapter 3 presents the fabrication and characterization of an integrated nanopore nanochannel structure on thin silicon nitride membrane devices for the manipulation and analysis (fluorescent imaging) of single DNA molecule.

This chapter is the integral text from:

Nanopore Embedded Nanofluidic Devices for Single-molecule DNA Analysis and Manipulation

Yuning Zhang and Walter Reisner, Nanotechnology 26, no. 45 (2015): 455301. [85]

3.1 Introduction

Nanopore and nanochannel based devices are robust methods for bimolecular sensing and single DNA manipulation. Nanopore-based DNA sensing is a leading candidate as a single-molecule DNA sequencing technology [86]; nanochannel based extension of DNA, combined with enzymatic or denaturation-based barcoding schemes [87, 88], is a powerful approach for high-throughout genomic mapping. Devices combining nanochannels with pores may lead to a range of new applications based on the ability to combine optical and blockade-based electrical detection methodologies. Yet, combining nanochannel and nanopore based fluidics presents serious challenges due to the very different fabrication approaches used. Nanochannel devices are made via direct

electron beam or nanoimprint based lithographic technologies on silicon or glass wafers (typically ∼0.5 mm) [88]. These devices are then bonded to coverslip thin glass via either thermal or anodic bonding. Solid-state nanopore based devices are fabricated via electron beam milling [29], or recently via dielectric breakdown [89], through thin silicon nitride or oxide membranes (20-50 nm thickness). The devices are typically inserted into cells that contain macroscopic or micro size buffer reservoirs located on either side of the membrane.

In this chapter, we demonstrate the fabrication and operation of a combined nanochannel-nanopore device (figure 3–1 a). In particular, we show that in equilibrium a nanochannel extended DNA molecule will not escape through an embedded sub-persistence length pore in a nanochannel. Moreover, upon application of a pneumatic pressure drop across the nanochannel, the DNA will slide transversely across the pore without undergoing translocation. If a trans-pore voltage drop is applied, we find we can perform cross-pore translocation of the molecule out of the nanochannel and into the adjoining microchannel reservoir. Upon reversal of the bias, the molecule will be sucked back into the nanochannel. Finally, we show that we can precisely position nanopores in a variety of lithographic features, including channels and rectangular nanocavities with dimensions in the range of ∼100 nm. Such cavity geometries are suitable for localizing single-molecules at a precise position on the chip [90]. While a number of groups have demonstrated that nanopores can be incorporated into microfluidic devices, these approaches are typically based upon PDMS fabrication [91, 92], restricting the dimensions of transverse channel features to greater than 10 μm, too large to alter the molecule equilibrium conformation [87] and permit the stretching demonstrated here. In addition, our approach is distinct from that of Pedone *et al* [93] and Liu *et al* [94]. These authors create a micro scale vestibule interfaced to a pore at one

end with an opening $\sim 100\,\text{nm}$ at the other end. These vestibule structures function as entropic cages [94], keeping the molecule in the vicinity of the pore prior to translocation. This approaches differ from our current device in that the vestibule structures are still micro scale (with dimensions 1-10 μm) and that the vestibule opening itself is interfaced to a bulk reservoir, not a nanochannel structure.

3.2 Device Concept

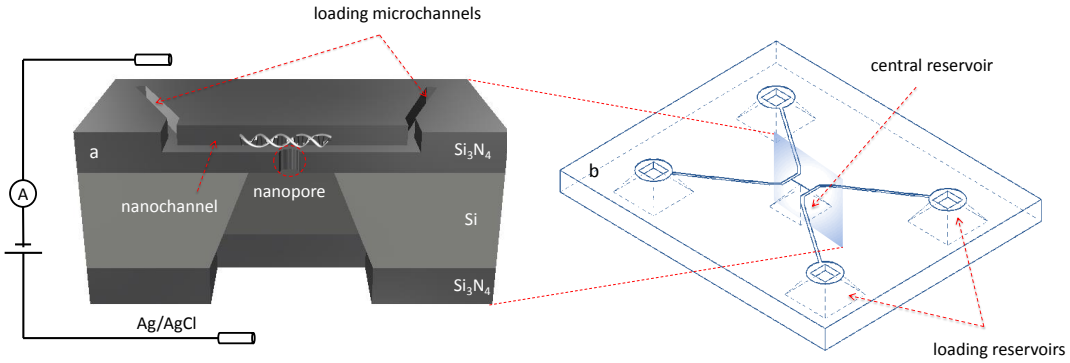

Figure 3–1: (a) Concept figure showing cross-section of nanopore/nanochannel device. A cartoon DNA molecule is shown inside the nanochannel in the nanopore region. (b) Schematic showing the chip layout including location of loading microchannels, nanochannel and the KOH-etched central and loading reservoirs.

A schematic of the nanopore/nanochannel device is shown in Figure 3–1. The mainbody of the nanofluidic device is a 500 μm thick $5 \times 6\,\text{mm}$ silicon chip. Both sides of the silicon chip are coated with 180 nm thick silicon nitride deposited via low pressure chemical vapour deposition (LPCVD). The device contains a single KOH-etched central reservoir spanned by a 180 nm thick free-standing nitride membrane. In addition there are four KOH-etched loading reservoirs, punched completely through the nitride membrane to enable introduction of fluid. Microchannel and nanochannel features are

created in the nitride layer in order to minimize electroactive area and reduce membrane capacitance [95]. In particular, we employ a classic design whereby two U-shaped micro loading channels (width=50 μm, depth=120 nm), connected to two loading reservoirs, are bridged by the nanofluidic channels (Fig. 1b, width=220 nm, depth=140 nm and total length=250 μm). The central KOH-reservoir is located between the two micro-loading channels so that the nanochannel, bridging the gap between the two microchannels, is etched across the free standing membrane. Our fabrication approach employs electron beam lithography to produce the nanofeatures giving considerable flexibility in terms of what nanofluidic patterns can be created. We have produced devices containing single nanochannels (figure 3–2 a-b) and nanoslits containing arrays of embedded nanocavities (figure 3–2 b-f) . A nanopore is fabricated in the middle of the nanochannel through the nitride membrane via a transmission electron microscope (TEM) (figure 3–2 c-d). Pore-nanochannel alignment is facilitated by the ability to see the nanofeatures on the membrane directly via TEM (figure 3–2 c). Finally, the device is bonded to a standard microscope coverslip (figure 3–5 c shows bonded chip) via a custom low-temperature bonding protocol which will also be introduced in details in the fabrication section.

3.3 Device Fabrication

The details of our fabrication approaches are as follows (figure 3–4). The devices are fabricated wafer-scale on 4 inch silicon wafers with a trilayer sandwich structure: 180 nm of silicon nitride, 500 μm silicon and 180 nm Silicon nitride. Photolithography is used to define the positions of the fluidic reservoirs and central reservoir. A RIE process consisting of a mixture of CHF_3, Ar and CHF_4, optimized for nitride, is then used to remove the exposed nitride. The native oxide is removed by a one minute dip in diluted hydrofluoric acid solution (DI-water to acid 10:1). The wafer is then immersed

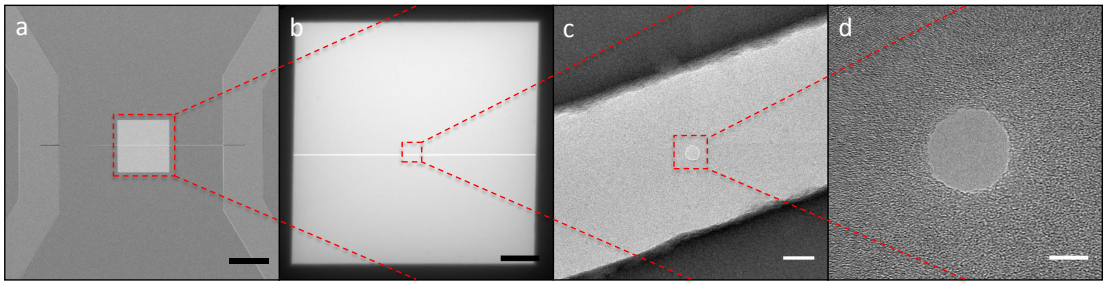

Figure 3–2: Fabrication results for nanochannel-nanopore device. (a) SEM image of the loading microchannels, central nanochannel and free standing silicon nitride membrane (scale bar is 50 μm). (b) TEM image of the central nanochannel and silicon nitride membrane (scale bar is 10 μm). (c) TEM image of a nanopore embedded inside the nanochannel (scale bar is 50 nm). (d) TEM image of a 21 nm pore (scale bar is 10 nm).

in a KOH laminar flow (the KOH buffer concentration is 45% w/w, normality is 11.67 N) bath and heated it to 65°C until the bulk silicon is etched through, resulting in a 70 μm$\times$70 μm 180 nm thick free-standing nitride membrane in the device center and at the reservoir positions.

Iterations of lithographic and etch steps are used to form the transverse nanofluidic and microfluidic features on the membrane-containing wafer. The nanofluidic features, either nanochannels(with a width of 220 nm, figure 3–2 c) or nanocavities(with width ranging from 100 to 1000 nm, figure 3–3 b), are defined via electron beam lithography in zep520A resist on top of the free-standing membrane and then etched via the nitride RIE process. The etch-process is carefully timed so that the nitride is not completely etched through, leaving a residual 40 nm of nitride in which the pore will be formed. Loading microchannels with a width of 50 μm are subsequently formed via another photolithography and RIE process. Nanopores are created using a standard fabrication process developed by the Dekker group [29] that utilizes a focused electron beam in a transmission electron microscope (TEM). Using a JEOL JEM-2100F TEM we can readily make nanoscale pores with diameter ranging from sub nanometre to 50 nm by

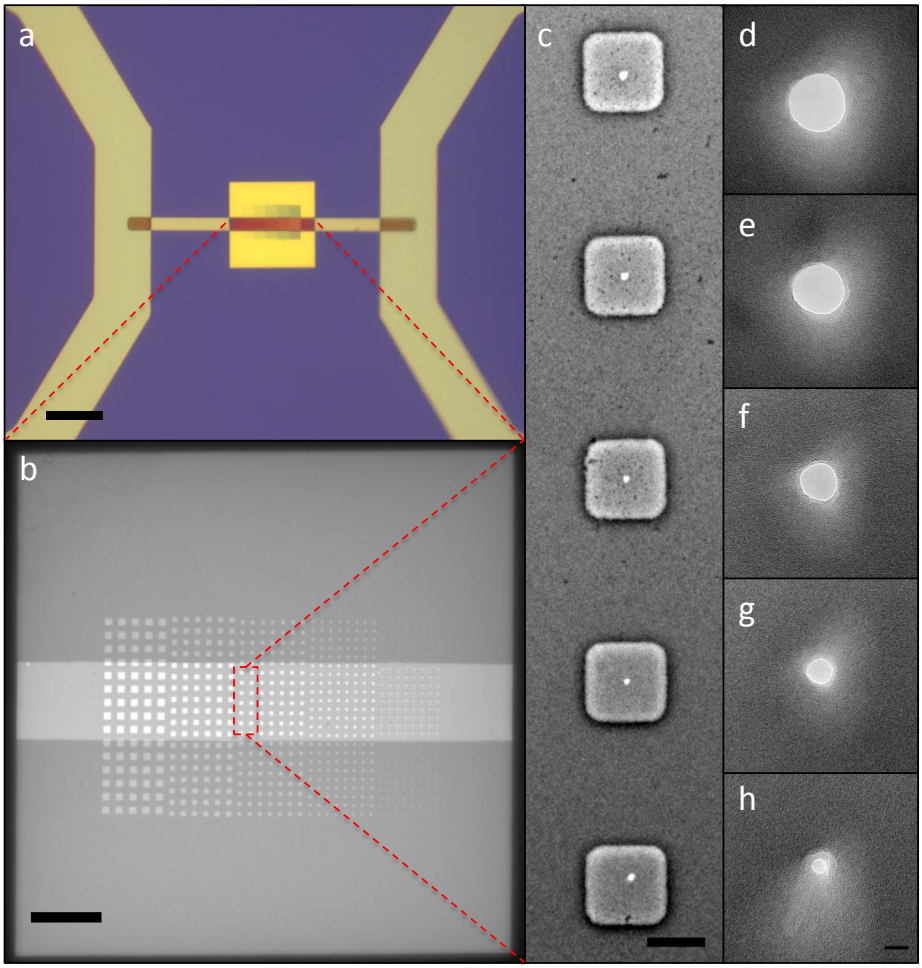

Figure 3–3: Fabrication results for nanocavity-nanopore device. (a) Optical image of the nanopore/nanocavity device: 50 μm wide loading channels are connected via a central 10 μm wide, 100 nm deep slit-channel across the silicon nitride membrane (the scale bar is 50 μm). (b) TEM image of the nanocavity array in the nanochannel and silicon nitride window (scale bar is 10 μm). (c) TEM image of nanocavity array containing various sized pores (scale bar is 400 nm). (d)-(h) TEM images of five individual nanopores fabricated inside 567×567×40 nm nanocavity array. From bottom to top the pore size is 5.8 nm, 10.6 nm, 15.6 nm, 21.3 nm and 24.6 nm (scale bar is 10 nm).

focusing the electron beam to a 2-4 nm spot on the membrane for 3-5 minutes and then adjusting beam position to control the pore size and shape.

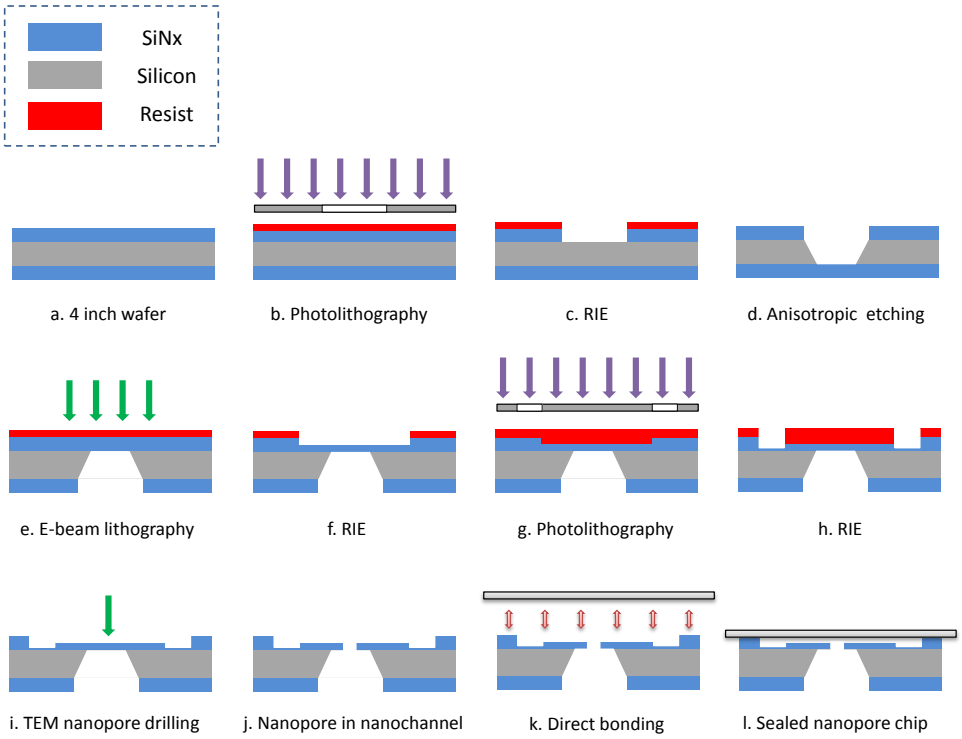

Figure 3–4: Nanochannel-nanopore device fabrication diagram. (a) Both sides of a 4 inch silicon wafer are coated with 180 nm of silicon nitride. (b)-(d) A photolithography step followed by reactive ion etching (RIE) and silicon anisotropic etching then forms the backside reservoirs. (e)-(f) A electron beam lithography step followed by RIE is used to create nanochannels. (g)-(h) A photolithography step followed by RIE is used to create loading microchannels. (i)-(j) The nanopore is formed via electron beam milling inside a TEM. (k)-(i) Our custom low temperature bonding step is then used to add the coverslip lid.

Developing a robust device bonding protocol was the most challenging aspect of our process. Due to the fragility of the free standing nitride membranes, a high temperature bonding protocol such as fusion bonding was not feasible. Moreover, we found that approaches based on sodium-silicate adhesive created too many defects in the nanofeatures. Consequently, we developed a low-temperature direct bonding protocol for silicon nitride to glass, following Wang *et al* [96] but omitting the high-temperature step. The protocol is as follows: a 20 minute piranha clean is followed by a RCA2 (HCl:H_2O_2:H_2O (1:1:5)) at 75∼80°C for 20 minutes and an RCA1 (NH_4OH:H_2O_2:H_2O (1:1:5)) at 77∼80°C for another 20 minutes. A standard borosillicate glass coverslip is then gently pressed against the chip, removing visible air bubbles. The edge of the coverslip is sealed with PDMS and cured at 80°C for 1 hour. The fabrication process of the nanopore/nanocavity device is almost identical to the nanopore/nanochannel device except a nanoslit, spanning the central membrane and connecting the loading microchannels, is added to introduce DNA into the cavities.

3.4 Device Operation

DNA molecules are driven inside the nanochannel via pneumatic pressure through a mechanic pump. Double straned DNA molecules will be stretched along the nanoscale channel, laying across the nanopore, due to the one dimensional confinement induced by the nanochannel. When a voltage is applied across the pore region, negatively charged DNA molecule will be locally captured to the pore region by electric field (figure 2-2). Given that DNA molecular width is around 2.5 nm, and DNA persistence length P is around 50 nm in the salt concentration (2 × TBE) we used, theoretically, we can fabricate a pore around or below the molecular width, and apply a voltage that is small enough will only attract the DNA to pore region instead of pushing it through. Ionic flow (K^+, Cl^-) across the pore region will be blocked by the DNA molecule that

lies across it, thus produces a blockade containing DNA structural information in the current trace. Importantly, this device is designed to have independent control over translocation speed and sensing signal. We can independently control the tanslocation speed by finely tuning pressure difference(ΔP), therefore we can scan any target region on a DNA chain as long as we need. Subsequently, a stable blockade signal could sustain longer enough for the nanopore detector to sense the structural information of any target region.

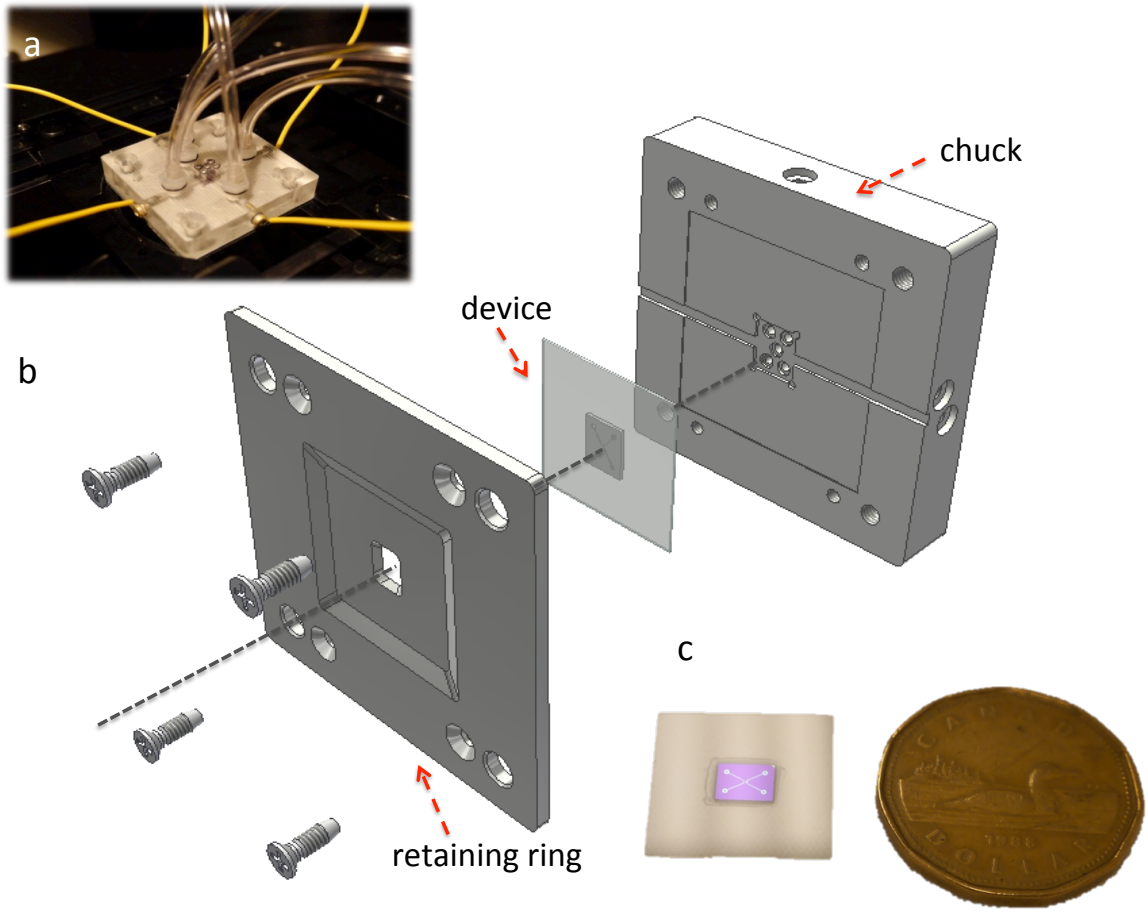

Figure 3–5: Fluidic cell and chip. (a) Schematic of the chuck, chip and retaining ring assembly. (b) Fluidic cell with luer connectors for applying positive air pressure (transparent tubes) and electric interconnects (yellow wires). (c) A nanofluidic chip next to a one Canadian dollar coin.

Stained T4 phage DNA is pipetted into the four loading reservoirs of our device and the solution is sucked by capillary action into the channels. The loaded device is then mounted on a custom-made chuck via oring seals to enable simultaneous electrophoretic and hydrodynamic actuation. In particular, hydrodynamic actuation is affected via pneumatic pressure applied at the reservoirs. DNA is transported across the microchannels using a pressure drop of 300-500 mbar. However due to the entropic barrier at the junction between the loading microchannels and nanochannel, higher pressure is required to drive DNA molecules into the nanochannel (1000-1500 mbar). Once the DNA molecules have been successfully introduced into the nanochannel the pneumatic pressure will be cut off; the DNA molecules will stop translating and remain inside the nanochannel where their dynamics will be observed and recorded via an EMCCD camera.

Figure 3–6 shows the dynamics of a T4 phage DNA located inside a pore-interfaced nanochannel (see also supplementary video 1). Figure 3–6 a shows a mosaic time-series of a DNA molecule inside the nanochannel; an embedded nanopore is located in the middle of the channel (figure 3–6 b-d). The DNA molecule is initially driven inside the nanochannel via a trans-channel pressure drop. The pressure is then cut off and the molecule halts (figure 3–6 a). A smaller pressure burst ($\sim$200 mbar) is then applied across the nanochannel. The DNA molecule slides across the 20 nm nanopore (figure 3–6 a-b). Note that the molecule stretches out as it crosses the pore: this effect arises as there is a small amount of flow through the pore created by the pressure drop, tending to the pin the molecule at the pore, but the flow is insufficient to force translocation. The pressure is then turned off and the DNA molecule relaxes to its equilibrium extension and stays at the right side of the pore. Next, a 1.5 V voltage drop is applied between the central reservoir and the right end of the nanochannel. The DNA

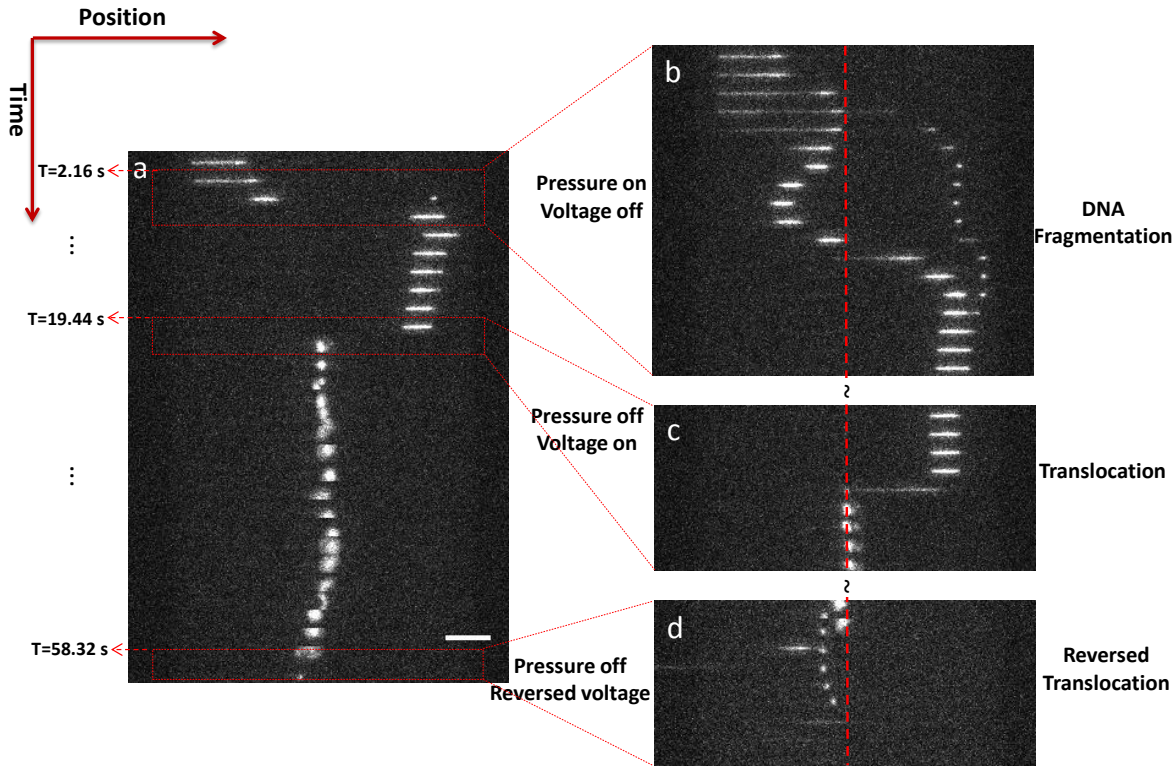

Figure 3–6: (a) Mosaic time series showing location of a T4 phage DNA molecule inside a pore-interfaced nanochannel (see also supplementary video 1); the time interval between each image is 2160 ms. (b) Zoom-in of time trace corresponding to upper box on (a): DNA molecule crosses the nanopore without translocation and the molecule fragments. (c) Zoom-in of time trace corresponding to middle box on (a): DNA molecule translocates through the nanopore crossing to the backside reservoir. (d) Zoom-in of time trace corresponding to lower box on (a): DNA crosses the pore in the backwards direction from the backside reservoir into the nanochannel. The dashed line shows the location of the nanopore. The time interval between each image in the magnified mosaics (b-d) is 240 ms.

molecule moves quickly towards the pore and then translocates through it (figure 3–6 a,c, see second box). The translocated molecule, now located in the central reservoir on the device backside, exhibits three-dimensional Brownian motion. Finally, we reverse the voltage: the DNA molecule is captured by the electric field and driven into the left

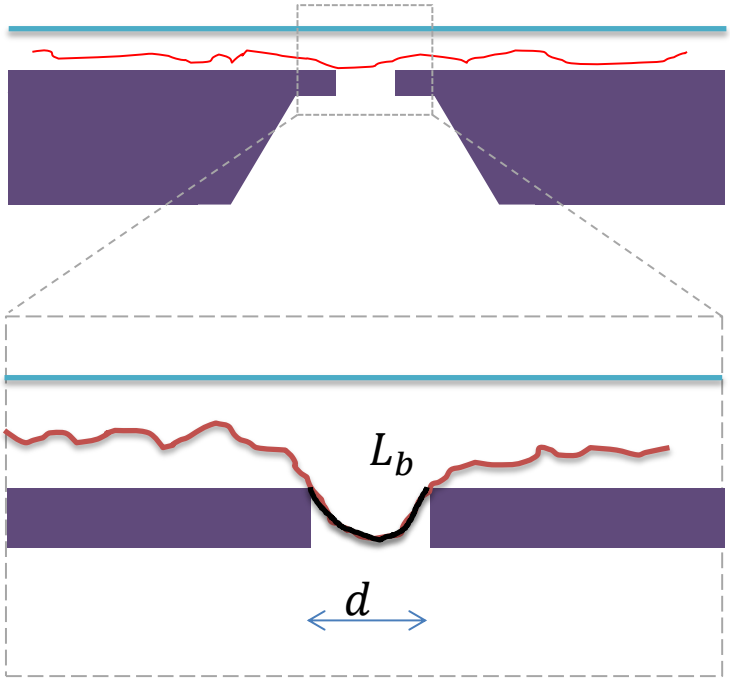

Figure 3–7: Concept figure showing a cartoon DNA molecule inside a nanochannel being driven towards the pore. If the molecule is initially straddling the pore, it must form a loop (herniation) in order to enter the pore with a diameter equal to the pore width d . The quantity L_b denotes the length of contour forming the loop.

side of the nanochannel through the nanopore (figure 3–6 a,d, see third box). We have also observed DNA fragmentation (figure 3–6 b) during the translocation. However, DNA fragmentation shown in figure 3–6 b is most likely due to DNA photonicking (e.g. due to fluorescent imaging) instead of arising from motion across the nanopore. Supplementary video 3 shows a DNA molecule repeatedly crossing a 20 nanometre sized pore without fragmentation and eventually translocating through the nanopore.

From a physical point-of-view, the barrier for cross-pore translocation arises from the requirement that the nanochannel-confined molecule form a U-shaped bend to enter the pore. In particular, the bending energy $E_{\text{bend}} = \frac{1}{2}k_BTPL_b/R^2$ where P is the DNA persistence length, L_b is the contour involved in bending and R is the

radius of curvature (figure 3–7). We estimate that the polymer will form a circular bend of diameter equal to the pore size d in order to enter the pore. The contour stored in the circular bend $L_b = \pi d/2$ and $R = d/2$ so that $E_{\text{bend}} = k_B T P/d$. We thus expect that sub-persistence pores will have an energy barrier in excess of $k_B T$ preventing translocation (as is observed here). In particular, the trapping time-scale can be estimated via $\tau \sim \tau_o \exp(P/d)$ where τ_o is the equilibrium relaxation time of the nanochannel confined polymer, the quantity we argue should set the prefactor time-scale. We estimate $\tau_o \sim 10\,\text{s}$ using the values for lambda-DNA in Reisner *et al* [67] and scaling to T4, using the Rouse result that $\tau \sim L^2$ with L the DNA contour length. We find that τ is around 2 minutes using a $P = 50\,\text{nm}$ and $d = 20\,\text{nm}$. Note that simply dropping the pore size to 10 nm will increase the trapping time 10-fold, far above the time-scale of any conceivable measurement. In addition, the nanochannel confined molecule has a higher free energy relative to the unconfined molecule in the bulk reservoir [97]. This higher free energy will give rise to an entropic recoil force that will gradually drive the molecule out of the channel. We argue, however, that the molecule will only feel this recoil force in the event that it crosses the bending barrier, so it is the bending energy that is relevant to determining the trapping time-scale.

We have also introduced DNA into pore-interfaced nanoslit/nanocavity devices (figure 3–8, supplementary video 2). The nanocavities act as entropic traps, effectively catching and isolating single passing DNA molecules. Depending on the detailed geometry of the cavity array (e.g. cavity diameter, slit depth and cavity spacing) a polymer will straddle and fill multiple cavities or just one [90] . For the $567\times567\,\text{nm}$ cavities with 817 nm spacing shown in figure 3–3 c we expect lambda DNA to straddle two cavities. Just as is the case for nanochannels, nanocavity trapped DNA will remain in a cavity containing a sub persistence sized pore due to the free-energy barrier for loop

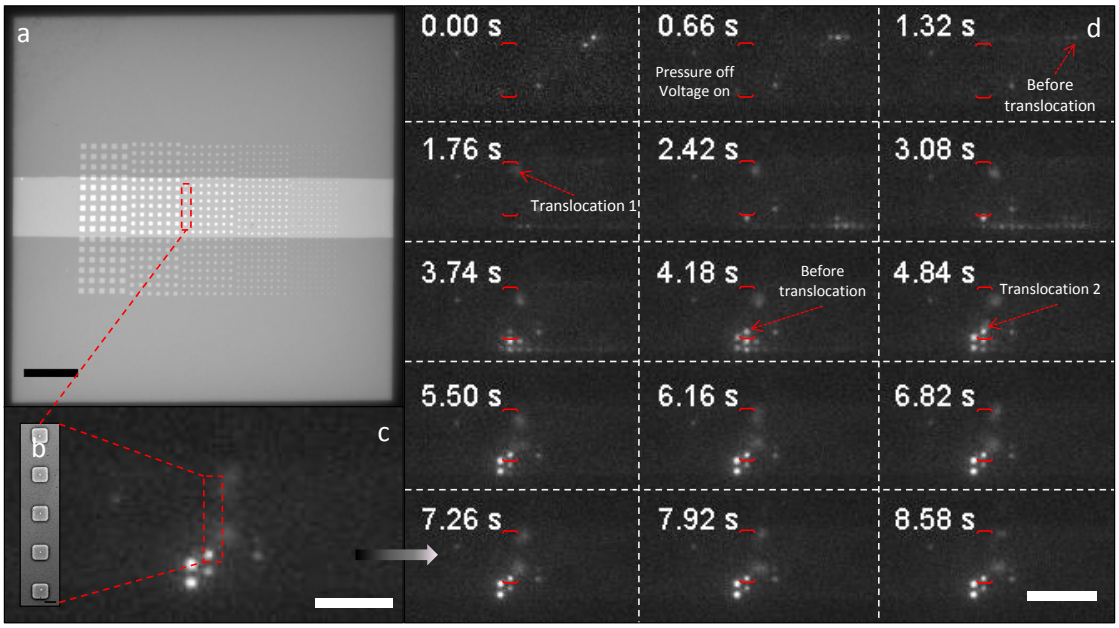

Figure 3–8: DNA dynamics in nanocavity containing multiple pores. (a) TEM image of the nanocavity array in the nanochannel and silicon nitride window (scale bar is 10 μm). (b)-(c) Zoom-in of fluorescent microscope image at time 7.26 s shows the precise location of the pore containing cavities. We also show a TEM image of the nanocavity array containing various sized pores (scale bar 400 nm) to indicate the positioning of cavity containing pores relative to the fluorescence micrograph in c. (d) Time trace of the location of lambda DNA molecules inside a nanocavity device (see also supplementary video 2). The relative location of the nanopore array is marked by red brackets. Initially, both air pressure and voltage are turned off. A single DNA molecule is trapped in the nanocavity toward the top edge. At time 0.66s, a negative voltage (-800 mV) from the right side of the cavity through the nanopore is applied. The first trapped molecule at the top edge rapidly moves towards a nanopore and translocates (translocation 1). From time 1.32 s to 4.18 s, DNA molecules at the right side of the cavity move towards the nanopore array and are trapped in the row of pore-containing cavities and an adjacent row. At time 4.84s, a second DNA molecule successfully translocates (translocation 2). From time 5.50 s to 8.58 s the two DNA molecules that have escaped the slit are observed diffusing in the backside reservoir.

formation. However, when we apply a voltage across the nanopore in excess of around 0.8 V, DNA molecules will translocate through the pore, crossing from the nanoslit to the device backside.

3.5 Conclusion

In conclusion, we demonstrate that nanochannel extended DNA molecules can be driven across an embedded pore or reversibly translocated through the pore upon application of a potential bias. In particular, this finding suggests that the pore could be used as a nanoscale "window" with which to probe nanochannel extended molecules, or permit chemical interactions between the molecule and analytes in the membrane interfaced macro-reservoir. As the reservoir contents can be easily exchanged, this would serve as an efficient way of performing chemical exchanges directly in the nanochannel while keeping the DNA confined. Moreover, the ability to pull a molecule out of the channel might function as a convenient way to extract an optically-mapped molecule for further analysis, including next-generation sequencing. One could imagine, for example, that a barcode would be used to identify molecules corresponding to a specific region on the genome, perhaps a disease-specific locus containing a translocation. The molecule would then be extracted from the channel via the pore for targeted sequencing that would identify the exact position of the translocation break-point. Future work will focus on incorporating local electrodes near the pore for combining blockade-based electrical with optical measurements.

CHAPTER 4
Nanopore Fabrication via an Atomic Force Microscope

Chapter 4 presents a novel AFM-based method for reliably locating and 'drilling' nanopores, which have already proven to be effective sensors for single molecules such as DNA and protein, in thin silicon nitride membranes using dielectric breakdown.

Using a Conductive Atomic Force Microscope Tip to Fabricate Nanopores via Local Dielectric Breakdown

Yuning Zhang, Yoichi Miyahara, Peter Grutter and Walter Reisner.

4.1 Abstract

We have developed a novel technique for fabricating nanopores on silicon nitride membranes using atomic force microscopy (AFM) with conductive tips. By applying a local voltage bias across the nitride membrane through the tip in contact mode AFM under ambient conditions, surface material is locally removed via a combination of dielectric breakdown, thermal melting and mechanical deformation, forming a nanoscale pore. Pore positioning can be readily controlled by controlling the position of the AFM tip.

4.2 Introduction

Recent advances in nanopore technology have made the pore structure an increasingly important and attractive tool for studying bio-molecules such as DNA and

proteins [3, 40, 98]. By monitoring fluctuations in the trans-pore electric current during bimolecular transit through the pore, nanopore detectors can sense single-molecules and yield structural information, including DNA sequence [32]. Compared with the classical sequencing technologies (first and second generation DNA sequencing [99]), nanopores have extremely high read lengths (up to 500 kb) and are label-free.

During the early years of nanopore technology (1990s to early 2000s), research was focused on biological nanopores [3, 98]. However, biological nanopores have several disadvantages including low mechanical stability of the supporting lipid membrane resulting in limited pore lifetime; need for well-controlled experimental conditions (e.g. specific temperature and pH range) in order to maintain the protein pore and support lipid layer structure and poor CMOS and micro/nanofluidic device compatibility. To overcome these challenges, researchers developed approaches for fabricating nanopores on thin membranes such as silicon nitride, silicon dioxide and graphene, referred to as "solid state nanopores". The most commonly used pore production approaches employ high energy beams to sculpt individual pores via local ablation of substrate material. Particle beam approaches include ion beam [28], electron beams generated in a transmission electron microscope (TEM) [29] and focused ion beam (FIB) [100]. The particle beam approaches are necessarily serial (one pore made at a time) and require expensive instrumentation, including high vacuum systems, found only at specialized facilities, increasing cost per pore and pore production times. Developing a more cost effective pore fabrication method could potentially accelerate research in the nanopore field and enable faster dissemination of pore technology outside academia

In 2013, a simple method for fabricating nanoscale pore was proposed by Kwok *et al.* [19]. By directly applying a voltage across an insulating membrane in electrolyte solution they were able to fabricate a single nanopore down to 2 nm in size. The applied

voltage induces a high electric field across the thin membrane; this field is so strong that it can induce dielectric breakdown of the membrane, leading to the opening of pores. Yanagi *et al.* [101] used this technique with pulsed voltage control to fabricate pores in 10 nm nitride films with diameters ranging from less than 1 nm to 3 nm. In the pulsed voltage approach, the pore is first formed with high voltage (7 V) pulses; the size is then tuned with mid-voltage pulses (2.5-3 V). Pores can be formed with pulse-control with a success rate of around 90%. The dielectric breakdown method is simple, fast, inexpensive and has great potential for micro/nanofuidic device integration.

While the dielectric breakdown method can produce inexpensive and high quality nanopores, there are two key disadvantages. Firstly, the positioning and size of the pore are random. The dielectric breakdown effect occurs at the weakest spot of the insulating membrane when a breakdown voltage is applied. The position of the weakest spot is, however, determined randomly by the inhomogeneity of the nitride films created by low stress plasma enhanced chemical vapor deposition process (PECVD). Consequently, the pore could be formed at any position on the membrane in contact with the liquid reservoirs, potentially a very large surface area. Secondly, the technique can not produce multiple nanopores or nanopore arrays with controlled spacing between pores.

Here we present a novel method for nanopore fabrication combining atomic force microscopy and the dielectric breakdown technique (see figure 4-1). A voltage up to 15 V is applied across the 10 nm silicon nitride membrane between a conductive AFM tip (placed above membrane) and a brass electrode (placed below membrane). The top surface of the membrane, where the AFM tip is positioned, is exposed to air; the region below the membrane, where the brass electrode is positioned, is immersed in a 1 M KCl solution. After application of the voltage, nanopores are formed in

the nitride membrane, due to the combination of dielectric breakdown effect, thermal melting effect and mechanical deformation. Nanopores are subsequently imaged using AFM and TEM. With this technique we are able to fabricate either single nanopore or nanopore arrays on 10 nm silicon nitride membranes. The classic dielectric breakdown technique is limited to applications that do not require control of the nanopore position. In contrast, with our approach, the pore can be positioned with the AFM tip, allowing for precision alignment with pre-existing device features (e.g. channels and electrodes, the location of which can be obtained in situ via the AFM tool's imaging capability). In particular, this approach could facilitate the creation of transverse electrode integrated pore structures [102], which require the positioning of the pore precisely between the electrodes. As another example, our approach could position a pore inside a nanofluidic channel. While such fine positioning can also be achieved with the conventional TEM nanopore drilling technique, with our AFM approach, pores can be made in ambient conditions (e.g. atmospheric pressure and normal indoor humidity) and we dispense with the inherently high costs (fixed and maintenance related) of a particle beam tool.

Lastly, our AFM approach is well suited for wafer level scaling of nanopore production. TEM's can only accommodate extremely small samples ($< 1 \times 1$ cm). While's wafer-scale FIB tools are relatively common in advanced fabrication facilities, the requirement of large vacuum chambers to handle 8 in wafers increases the expense of these tools. The required vacuum conditions may also damage sensitive chemical patterning on the devices. In addition, AFM tools can be in principle multiplexed so that multiple tips can be scanned at once, permitting truly parallel pore fabrication.

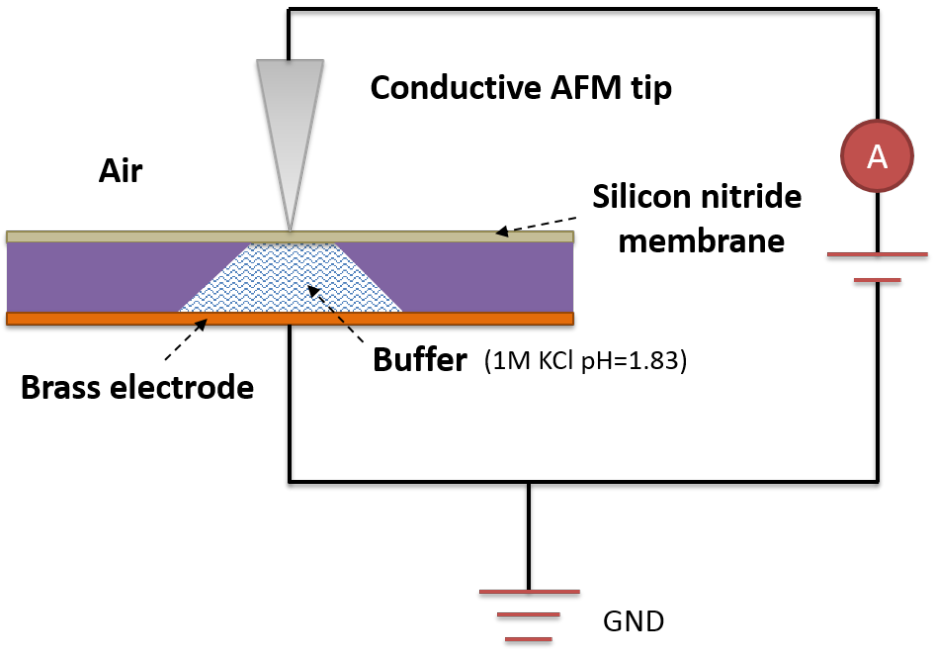

Figure 4–1: A diagram illustrating the AFM based dielectric breakdown technique for nanopore fabrication. A voltage is applied across the silicon nitride membrane between the top side conductive AFM tip and the bottom side brass electrode, immersed in KCl buffer.

4.3 Experimental Setup

The nanopore fabrication setup consists of three parts: a custom assembled AFM setup (figure 4–2 c), the fluidic cell (figure 4–2 a and b), and an imaging and controlling system (PC). Figure 4–1 is a schematic detailing the AFM dielectric breakdown setup. A DC voltage ranging up to +15 V is applied across the membrane between the conductive AFM tip and the brass electrode. The fluidic cell chamber is filled with electrolyte (1 M KCl, pH=1.83). With this setup, we have successfully fabricated multiple nanopores in 10 nm thick silicon nitride membranes.

4.3.1 Materials and Methods

Dielectric Membranes

We use commercially available thin nitride membranes (Norcada, NT001Z). The silicon nitride membrane is fabricated via low stress LPCVD with a residual film stress of less than 250 MPa. The thickness of the membrane is 10±0.7 nm with a free standing window size of $50\times50\,\mu m^2$. The 200 μm thick silicon frame is octagon shaped with a maximum diameter of 3.0 mm. The dielectric strength of the membrane is about 10^9 V/m [103]. Accordingly, the required breakdown voltage for a 10 nm silicon nitride membrane will be in the order of 10 V. The resistivity of the membrane is $10^{16}\,\Omega$ ·cm, the Young's modulus is 270 GPa and the surface roughness(Ra) is 0.36±5% nm, respectively [103].

AFM tips

Two different types of AFM tips are used in our experiments PtSi-FM tip (commercially available from Nanosensors) and conductive diamond tip (commercially available from Adama Innovations). The NANOSENSORS PtSi-FM tip has a resonance frequency of 75 kHz, a force constant of 2.8 N/m and a tip radius of curvature is around 25 nm. The AFM tip is coated with PtSi, conferring a tip resistivity of $\sim 3\times10^{-5}\,\Omega$·cm, almost comparable to the resistivity of a typical metal ($\sim 2\times10^{-6}\,\Omega$·cm).

The Adama innovations conductive diamond tip is prepared by coating the tip with a thin layer of ultrananocrystalline diamond (UNCD) film. By varying the film growth conditions, the electrical conductivity of the UNCD coating can be adjusted to be either conductive or insulating. For our experiments, we use a resistivity between 3.0×10^{-3} to $5.0\times10^{-3}\,\Omega$·cm, which is about 100 times higher than the PtSi-FM tip but still significantly less than that of silicon nitride membrane ($\sim 10^{16}\,\Omega$·cm). The

force constant is 2 N/m for AD-2-ASA or 10 N/m for AD-10-ASA tip. The tip radius is 10 ± 5 nm.

Fluidic Cell Design

We designed a special fluidic cell to enable simultaneous probing of the membrane top side with the AFM tip while keeping the membrane bottom side immersed in electrolyte solution. The fluidic cell is made of poly(methyl methacrylate) (PMMA) plastic and allows the direct mounting of a membrane containing silicon frame TEM chip. The chip is sandwiched between a top brass retaining lid and a top O-ring, sealing the reservoir containing an aqueous solution of 1 M KCl, as shown in figure 4–2. The bottom part of the fluidic reservoir is sealed by an O-ring and a brass electrode. The brass electrode connects to a custom-built voltage amplifier that provides a trans-membrane potential ranging from -15 V to 15 V. The top brass retaining lid is fixed to the fluidic cell body via plastic M2 screws. We then apply silver paste at the bottom of the cell (underneath the brass electrodes) in order to minimize contact resistance. The cell is mounted on the AFM sample stage which is then placed on an optical table for vibration isolation.

Equivalent Electric Circuit

The AFM tip, electrolyte and the bottom brass electrode constitute three resistors connected in series. The resistivity of the AFM tip is $\sim 3\times10^{-5}\,\Omega$·cm for the Pt-Si tip and 3.0×10^{-3} to $5.0\times10^{-3}\,\Omega$·cm for the diamond tip, significantly less than the resistivity of silicon nitride membrane ($10^{16}\,\Omega$·cm). The electrolyte can be considered as a conductor. Consequently, even though the membrane thickness is only 10 nm, the resistance of the nitride film dominates and the potential applied across the nitride film is almost equal to the voltage supplied by the amplifier.

Tip Enhanced Electric Field

Another distinct advantage of using conductive tip for dielectric breakdown nanopore fabrication is the tip induced local electric field enhancement. While the critical electric field of performing electric breakdown to make a nanopore on nitride memebrane can be estimated from a classical parallel-plate capacitor model. In our experiment, the membrane is connected by a conductive tip with nanometer sized radius of curvature, in which the electric field can have an local enhancement factor up to 100 – 1000 according to previous researches [104, 105]. The strongly enhanced local electric field can potentially shortens the time for dielectric breakdown process significantly.

4.4 Results

4.4.1 Pore production protocol

The full nanopore fabrication process consists of three steps: pre-scan of the nitride membrane, the fabrication of nanopore and re-scan of the membrane after fabrication. For the pre-scan and re-scan, AFM imaging is performed in contact mode. The detailed operating parameters are: scan size 500-1500 nm, scan rate 2 Hz, zero bias voltage, 0.1 V deflection voltage and a 128 s scan time. The deflection voltage controls the force exerted by the tip against the membrane. This parameter has an optimum value for pore formation, which will be discussed later. During the pore production step the AFM tip is held at the same location (scan size 0 nm) while a bias voltage (-15 to +15 V) is applied for a fixed time duration, referred as 'load-time', to open the pore. The load-time used is in the range of 128-256 s. Figure 4–3 demonstrates successful fabrication of a dual-nanopore arrangement with a 500 nm pore spacing. The pores were created via a PtSi-FM tip with a bias voltage of 10 V and a load time of 128 s. Figure 4–4 shows the nitride membrane before and after pore fabrication. Concave indentations in the surface indicate the presence of the pores.

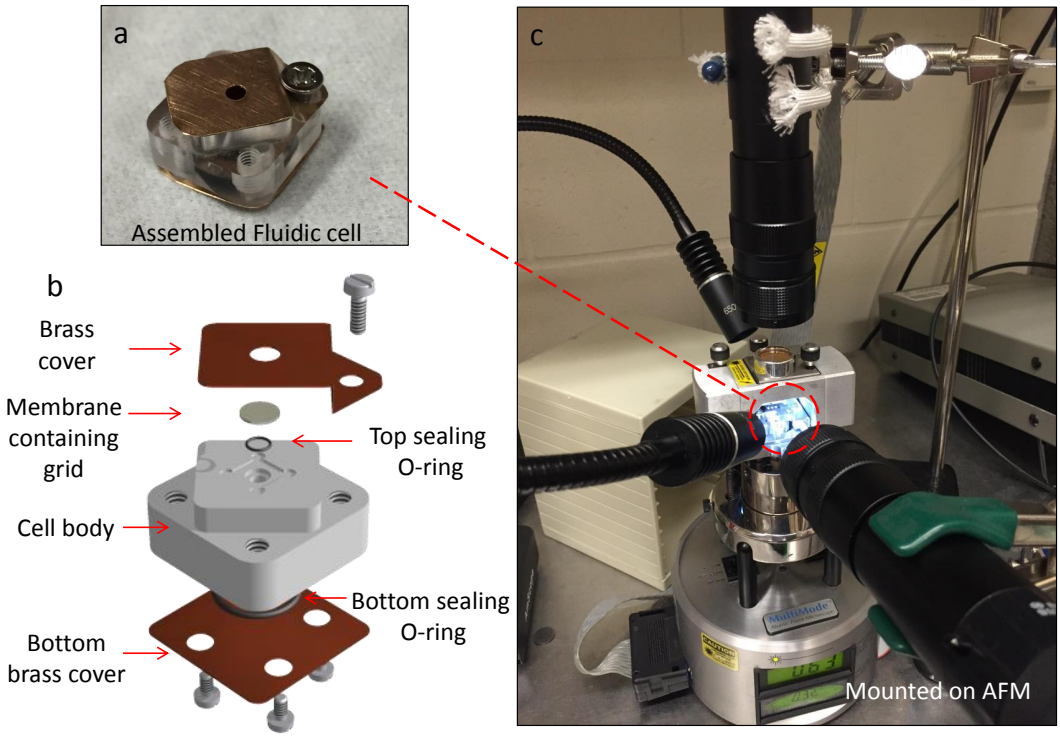

Figure 4–2: a) The assembled fluidic cell containing a 10 nm thick silicon nitride membrane chip ready for nanopore drilling. b) A 3D view of the fluidic cell. The nanopore chip is sandwiched between the top brass cover and top sealing O-ring. c) Photograph showing the fluidic cell mounted on the AFM sample stage and illuminated by the light source used for bright field microscopy inspection.

4.4.2 TEM nanopore characterization

Dielectric materials, like silicon nitride, can store charge [106]. Since the dielectric breakdown process induces charging close to the membrane, it is conceivable that the pore shapes we observe in our topography scan could result from electrostatic interactions (e.g. due to residual charge build-up on membrane surface) rather than a true pore topography. In order to rule out this possibility, and characterize pore shape with higher resolution, we imaged the membrane with TEM after nanopore fabrication.

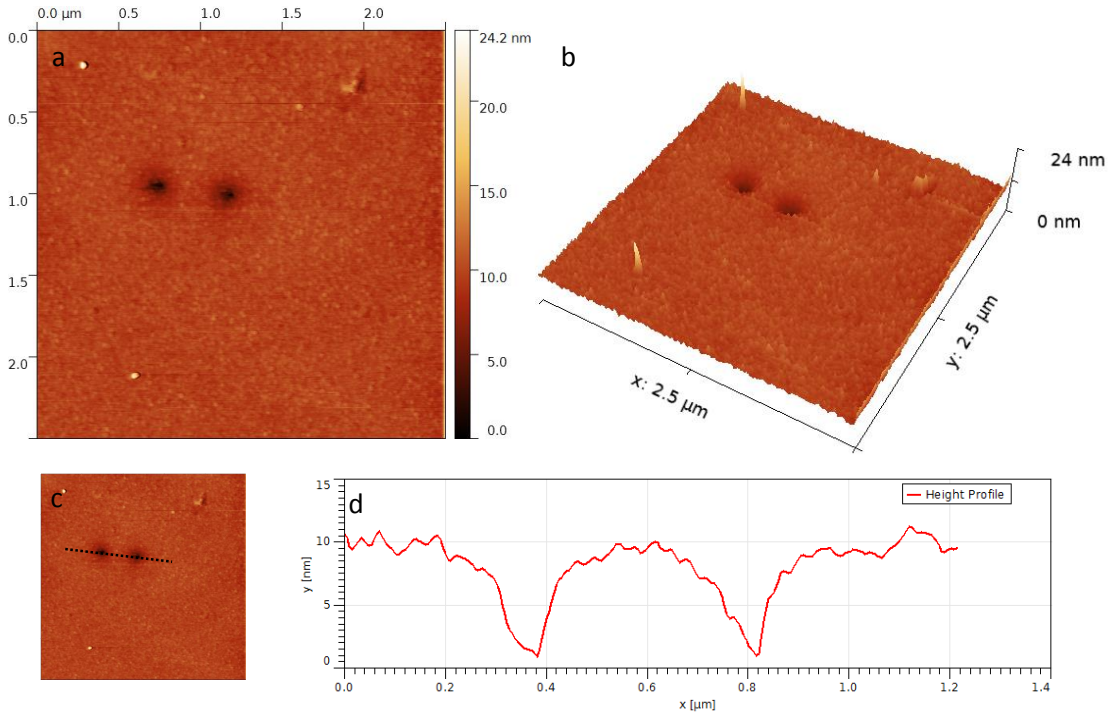

Figure 4–3: The double-nanopore fabricated via conductive AFM (C-AFM) dielectric breakdown technique. a) The contact mode AFM image of a double nanopore fabricated on 10 nm thick silicon nitride membrane via dielectric breakdown. b) 3D view of the image showing physical concaves on the nitride membrane indicating a double nanopore. c) A 1.2 μm long line scan across the pores corresponds to the height profile shown in d). AFM settings for pore drilling: scan size 0 nm, bias voltage 10 V, deflection voltage 1.00 V, load time 128 s.

In order to prepare membranes for TEM imaging, we first cleaned the membrane containing TEM grid in DI water for 60 minutes to remove precipitated salt and then in Piranha for 15 minutes to remove any organic contamination. The nitride membranes were then imaged using a JEOL JEM-2100F TEM at 200 kV. TEM images of the fabricated nanopore are shown in figure 4–5, indicating that the well-defined pores are present in TEM images as well as the AFM scans.

A nanopore array in the silicon nitride membrane is created with the conductive diamond tip using the following AFM settings: scan size 0 nm, bias voltage 10 V,

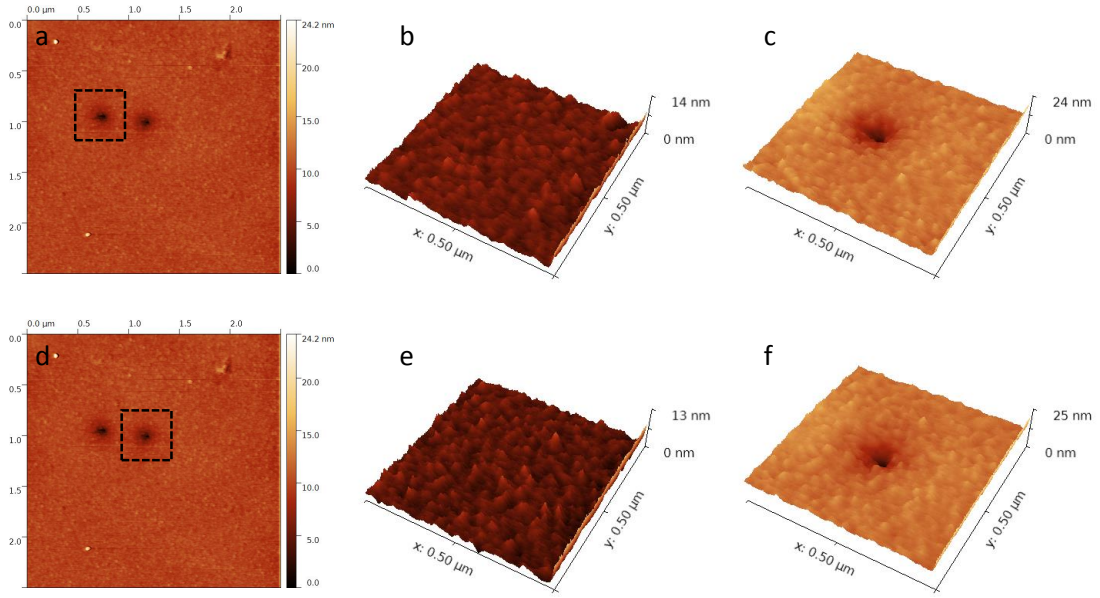

Figure 4–4: Higher resolution AFM image of the same double-nanopore shown in figure 4–3 **before** and **after** nanopore drilling. b) & c) Contact mode AFM scan before and after drilling for the left nanopore. e) & f) Contact mode AFM scan before and after drilling for the right nanopore. The AFM images of the two individual pores fabricated under the same drilling conditions look very similar, implying the technique has high reproducibility.

deflection voltage 1.00 V, load time 256 s. The nanopores are labeled as 1 to 5 in figure 4–5. Nanopores are evenly spaced (500 nm) and have pore diameters of $\sim$ 40 nm. During the last run, the deflection voltage is increased from 1.00 V to 2.00 V. The increased deflection voltage created a triangular crack on the nitride membrane (labeled as 6) propagating outwards from the pores edges (a higher magnification image is shown in figure 4–5 c). We believe this propagating crack is created by the triangular base of the silicon cantilever. The possible orientation of the base is indicated in figure 4–5 c by a red dashed tetrahedron. Thus, mechanical deformation induced by the AFM tip may also play a role in the nanopore fabrication, affecting nanopore size and shape.

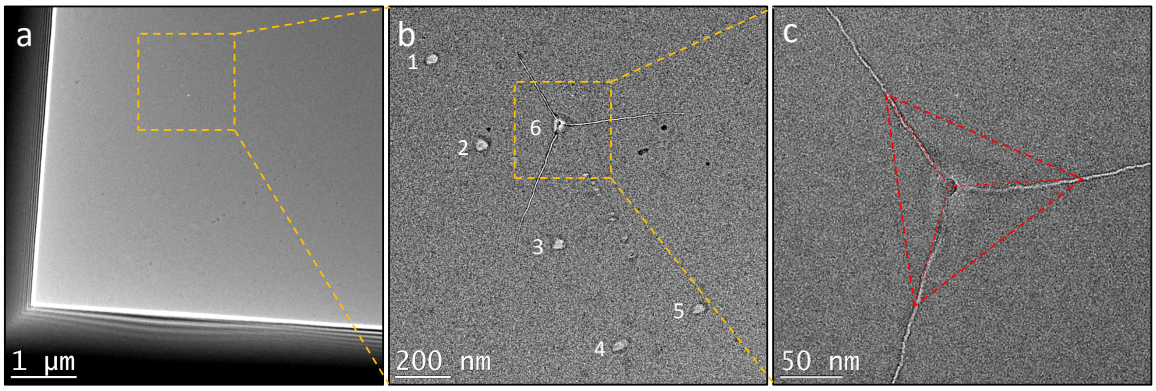

Figure 4–5: TEM characterization of nanopore fabricated by conductive diamond tip. The nanopores are fabricated using the following AFM settings: scan size 0 nm, bias voltage 10 V, deflection voltage 1.00 V (figure b 1-5) and 2.00 V (figure b 6), load time 256 s. a) A large scale TEM image shows a corner of the $50 \times 50\,\mu m^2$ where the nanopore array is located (indicated by the yellow dashed square). b) Zoomed in TEM image of the full nanopore array fabricated by the C-AFM dielectric breakdown technique, nanopores (labeled as 1 to 5) are spaced evenly at a distance of 500 nm. The nanopores have a diameter of around 40 nm. c) Zoomed in image of the triangular crack caused by the the triangular silicon base of the conductive diamond tip (the possible orientation of the silicon base is indicated by a red dashed tetrahedron).

4.4.3 Bias Voltage dependence

In order to understand the effect of bias voltage on nanopore fabrication, we have performed experiments varying bias voltage while keeping other settings fixed. The results are shown in figure 4–6. In particular, for these experiments, the membrane thickness is 10 nm, a PtSi-FM tip was used, the bias voltage ranged from 5-10 V in steps of 1 V and the deflection voltage was held at 1.00 V. We observe that pore size increases with increasing bias voltage. At bias voltage smaller than 6 V, the AFM barely detects the existence of the nanopore. The nanopores for bias voltage less than 6 V are either too small to be detected (i.e. they are smaller than the AFM tip diameter) or the voltage is not strong enough to induce breakdown and form a nanopore.

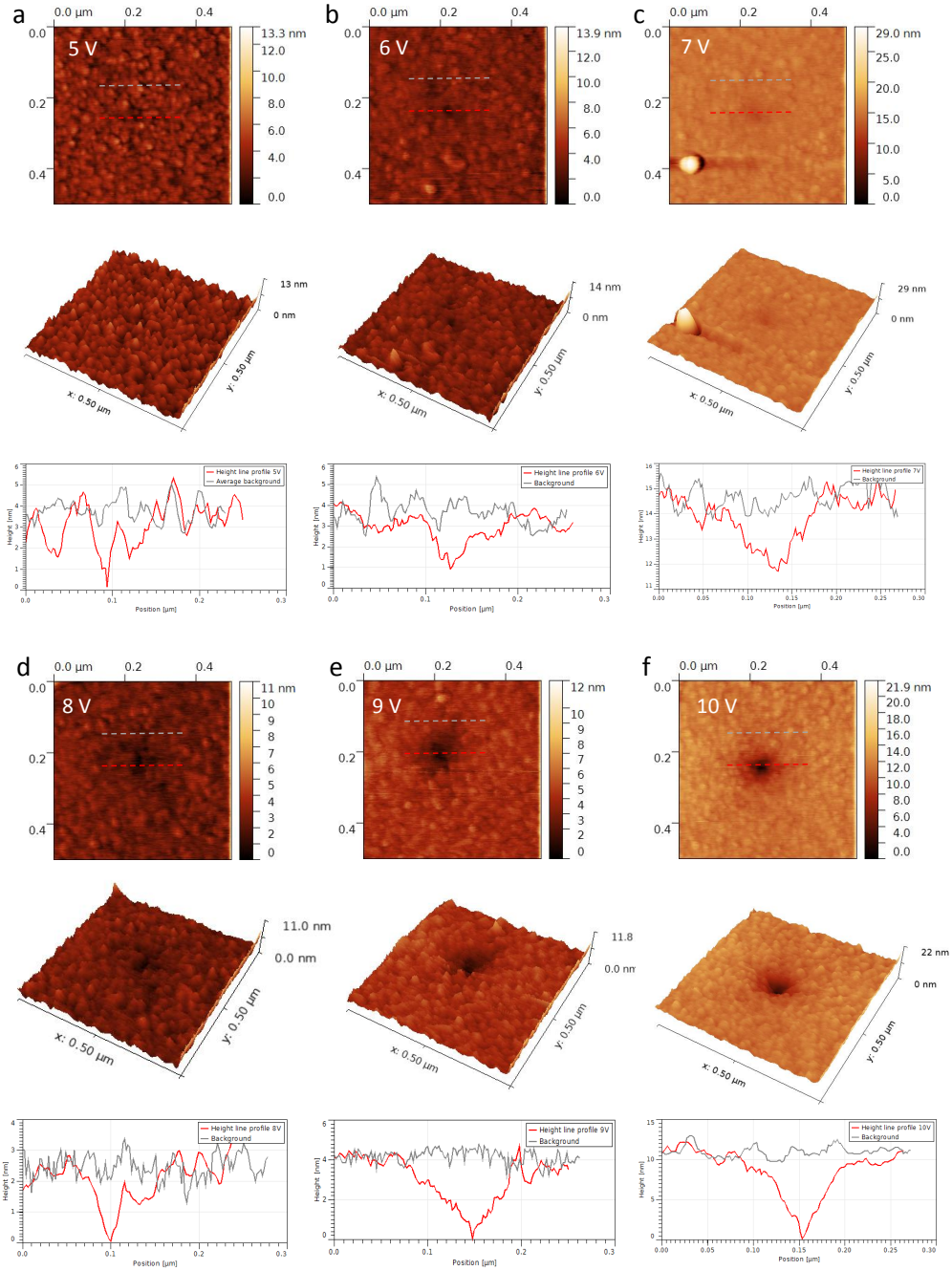

Figure 4–6: AFM images of nanopores for bias voltage ranging from 5-10 V. A 2D scan is shown on top. Below each 2D scan we show a line topography scan across the pore compared to a background topography scan (corresponding to a nearby location away from the pore). The pore just starts to form at around 7 V (figure c). AFM settings for pore drilling: scan size 0 nm, bias voltage 5-10 V, deflection voltage 1.00 V, load time 128 s.

We have also investigated reversing bias voltage polarity while keeping the other conditions fixed and identical in value to those used in figure 4–6). After reversing bias to -10 V, there is no evidence of pore formation (see figure 4–7). In order to explain the bias voltage polarity, we revisit the fundamental mechanism of dielectric breakdown and propose a model that can explain this finding as well as other recently reported findings [107, 108].

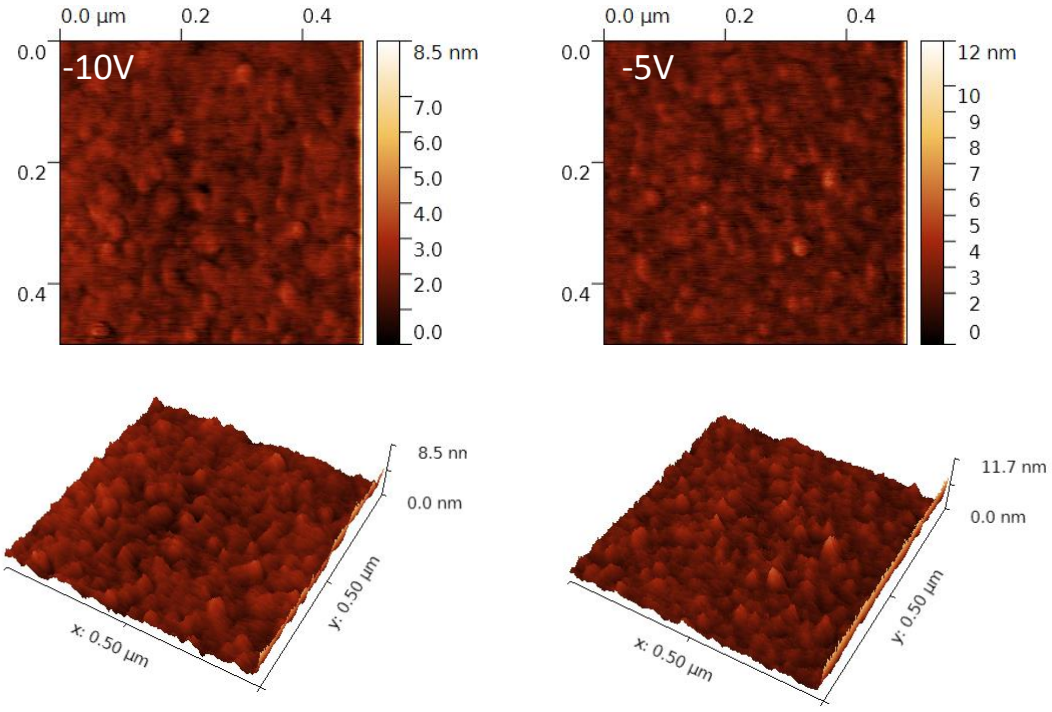

Figure 4–7: AFM images of the nitride membrane after reversing vias (-10 V and -5 V) while keeping the other conditions the same as used in figure 4–6.

4.4.4 Deflection voltage/loading force dependence

Increased tip deflection voltage can lead to membrane cracking (figure 4–5). Thus, the mechanical force introduced by the tip against the membrane is also a possible cause of nanopore formation. In order to prove that nanopore formation does involve the

dielectric breakdown effect, instead of just pure mechanical breaking of the nitride membrane by the AFM tip, we have performed control experiments with **zero** bias voltage and varying deflection voltage. In these experiments we used the following settings: a PtSi-FM tip, zero bias voltage, a deflection voltage of 0.10 V and 1.00 V and a loading time is 128 s. The 0.10 V deflection voltage value is chosen to match the default voltage for contact mode AFM imaging using the PtSi-FM tip (e.g. it is the value used during the pre-scan and re-scan steps). The 1.00 V deflection voltage value is chosen to match the default value used for the pore formation step. When we attempt to make a pore under these conditions, we find that the re-scan AFM image shows no evidence of pore formation, indicating that a non-zero bias voltage is required for pore formation and that dielectric break-down likely plays a role in the pore formation process.

In addition, we have fabricated nanopores with varying deflection voltage while keeping the bias voltage fixed (see figure 4–8). Even with the deflection voltage used for imaging (0.10 V) a nanopore formed. The size of the nanopore formed increases as the deflection voltage increases. Thus, we can conclude the presence of the bias voltage is necessary for the creation of a nanopore, while the deflection voltage is not strictly required for the nanopore formation. Increasing the deflection voltage, however, mechanically deforms the nanopore (increasing pore size and changing pore shape). To summarize, while the fundamental pore generation mechanism is dielectric breakdown, the size and shape of the pore formed are altered by mechanical deformation introduced by the AFM tip.

4.5 Nanopore Formation Mechanism

Dielectric breakdown is intrinsically an electric conduction process in solids. In order to better understand the dielectric breakdown mechanism, we will first review basic

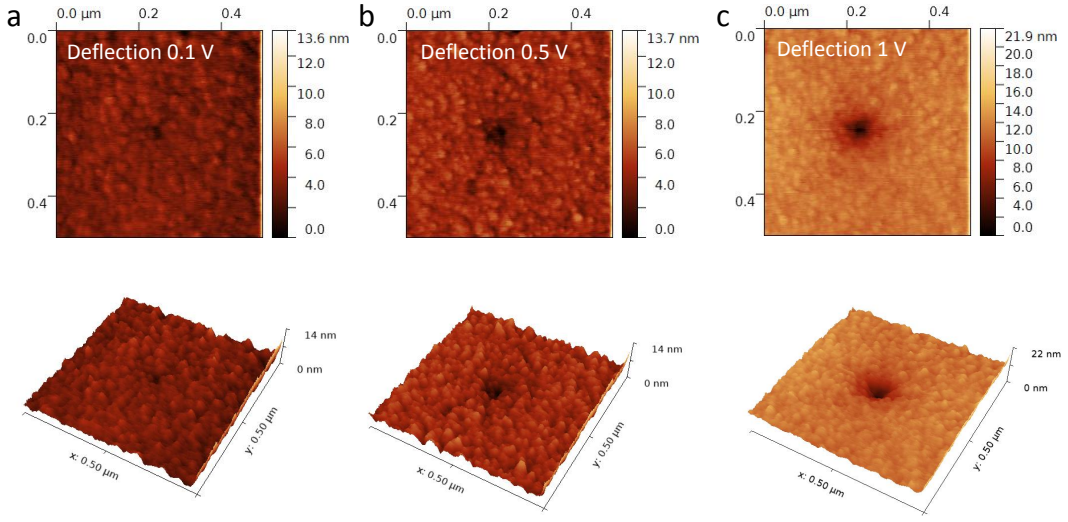

Figure 4–8: AFM images of nanopores fabricated using different deflection voltage values (0.1, 0.5, 1.0 V) while keeping other parameters fixed (PtSi-FM tip, bias voltage 10 V, load time 128 s).

physics of conduction in solids and then discuss the dielectric breakdown mechanism in detail.

4.5.1 Conduction in solids

Electric conduction in solids is typically mediated by electron transport. However, electrons are not totally free in solids, they have to follow certain "traffic rules". An intuitive way to visualize the allowed energy states of electrons in a solid is the electronic band structure. In solid state physics, the available energy states for electrons in the materials form allowed bands and the forbidden energy states form the band gaps. The energy bands and band gaps are derived from solving the quantum mechanical wave functions for an electron in a large, periodic lattice of atoms or molecules. Band theory determines the difference between insulators, semi-conductors and conductors. The comparison of band gaps of typical insulators, semi-conductors and conductors are drawn in figure 4–9. The band gap, an energy range where no electrons states

can exist, refers to the energy difference between the bottom of the conduction band and the top of the valence band in insulators and semiconductors. In conductors, the conduction and valence band often overlap.

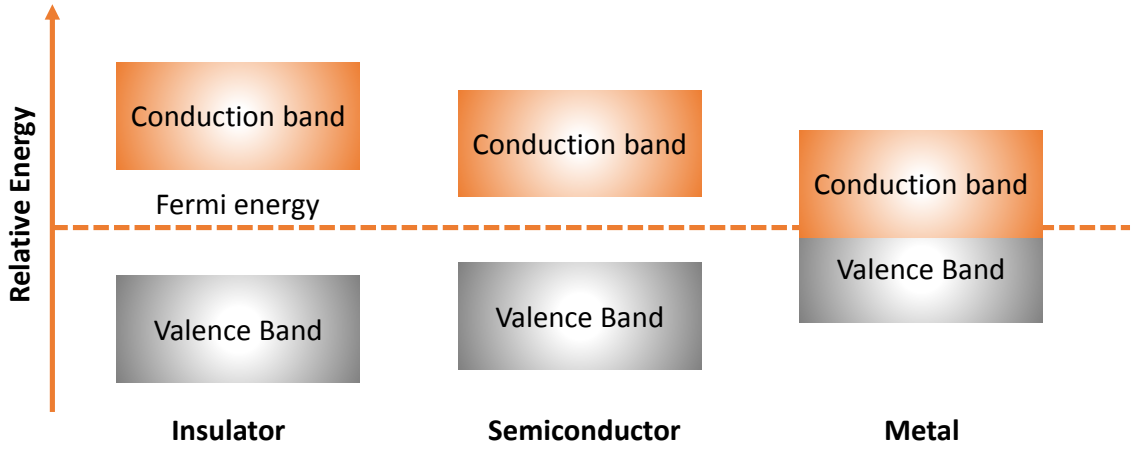

Figure 4–9: Comparison of band gaps of insulator, semiconductor and conductor(metal).

In non-metallic materials the valence band is full of electrons tightly bound to the atomic nucleus. In order for electrons to act as charge carriers and move freely, electrons in the valance band have to absorb enough energy to cross the band gap (E_g) and enter the conduction band. Thus, the size of the gap determines the conductivity. For conductors, the valance and conduction band overlap, so that electrons can move freely. For semiconductors, where there is a small band gap, electrons can move from the valance to the conduction band with the help of external energy (electric, thermal, etc.). However, for insulators, the E_g is sufficiently high that the probabilities of electrons jumping from the valence to the conduction band is negligible under normal conditions.

4.5.2 Conduction mechanisms in dielectric membranes

Insulators are typically considered perfectly non-conductive. However, insulators can conduct under certain extreme conditions, such as high applied electric field and high temperature. Understanding the conduction mechanisms in insulating (dielectric) films is the key to the success of a variety of dielectric material applications and is also crucial for better understanding the dielectric breakdown effects in our experiments. Generally, the conduction mechanism in dielectric films can be classified as electrode-limited and bulk-limited [109]. The electrode-limited mechanism depends on the electrical properties at the electrode-dielectric contact; the bulk-limited conduction mechanism depends on the electric properties of the (bulk) material itself.

Quantum mechanical tunneling of electrons, an important class of electrode-limited conduction mechanism, describes the transition of electrons through a classically forbidden energy state [109]. The original interest in quantum mechanical tunnelling of electrons comes from efforts to enhance the performance of MOS devices in the semiconductor industry. Due to the constant downscaling of dielectric gate thickness in modern MOS devices, electrons can tunnel through the dielectric layer to the gate contact of a MOS structure. Two tunnelling mechanisms are of particular interest to us: direct tunneling, and Fowler-Nordheim tunneling (a special case of direct tunneling) [109].

Electronic direct tunneling through a dielectric, illustrated in figure 4–10 a, happens only when the insulating material is very thin (on the order of 2-4 nm) [110, 111]. Quantum mechanical tunneling theory predicts that the electronic tunneling probability is determined by the width and the height of the barrier. The barrier width is determined by the dielectric thickness and the barrier height is determined by the energy difference between the conductor's Fermi level and the insulating material's

conduction band. Direct tunneling through thin silicon nitride, metal oxide and silicon dioxide membranes have been extensively studied for better development of semiconductor devices [112, 113, 114]. Recently researchers have reported the charge trapping and tunneling characteristics of MNOS (metal-nitride-oxide-semiconductor) transistor as a function of nitride layer thickness [115]. This work suggests that once the silicon nitride membrane thickness increases above 4 nm the tunneling current dramatically decreases and charge trapping efficiency increases.

Fowler-Nordheim tunneling is a special case of direct tunneling (figure 4–10 b). When an external electric field is applied across the dielectric material, the energy band is tilted. When the dielectric material is sufficiently thin or the external electrostatic field is sufficiently strong that electrons can tunnel across the barrier into the conduction band of the dielectric material, an electron can move freely from the dielectric to the conductor.

The Poole-Frenkel emission is one of the most common bulk-limited conduction mechanisms. As illustrated in figure 4–10 c, defects (charge traps) in the dielectric material create intermediate energy levels in the band gap allowing electrons to jump from the left conductor in to a defect in the insulator. The trap-assisted electron transport process continues until the electrons reach the conductor on the right. Realistically, when we consider an insulating membrane, it is not a perfect single crystal. During the fabrication process (usually via thin membrane deposition process such as PECVD, LPCVD, ALD), structural defects (doping atoms, vacancy, interstitial, etc.) or doping atoms are introduced into the the membranes. Also due to the high electric field, defects can be generated at the surface or in the bulk material by various causes: impact ionization, anode hole injection and hydrogen atom assisted trap creation [116, 117, 118, 119].

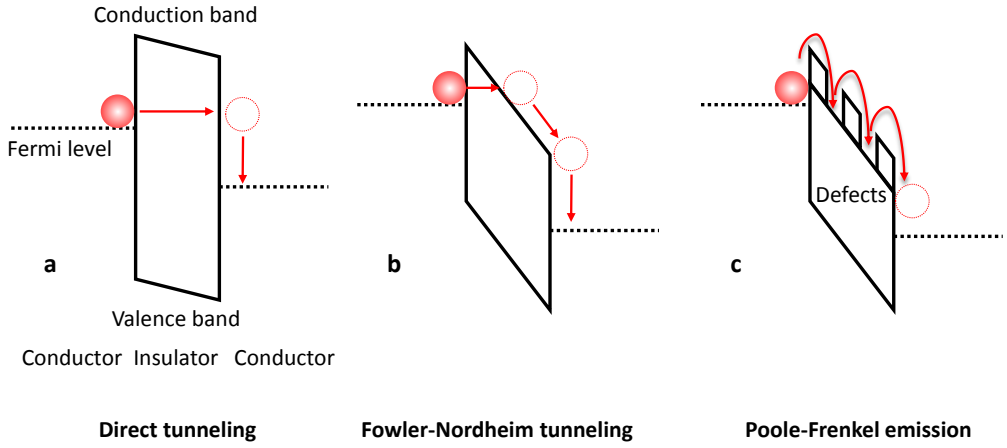

Figure 4–10: The energy diagram of three different electron conduction mechanisms in dielectric materials. a) Direct tunneling. b) Fowler-Nordheim tunneling. c) Poole-Frenkel emission.

4.5.3 General dielectric breakdown mechanism

Dielectric breakdown of thin insulating membrane devices in dry environments have been extensively studied both theoretically and experimentally by semiconductor researchers attempting to improve the performance of MOSFET devices [120]. The breakdown mechanism in the case where liquid is present on one side of the membrane, or or both sides has also been investigated [121, 122, 123, 107]. While a number of different theories have been proposed, the fundamental physical mechanisms behind dielectric breakdown are still unclear. The basic outline shared by most of the proposed models is as follows:

1) a large local electric field applied across the material introduces charge traps (defects) in the material. These charge traps act to increase the local conductivity, creating a state intermediate between the valance and conduction band, so that electrons can tunnel freely between the traps under the influence of the external electric field.

The typical tunneling distance of electrons per trap is on the order of a few nanometers [124, 125].

2) The charge traps (defects) are stochastically created at the surface or in the material bulk. Once a connected path of these traps is created that spans the sample, a conductive path or "electron highway" is formed.

3) Once the conductive path is created, electrons can move though the material leading to current leakage. Due to the Joule heating created by the leakage current, the material is physically damaged, creating a physical tunnel in the material (in our case, a nanopore). This effect is also termed as thermal breakdown. The damage done to the material is permanent and irreversible.

The formation of charge traps is the key for better understanding the breakdown mechanism. These charge traps can be any possible defects (such as doping atoms, vacancy, interstitial, etc.), illustrated in figure 4–11. The physical origin of these defects is still unclear, however several possible mechanisms for trap formation are listed, including hole injection, impact ionization under high electric field and hydrogen assisted trap creation [116].

4.5.4 Anode hole injection model

As discussed in the previous subsection, a number of dielectric breakdown mechanisms have been proposed [120]. To the author's knowledge, researchers in the dielectric breakdown nanopore field have been using the stochastic trap generation model to explain the nanopore formation [19, 107, 101, 108]. However this model doesn't elucidate the physical mechanism governing the formation of charge traps in dielectric materials induced by strong electric field and also assumes the trap generation to be stochastic, which can be misleading.

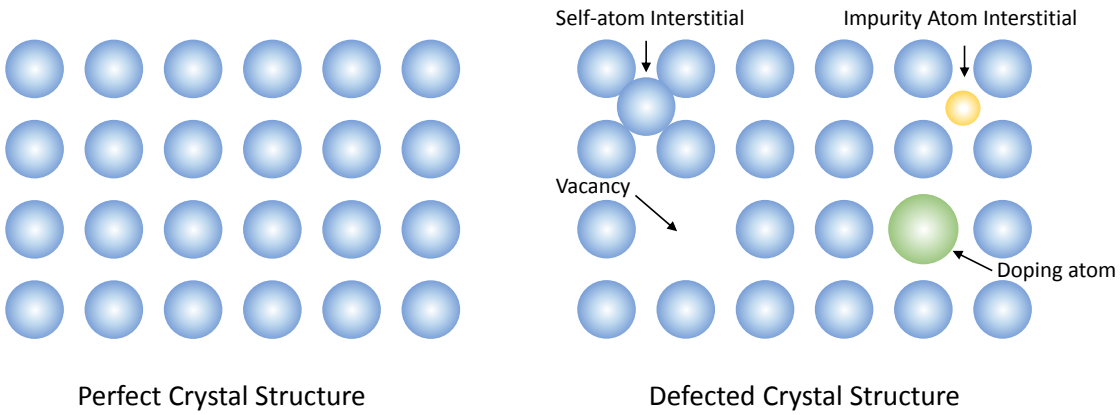

Figure 4–11: The comparison between a perfect lattice structure and lattice structure with defects in 2D. Most common defects, such as vacancy, doping, self-atom interstitial and impurity atom interstitial, can modify material properties (e.g. band gaps, conductivity, hardness, melting temperature).

Recently, researchers reported 3D nanopore shape control via controlled pulse dielectric breakdown [108]. They demonstrated that pore core orientation can be determined by changing pulse polarity. Once a pore is formed, the larger opening of the pore is bias dependent and will always be on the anode side. The authors use electric double layer effects to explain the voltage polarity of the pore formation process.

When emerged in electrolyte, the silicon nitride membrane will be negatively charged, due to the formation a native oxide layer [126], only several atom thick, on the nitride surface while exposed to air. The charging of the membrane will naturally cause the formation of a electric double layer near the membrane surface. The negatively charged surface will attract a thin layer of positive ions from the electrolyte (H^+ and K^+), forming an immobilized positive Stern layer (in addition to the diffuse layer extending into solution). The local electric field introduced between the Stern layer and the nitride surface is so strong near the material surface that it will cause physical defects and introduce charge traps into the dielectric [108]. When the charge trap

density becomes sufficiently high, a transmembrane conductive path will be formed by random traps. A large fluence of electrons flows through the dielectric material and produces Joule heating, eventually causing physical breakdown of the dielectric membrane and forming a nanopore. However, if a negative bias is applied to the surface (the cathode), the concentration of the positive charged ions in the Stern layer is lower [127], resulting in a weaker local electric field. The weaker local electric field will induce charge traps with lower probability, leading to a smaller chance of inducing breakdown, consequently giving rise to asymmetry in how the bias polarity effects pore formation.

The stochastic trap generation model (with EDL) provides a reasonable explanation for the asymmetric effect, yet there are some problems. In particular, the authors fail to provide a fundamental charge trap formation mechanism and address how the high local electric field induces charge traps in the dielectric material. Additionally, the model is only valid when both sides of the membrane are immersed in electrolyte and consequently cannot explain the asymmetric voltage polarity dependence reported in the semi-wet condition observed in our AFM nanopore experiment (figure 4–7, only one side of the membrane is immersed in an electrolyte).

We propose an alternative model, termed as the **anode hole injection model**, which will not only elucidate the physics of dielectric breakdown but also provide an explanation for the origin of asymmetric voltage polarity effects observed by us and other workers [107, 108]. The anode hole injection model (AHI) was originally proposed in the 1980s to explain electric breakdown in thin dielectric layers used in semiconductor devices [128, 129, 130]. This model suggests that electrons, when they reach the anode, are able to elastically transfer excess energy to electrons deep in the anode valence band via impact ionization [128, 129]. The excited valance electrons are promoted to the lower edge of the conduction band leaving a "hot" hole behind. These hot holes can

then tunnel back into the dielectric generating charge traps, probably through hole-induced trap generation (hole-trapping will eventually turn into an electron trap) [129, 130]. In turn these traps increase the current density inside the dielectric due to trap-assisted electron tunneling (electron hopping) and/or Poole-Frenkel emission, leading to an electron runaway process that ends in breakdown [131, 132, 133]. In addition, the recombination of trapped holes and electrons can also lead to permanent defects in the dielectric material (most likely neutral traps), which could further increase local current through trap assisted tunneling [134]. According to AHI model, breakdown occurs when a critical hole fluence is reached (about $0.1\,\mathrm{C/cm^2}$ for a 11 nm thick oxide [130]). However, the AHI model does not apply for ultra thin dielectric membranes (below $\sim 4\,\mathrm{nm}$), for which direct tunneling (including Fowler-Nordheim tunneling) effect takes over and dominates.

The AHI model suggests that breakdown is a two-step process. The first step takes time, up to years, when the dielectric material is slowly damaged under electric field. The second step is a very short electron runaway process, on the order of microseconds, where a conductive path is formed through the dielectric material [130]. The massive fluence of electrons lead to Joule heating effect and result in localized melting in the dielectric material [135].

As discussed, we have observed polarity dependent breakdown events (shown in figure 4–7). When a positive bias is applied on the conductive tip, the AFM is able to detect the formation of a nanopore after applying a bias for 256 s. However, when the trans-membrane potential polarity is reversed, even with the same bias amplitude, pores are not formed (or are too small to be detected by AFM). We will first discuss the **band-diagrams and the charge transport** across the dielectric membrane

(illustrated in figure 4–12) and then apply the AHI model to **clarify the polarity dependence** we observe.

In our experiment, a positive bias is applied across the conductor-oxide-nitride-oxide-electrolyte (ONO) layer (band-diagrams and electron transport are shown in figure 4–12). The conductive layer (first layer from the right) corresponds to the conductive AFM tip. The two oxide layers correspond to native oxide on nitride (around 0.5 nm thick, forms when the nitride surface is in contact with air). The electrolyte layer can be considered as a conductor with an effective fermi level E_{redox} (will be discussed in details in the following subsection). When a strong electric field is applied, hot holes (such as oxygen vacancy) are created at or near the oxide-conductor interface. The holes then move towards the cathode under the influence of the external field via tunneling or Poole-Frenkel emission. Electron traps are subsequently created inside the nitride layer due to hole-trapping. In addition, defects (such as breakage of chemical bonds) are created inside the membrane by hot holes or the recombination of holes and electrons [136]. These charge traps or defects create intermediate energy states between the valance and conduction band, allowing a large fluence of electrons to pass through via electron hopping (trap assisted tunneling) and/or poole-frenkel emission and initiate dielectric breakdown.

We can apply the the AHI model to clarify the polarity dependent effects (shown in figure 4–13). When the AFM tip is positively biased, holes are induced in the oxide near the tip. The holes, under the influence of the electric field, cross the membrane to the cathode, inducing a large number of charge traps/defects in the nitride membrane along the way. The density of the traps follows the spatial distribution of hole current: much higher near the tip region and gradually decreases towards the cathode (figure 4–13 b). Breakdown occurs when a critical trap density is reached along a membrane spanning

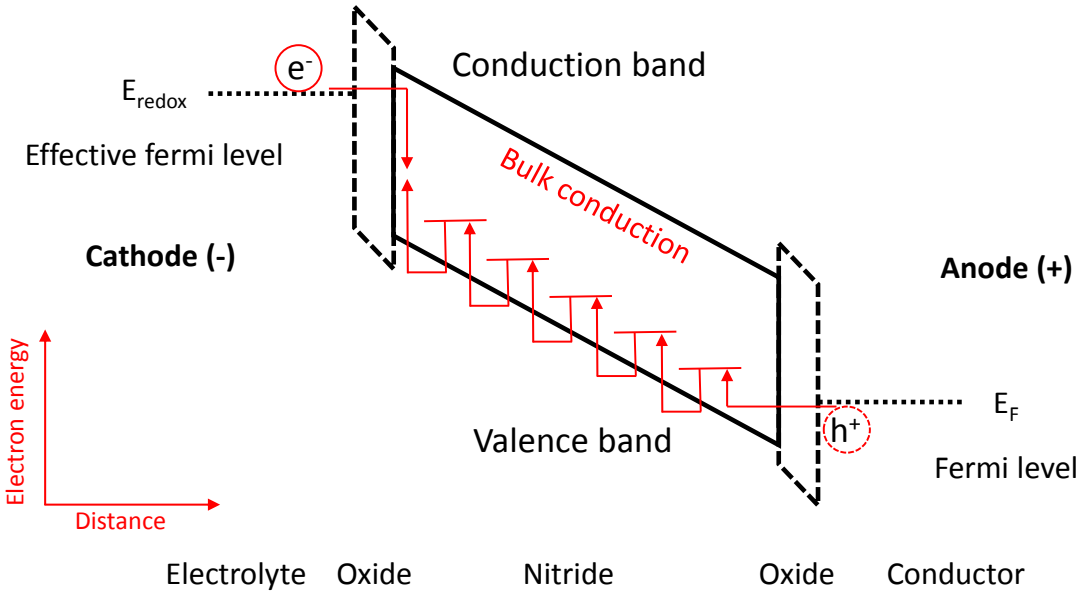

Figure 4–12: A positive bias is applied across the conductor-oxide-nitride-oxide-electrolyte layer. The anode injected hole moves across the membrane towards cathode. These induced holes create intermediate energy states in the forbidden energy band in the nitride membrane, enabling electron hopping and/or Poole-Frenkel emission, creating a path-way for high fluence electron flow, resulting in dielectric breakdown of the membrane.

path. However, in the case of reversed voltage polarity shown in figure 4–13 c, holes are randomly induced at the very wide electrolyte-dielectric interface while electrons are pulled away from the dielectric membrane. Because the electrolyte-dielectric interface is very wide compared to the localized tip-dielectric interface, holes are generated over a much wider area, and consequently, the time scale of reaching the critical trap density for breakdown in this case is much larger.

We can also use the AHI model to clarify the voltage polarity dependence of nanopore shape orientation reported in [108], without considering EDL effect. In this case, both sides of the membrane are immersed with electrolyte (figure 4–14 a). The breakdown happens at the weakest region of the dielectric membrane (thinnest region

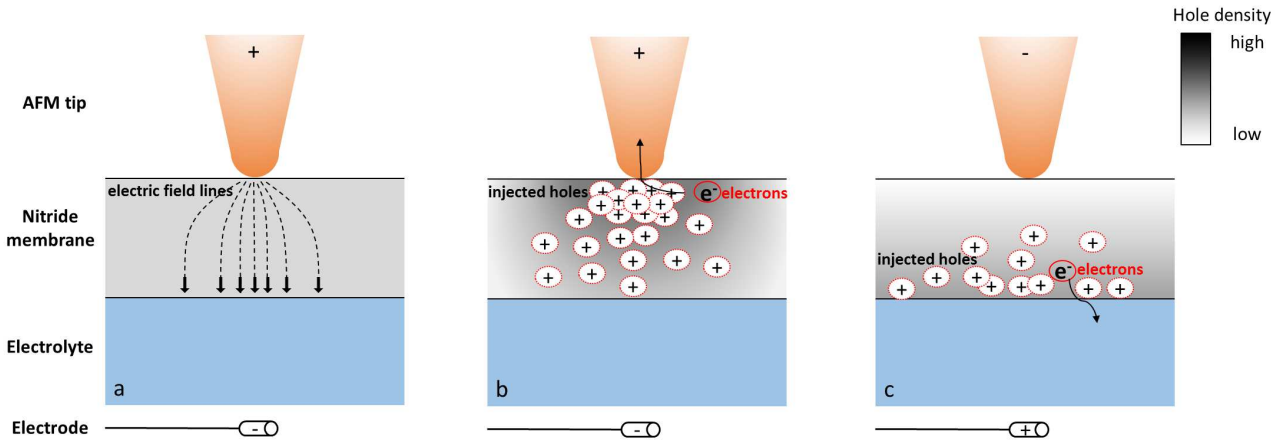

Figure 4–13: a) The electric field lines inside the nitride membrane right after applying a positive bias to the tip. b) When a positive bias is applied to the tip, electrons are drawn towards the tip inducing holes, followed by charge traps and defects, in the dielectric membrane. The hole density in the dielectric membrane depends on physical distance to the anode, increasing with increasing proximity to the anode. Breakdown happens once a critical trap density is reached across the membrane. c) In the case of reversed voltage polarity, critical trap density is much harder to reach due to the non-localized injection of holes through anode. Electrons and holes are denoted with $\ominus$ and $\oplus$.

or most defects). The density of the charge traps will be higher on the anode size due to the hole injection, thus resulting in a large opening of the cone towards the anode when breakdown happens, indicated with the red dash line in figure 4–14 a. In addition, the anode hole injection model can explain the pH asymmetry effects reported by Briggs [107] (figure 4–14 b and c). Briggs *et al* reported that nanopore formation via dielectric breakdown will be accelerated when the anode is immersed in acidic electrolyte and the cathode is immersed in alkaline electrolyte; in the opposite condition, nanopore formation will be suppressed [107]. As demonstrated in figure 4–14 b and c, the hole injection efficiency will be affected by the pH of the electrolyte. In order to inject holes inside the membrane, electrons are driven from the membrane into the electrolyte and reduction reactions occur at the electrolyte/membrane interface located on the anode

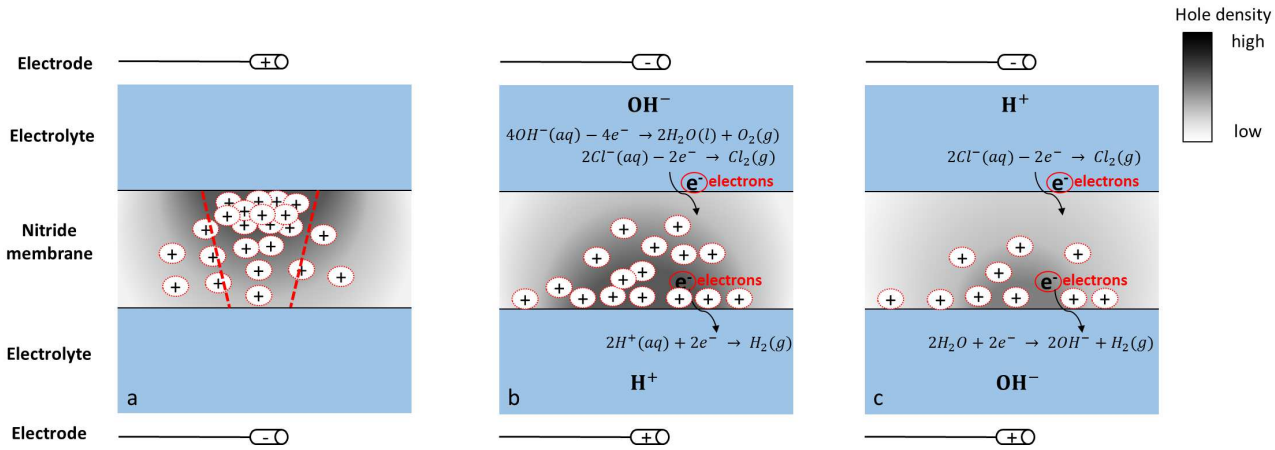

Figure 4–14: a) The injected hole density at the breakdown site (weakest region) of the membrane is higher on the anode side and lower on the cathode side, thus resulting in a larger opening towards the anode when breakdown occurs. The possible opening of the nanopore is indicated with the red dashed line, with a larger opening on the anode and a smaller opening on the cathode (agrees with [108]). b) In fast nanopore formation conditions (H^+ on anode side and OH^- on cathode side) [107], hole injection efficiency is higher when the anode side of the membrane is immersed in acidic electrolyte. c) In the slow condition (H^+ on cathode side and OH^- on anode side), hole injection efficiency is suppressed since the energy required for the reduction reaction is higher. In other words, the ability of extracting electrons from the membrane and creating anode holes in case c) is lower that b), thus resulting in a pH induced nanopore formation time difference. H^+ and OH^- sign indicate the pH of the electrolyte (H^+ lower than 7, OH^- higher than 7). Redox reactions at the electrolyte/membrane surfaces (only the electrolyte half) are listed in the figure for both conditions. Electrons and holes are denoted with $\ominus$ and $\oplus$.

side. When considering the reduction reaction in acidic electrolyte, we have:

$$H^+(aq) + e^- \rightarrow \frac{1}{2}H_2(g); E^0(V) = 0\,V \tag{4.1}$$

where $E^0(V)$ is the standard electrode potential (by definition, $E^0(V)$ is zero for reaction 4.1). However, when the anode is immersed in alkaline electrolyte, the concentration of H^+ is low and the reduction reaction is:

$$H_2O + e^- \rightarrow OH^- + \frac{1}{2}H_2(g); E^0(V) = -0.8277\,V \tag{4.2}$$

where $E^0(V)$ is -0.8277 V for reaction 4.2. The negative $E^0(V)$ means reaction 4.2 requires higher energy than 4.1, and it's easier to inject holes in the dielectric membrane when anode is immersed in an acidic electrolyte. Since a critical hole fluence is required for dielectric breakdown, the pH induced hole injection efficiency difference will eventually lead to different pore formation time (faster for figure 4–14 b, and slower for figure 4–14 c).

4.5.5 Redox Reactions and Local Anode Oxidization

One issue we haven't fully discussed is the conduction in electrolyte solution and the redox reactions occurring at the electrolyte/oxide(nitride) interface. Since electric conduction through the electrolytes takes place via ionic, not electronic, transport, redox reactions are required at the electrolyte/nitride interface to sustain the dielectric breakdown. The breakdown potential (~ 10 V) is significantly higher than the electric potential of typical redox reactions in electrolyte (1.23 V for water electrolysis). We believe the fundamental breakdown mechanism of the nitride film should not be affected by the presence of electrolyte (even though the hole injection efficiency can be affected by the electrolyte), To simplify the model, we considering the electrolyte as a conductor with an effective fermi level.

Another effect closely related to the AFM nanopore is the local anodic oxidization. Local anodic oxidization occurs when a negative voltage pulse is applied across the AFM tip and the substrate (tip is cathode, and the substrate is anode). A water

meniscus is formed between the tip and substrate surface. This nanometer-sized water meniscus acts like an electrochemical cell. Oxyanions (OH^-, O^{2-}) are driven towards the anode and oxidize the substrate surface. Typically, this technique is used to locally oxidize silicon and metallic substrate, creating nanoscale patterns such as nanowires [137] and Cervantes' Don Quixote [138]. In our AFM setup, local anodic oxidization can also contribute to the polarity asymmetric effect since local anodic oxidization will always appear on the anode side. However, local anodic oxidization is not likely a driving process for pore formation, since local anodic oxidization creates nano-sized oxide peaks instead of holes [139]. Control experiments could potentially be performed under vacuum condition to rule out the effect of local anodic oxidization.

4.6 Discussion and Future Applications

To conclude we have developed a new method of fabricating nanopore on thin silicon nitride membrane via AFM dielectric breakdown technique. With this technique we were able to produce arrays of nanopores by simply varying the position the AFM tip. We also presented a detailed study of AFM processing conditions that permit pores to form and the resulting pore size.

We developed a new theory, 'the anode hole injection model,' to explain pore fabrication via dielectric breakdown. We believe anode hole injection provides a fundamental and comprehensive explanation for breakdown-based pore fabrication, providing a physical origin of charge trapping and explaining the bias polarity asymmetries observed in both our AFM breakdown approach and classic breakdown-based pore fabrication.

Finally, we have demonstrated that the AFM breakdown approach is an effective technique for forming single nanopores or nanopore arrays, which could be efficiently

applied at low cost in industry. While we have demonstrated pore fabrication in experiments where only one side of the membrane is dry, we believe pores could be created in completely dry conditions (i.e. both sides of membrane dry, see figure 4–15). We argue that a conductive-AFM could be used as a local electrode on one side of a nitride coated silicon wafer, while applying a breakdown voltage between the tip and the silicon wafer (with the silicon wafer doped to ensure sufficient conduction). After photo-lithography, RIE and KOH etching to remove the bulk silicon beneath the pores, we would form a potentially wafer scale nanopore/nanopore array.

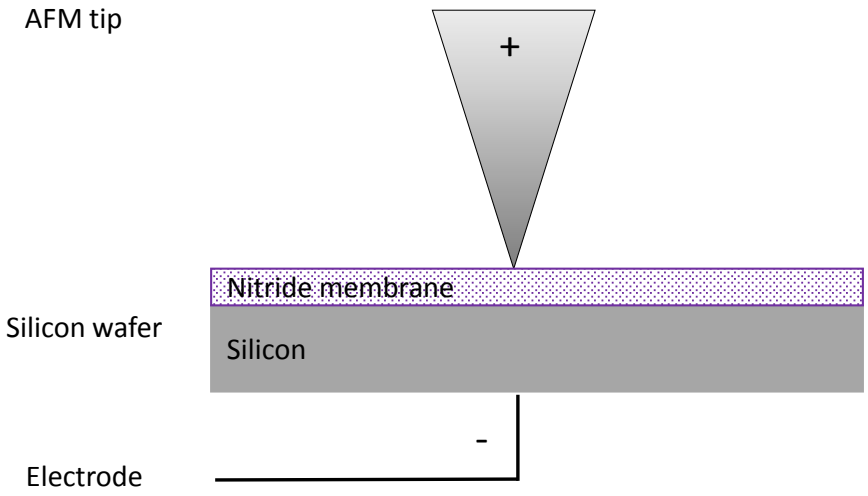

Figure 4–15: A schematic showing proposed nanopore fabrication via completely dry AFM assisted dielectric breakdown.

CHAPTER 5
Graphene-enabled Electron Microscopy: Part One
– Graphene Liquid Cell for Scanning Electron Microscopy

chapter 5 presents the fabrication and characterization of a novel liquid cell for SEM imaging using single layer graphene membrane as imaging window. Gold nanoparticle dynamics in liquid environment are successfully recorded and analyzed using the graphene SEM liquid cell.

This chapter is the integral text from:

Dynamic Imaging of Au-nanoparticles via Scanning Electron Microscopy in a Graphene Wet Cell

Wayne Yang[†], Yuning Zhang[†], Michael Hilke, and Walter Reisner, Nanotechnology 26, no. 31 (2015): 315703. ([†] equal contribution) [140]

5.1 Introduction

Nanoscale imaging in liquid environments is important across a wide range of research fields from physics to biology, driving new insights in molecular and biological theory [141, 142]. New experiments enabled by wet-cell technology include live imaging of antibodies and bacteria to understand immune response and in-situ imaging of crystal growth to deduce growth kinetics [143]. The imaging is typically performed with

electron microscopy such as SEM (Scanning Electron Microscope) or TEM (Transmission Electron Microscope) [144, 145]. In particular, SEMs are widely available and accessible to most researchers. While SEMs offer quick and high resolution nanoscale (2-10 nm) imaging, the high vacuum operation conditions ($<10^{-4}$ Torr) of these instruments make the imaging of liquid environments challenging [146]. Systems that operate at high pressures such as environmental SEMs (E-SEMs) are specialised tools requiring the use of water vapour to purge and replace air in the specimen chamber. Moreover, the electron beam in such systems scatters from the introduced vapour resulting in limited resolution [147, 148, 149].

Conventional wet cells are based on sealing liquid samples behind a 30-150 nm silicon nitride window [150, 151]. While this approach has proved effective, the resolution is fundamentally limited by the necessity of using relatively thick nitride membranes. Experiments have obtained a resolution of only around 20 nm for a membrane thickness of 50 nm in an SEM [152]. The fabrication of thinner nitride windows with thickness below 50 nm is challenging, requiring special techniques to control the etching rate and achieve etching uniformity [153]. As the nitride membrane becomes thinner, the windows become too fragile to handle. Silicon nitride wafers are also electrically insulating, requiring the sputtering of a thin layer of conductive material such as gold for electrical leads or to ground the sample [154]. Ultimately, nitride based windows cannot be extended to thicknesses below a few nanometres. This is a very crucial technical limitation, limiting not just resolution but signal. For example, the need for relatively thick nitride windows obviates application of standard SEM techniques such as Energy Dispersive X-Ray (EDX) due to the absorption of signal by the thick membrane.

Here we present a graphene wet cell for SEM imaging under a high vacuum environment. Graphene is an atomically thick layer of carbon atoms (0.34 nm thickness) [155]

with exceptional properties including high mechanical strength, high thermal and high electrical conductivity. Graphene's atomic thickness makes the material an optimal imaging window enabling maximum resolution and signal. In particular, graphene allows for the collection of low energy secondary electrons as opposed to just colllecing backscattered electrons in most SiN wet cell imaging studies [156], greatly improving the signal and resolution. Graphene's mechanical strength prevents breakage of $\sim 5\,\mu$m membranes under vaccum conditions. Graphene's high thermal conductivity allows excess heat generated from the beam to dissipate quickly without damaging the sample. Finally, graphene's high electrical conductivity obviates the need for an additional metal coating for grounding. The graphene membrane also provides convenient electrical leads for voltage and current inputs for adding electrical bias in experiments. Previous groups have used graphene oxide membranes for imaging [157]. However it is challenging to control the homogeneity in the graphene oxide membrane across the window and, at around 20 nm thick, they are comparable in thickness to nitride. Using chemical vapour deposition (CVD) with carefully controlled growth conditions we can ensure that there is a single layer graphene membrane [158, 159].

Our single-layer graphene wet cell device enables dynamic imaging in a SEM. In particular, we observe Brownian dynamics of Au-NP's transiently binding and unbinding at the surface of the graphene. While Brownian motion of Au-NP's has been observed previously in a TEM using a graphene sandwich assay, developing a molecular in-liqiuid imaging capability in an SEM has key practical and fundamental benefits [7]. SEM's are more available, cheaper and more versatile tools that permit introduction of much larger samples. For example, large (1-10 cm size) micro/nano fluidic devices could be easily introduced into an SEM and wet cell imaging could then be performed

as part of routine device operation. In particular, as there is no constraint on sample thickness in an SEM, an SEM-based wet cell can incorporate much deeper fluidic channels without loss of signal, significantly simplifying wet-cell design. Moreover, additional sample material can be potentially pulled in from deeper in the cell. For example, we show that continuous scanning attracts Au-NP's to the graphene interface. Finally, SEMs are outfitted with a wide range of surface characterisation tools (for example, EDX). We show that, using our graphene wet cell device, these tools can then be adapted to study the wet cell environment. As an example, we able to obtain an EDX spectrum of Au NPs in liquid.

5.2 Sample preparation

Our fabrication process is divided into three steps, the fabrication of the silicon nitride substrate, the growth and transfer of the graphene and the wetting and sealing of the device for SEM imaging. An illustration of the device is shown in figure 5–1.

The first step is substrate fabrication. Our substrate is a $400\,\mu m$ thick (110) silicon wafer coated with a 180 nm thick nitride membrane and divided into 2×2 mm dies. The wafer was patterned with photolithography and etched in KOH from the back to produce a $70\times70\,\mu$m residual nitride membrane in the middle of each die. The KOH etched apertaure also serves as a reservoir for the liquid sample. Lastly, a $2\,\mu$m diameter hole was etched through the middle of the free standing nitride membrane to form the graphene viewing window.

Graphene was grown using Chemical Vapour Deposition (CVD) on a $25\,\mu m$ thick copper foil with a growth temperature of $1050\,^o$ C at a pressure of 100 mTorr and a flow of 4 sccm of CH_4 [160]. Our custom-built CVD system is based on a vertical furnace. Two gas tubes feeds into the top of a 2.5 cm wide vertical quartz tube to provide the flow of gases. The quartz tube is lowered into the oven during the growth and

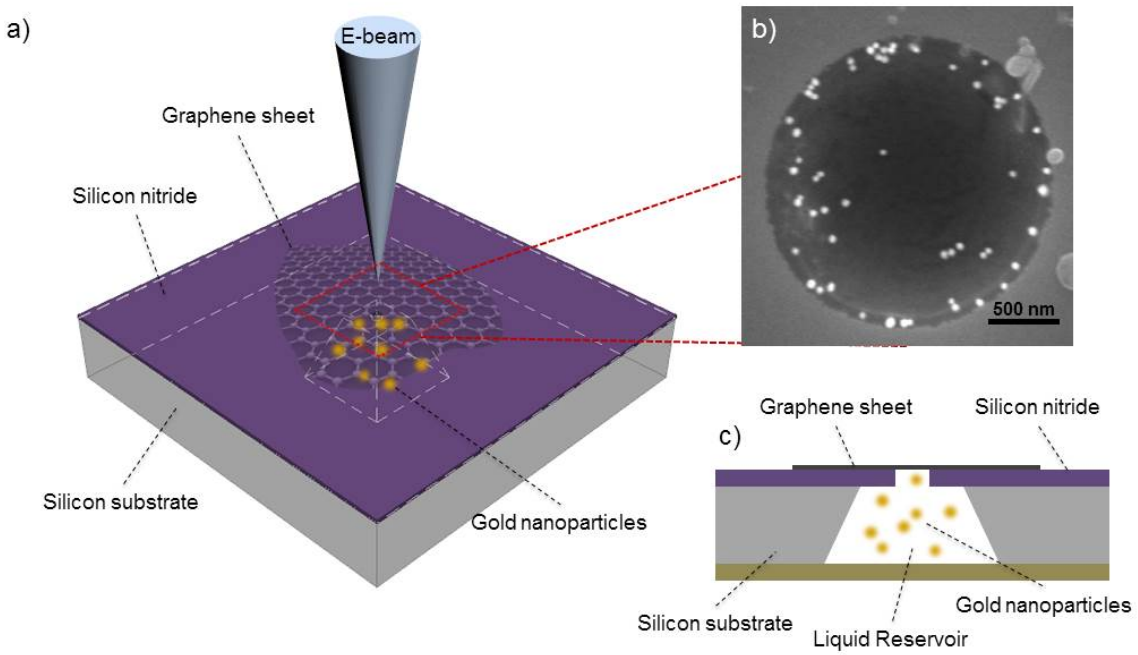

Figure 5–1: a) A schematic of our graphene wet cell device. b) SEM image of the liquid environment imaged through the graphene membrane micropore. The graphene is positioned on top of a circular aperture etched through the SiN membrane. c) Schematic of device as viewed from the side. The liquid sample, held in the 400 μm fluid reservoir sandwiched between the graphene membrane and kapton tape, consists of deionized water with Au nano particles. The figure is not drawn to scale.

the growth time is approximately 1 hour. Before the growth, the copper foil was first annealed in a flow of 12 sccm of hydrogen for an hour to strip the oxide layer on the foil. The CVD synthesized graphene was then spin coated with a thin supporting layer of polymethylmethacrylate (PMMA) layer and the Cu substrate was etched away in a solution of 0.1 M ammonium persulfate ($(NH_4)_2S_2O_8$). The sample was transferred by inserting a glass slide into the ammonium persulfate solution, using the slide to scoop out out the freely floating graphene membrane and depositing the graphene

bearing slide into a beaker of de-ionised water. To completely remove the ammonium persulfate residues, the sample was transferred into another clean beaker of de-ionised water before being transferred onto the top side of the silicon nitride wafer sample to cover the 2 μm holes. Graphene produced using the same growth conditions was transferred onto $Si0_2$ wafers for Raman spectroscopy to confirm that the graphene was indeed monolayer.

Finally, the sample was ready to be wetted and sealed. Gold nanoparticles (Au-NP's) 20 and 50 nm in diameter were used to characterise the fluid cell. We chose Au particles as they are commercially available in a wide variety of sizes and can potentially be used as conductive biological labels [161]. The Au-NP's were diluted 1:20 from stock solution in DI and then the nanoparticle containing solution was degassed for an hour. Degassing was crucial to ensure proper wetting and to decrease the formation of gas bubbles during imaging. After degassing, several microliters of solution was pipetted into the reservoirs and the wafer sample was sealed with Kapton tape on the back side. The device was then rinsed in acetone and isopropanol to dissolve the PMMA supporting layer on the graphene. The imaging of the device was then done using a FEI-F-50 SEM in the standard high vacuum mode at 10^{-6} Torr using a secondary electron detector of the Everhart-Thornley type. The graphene membrane remained intact at this operating pressure of 2.2×10^{-6} Torr. The primary electron energy used for imaging is 10 KeV. Under these imaging conditions, the escape depth of secondary electrons in water should be in the order of 10 s of nm [162].

5.3 Observation of Nanoparticle Dynamics

While many Au-NPs are non-specifically bound to the membrane, we observe Brownian dynamics of Au-NPs floating in solution below and undergoing transient interactions with the membrane. These dynamics are recorded over several minutes

using a screen capture program. Figure 5–2 gives an example of bead motion. Beads are observed to be diffusing in and out of contact with the membrane surface, confirming that they are indeed contained in a liquid environment. The particle trajectories are recorded using a custom tracking program [151].

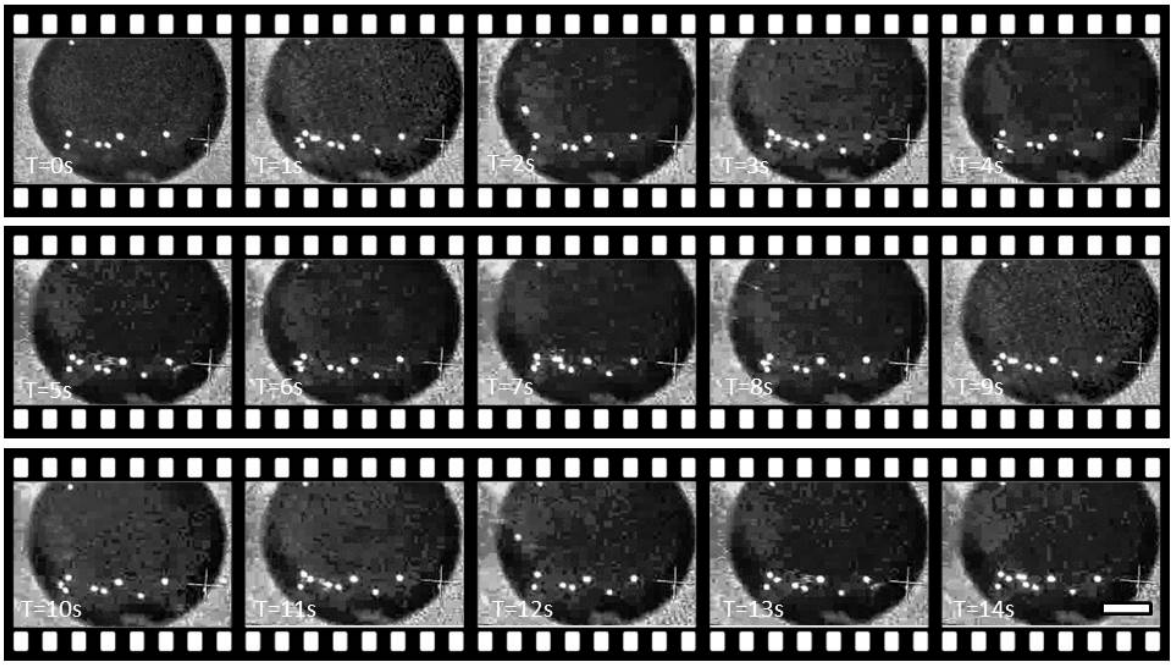

Figure 5–2: Image time-series showing Au-NP dynamics in our graphene wet-cell device. Beads are observed to be diffusing in and out of contact of the graphene nanopore. The white bar indicates 500 nm.

In the absence of confinement, the gold nanoparticles are expected to undergo Brownian motion in water, characterized by a diffusion constant :

$$D = \frac{k_b T}{6\pi\eta r} \tag{5.1}$$

where k_b is the Boltzmann 's constant, T is the temperature (300 K), η is the viscosity of DI water (1×10^{-3} Pa·S), r is the radius of the beads (25 nm). For our image frame rate of $1/t_s$=29 Hz, this leads to a corresponding mean diffusion length of

$L_D = \sqrt{Dt_s} \simeq 550\,\text{nm}$ at room temperature (300 K). Hence, within one image frame the particles are expected to approximately hop 1/4 of the length of the nanopore. Figure 5–2 suggests that we indeed see fluctuations on that scale. However we also observe two additional types of behaviours. Particles can be permanently bound to the membrane over the course of the imaging time and can also diffuse in and out of contact with the membrane, interacting transiently with what appears to be "sticky sites". This sticking behaviour can be quantified by a plot of occupation probability $p(x, y)$. The occupation probability is taken by integrating the total number of frames a bead appears at a certain location normalised over the total number of frames of the video. Figure 5–3 shows the occupation probability for the same device with a spatial resolution of 10 nm and time resolution of 25 ms, clearly indicating the existence of strong trapping sites that permanently bind beads and weaker trapping sites that give rise to transient interactions.

The non-uniformity of the occupation probability suggests that the graphene membrane varies with regards to its physical and chemical reactivity towards nanoparticles. One possible source of non-unformity are the existence of grain-boundaries in the graphene layer [163]. These grain boundaries are imperfections in the graphene lattice due to differently orientated growth directions. The grain boundaries from previous studies are spaced roughly the same distance apart ($\sim 1\mu$m) as the observed sticky sites. Another possible source of non-uniformity is the presence of graphene "wrinkles" arising from the growth conditions on the inhomogeneous surface of the copper foils [158]. The wrinkles form valleys in the graphene sheet allowing beads to be drawn in through attraction by van der Waals forces (which has also been observed in other wet cell applications)[164]. To reduce this effect, we repeated the experiment with PEG (polyethylene glycol) coated Au beads as shown in Figure 5–4. Indeed we observed a

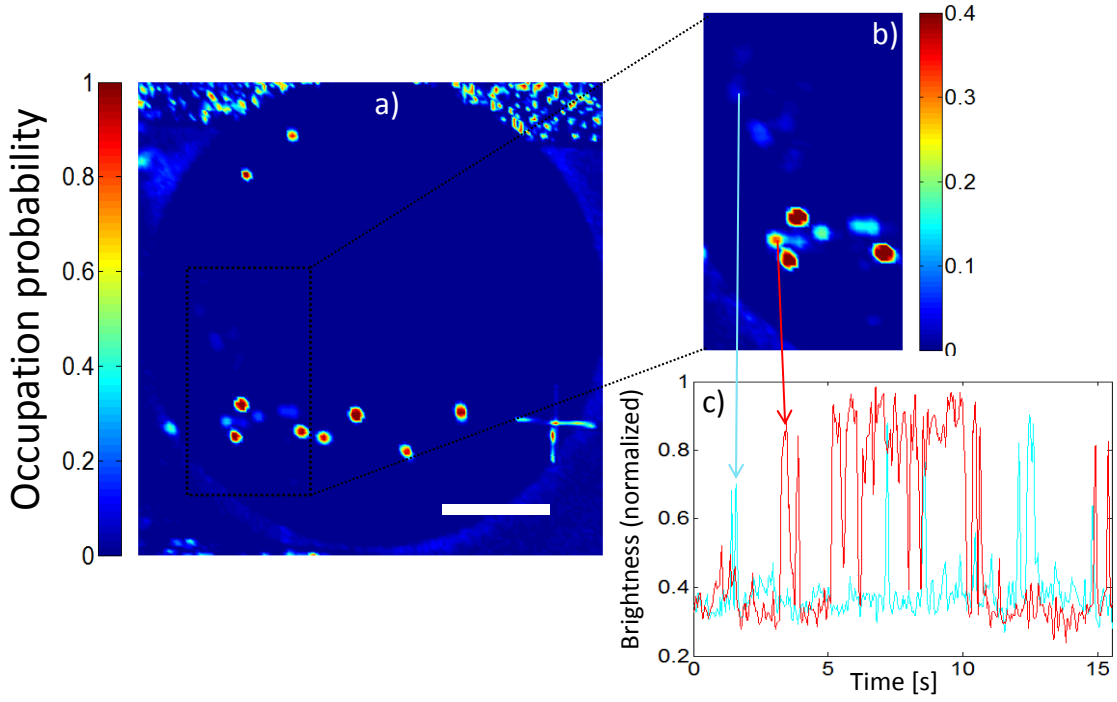

Figure 5–3: a) Plot of the integrated (over 15 s) normalized nanoparticle occupation probability across the graphene membrane. The nanoparticle occupation is defined as a brightness of 70 % or more. Some spots show an occupation of unity, meaning that beads are bound to the membrane at these positions for the entire duration of the movie. b) Zoomed image of the upper left corner with arrows indicating the positions of the time traces in (c). Each pixel shown corresponds to an integrated area of $30\times30\,\mathrm{nm}^2$ at a frame rate of 29 Hz. The scale bar denotes 500 nm in length.

suppression of the adhesion of Au particles to the graphene membrane with a reduction of the density of stuck beads upon imaging [165].

Our dynamic SEM imaging capability, performed over a deep sample reservoir, enables us to demonstrate that continuous scanning draws beads to a scanned region of the membrane. We selected two areas ($0.7\times0.2\,\mu$m) on the graphene membrane,

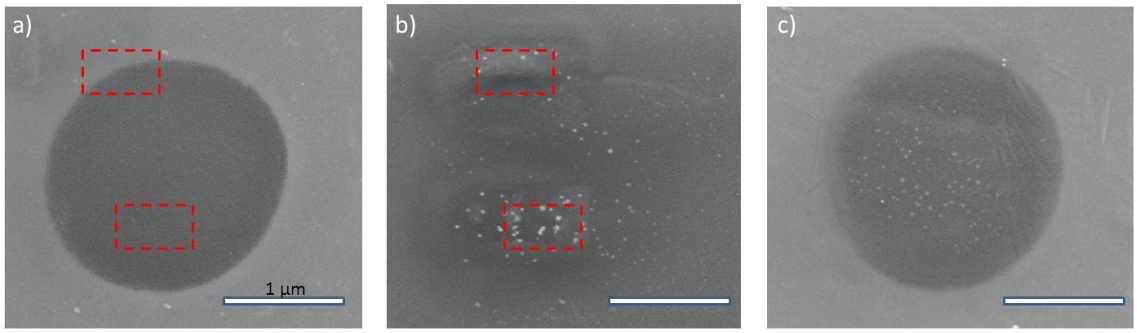

Figure 5–4: a) The graphene pore before imaging in SE mode. The red boxes indicate the areas selected to be scanned for 2 minutes. b) The image of the pore after scanning. c) Image of a graphene membrane on a different device that has been repeatedly scanned by the electron beam. Note that the beads are drawn to the surface. The white scale bar indicates 1 μm.

marked by the dashed red boxes in Figure 5–4 a). The area was then scanned continuously at 5 KeV for 2 minutes. Beads were observed to diffuse onto the graphene membrane in those areas (Figure 5–4 b). Note that Figure 5–4 b) is exactly at the same spot as Figure5–4 a). The image looks different because the graphene membrane was observed to be deforming from the continuous scans. In Figure 5–4 c), we scanned the entire pore on a different device for several minutes to draw beads onto the graphene membrane. This dynamic beam-induced attraction of the beads might arise from electrostatic charging of the membrane, possibly related to chemical modification of local impurities such as PMMA residues (resulting in charge trapping) [166]. In addition, the PMMA from the supporting layer in the transfer process may not be totally removed during acetone-based dissolution process. Finally, space charge transiently deposited in a nanoscale region beneath the graphene by either electron depositon or secondary electron generation might induce polarization forces on the beads [167]. The stability of the graphene membranes greatly varies due to these effects. We observed cells that

were stable for 2-15 minutes under 10 KeV. Future cells can be improved by optimizing the imaging conditions and reducing contamination of the graphene membrane.

5.4 Energy Dispersive X-ray Spectroscopy

The use of EDX in a wet cell could potentially allow for positive chemical identification of elements in a liquid environment. EDX, however, cannot be performed in a standard silicon nitride wet cells due to the thickness of the nitride layer that absorbs emitted radiation. Here we show that graphene membranes enable EDX-based analysis in liquid enviornments.

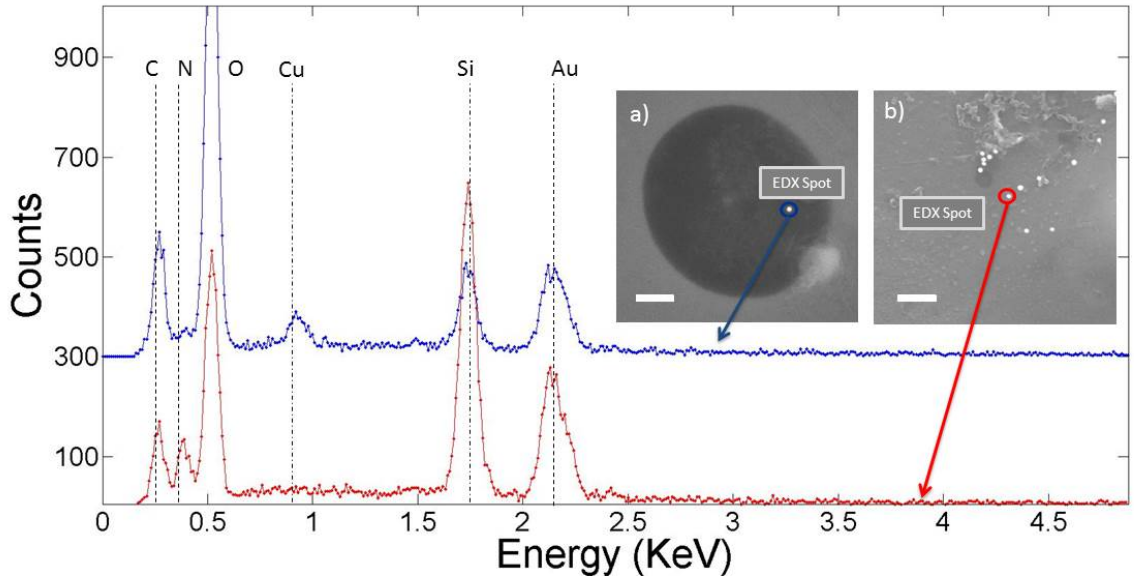

Figure 5–5: EDX spectra for a bead underneath the membrane (blue line) and at a control location away form the membrane and on top of the nitride film (red line). Both spectra were integrated over 30 s and the bead-in-liquid spectrum is offset by 300 counts for ease of comparison. Inset a) Secondary electron image of location of bead-in-liquid. Inset b) Secondary electron image of control bead. Both scale bars indicate 500 nm.

We attracted diffusing Au NP's with the electron beam to the surface of the graphene membrane and performed EDX. Figure 5–5 shows spectrums taken at two different locations. The first EDX location (Figure 5–5 a)) is for a graphene bead

located underneath the membrane layer. The second location (Figure 5–5 b)) is for a Au-NP resting on top of the graphene-silicon nitride wafer away from the membrane. To ensure that the EDX spectra correspond to beads in liquid and not on the surface of the membrane, we performed EDX only on beads that had freely diffused onto the surface of the graphene membrane during imaging and were stuck there during the EDX. Remarkably, we only see a 30 % reduction in the integrated intensity for the Au signal under the graphene vis-a-vis the control spectrum. The source of the attenuation may be due to absorption of the signal by surrounding water or contamination deposited by the electron beam during the EDX measurement. Despite the attenuation, we are still able to positively identify the in-liquid particle composition. We also observe a much lower but non-zero silicon peak coming from location (a). The peak arises from the silicon background scattering from the hole edges. In addition, we observe a weak copper peak on the suspended graphene membrane, likely arising from copper used in the growth process that is not completely removed. We were able to perform multiple EDX measurements without any degradation of the graphene membrane.

5.5 Resolution

To determine the resolution of the Au-NP's under the graphene wet cell we imaged 20 nm beads bound to the membrane. The intensity line profile of each Au-NP (see Figure 5–6) was extracted and the resolution was determined from the edge-width over which the Au-NP's intensity rose from 20 % to 80 % of its maximum height [77]. Averaging over five beads, we find the resolution of the Au-NP's in our wet-cell to be 5 ± 3 nm (error is standard deviation on mean over beads measured).

The contrast to noise ratio (CNR) is defined as :

$$CNR = \frac{S}{\sigma_n} \tag{5.2}$$

where S is the peak signal and σ_n is the standard deviation of the background noise [168]. We obtained a value of 7 ± 1. These results confirm that graphene leads to improved resolution: our resolution is higher than the 20 nm reported in the 50 nm silicon nitride membrane and comparable to the resolution ($\sim$ 5 nm) obtained under much higher electron imaging conditions such as at 200 Kev in a TEM [77]. The high contrast to noise (CNR) ratio also makes it possible for us to observe and record movements in the liquid environment.

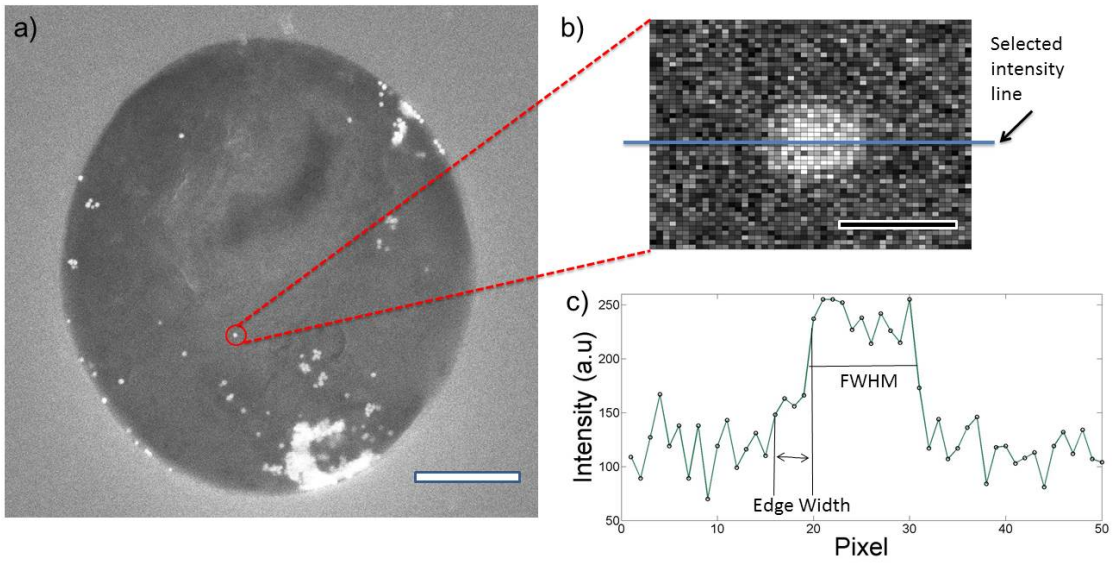

Figure 5–6: a) A secondary electron image of 20 nm Au particle non-specifically absorbed to the graphene window. b) A close-up image of a bead selected as an example. c) Intensity line profile. The edge width is determined from the 20-80% rise in intensity at the profile edge. A resolution of 5 ± 3 nm with a CNR of 7 ± 1 is obtained from averaging results over five beads. The white and black scale bars in a) and b) corespond to 500 nm and 25 nm respectively.

5.6 Conclusion

In conclusion, we have demonstrated that single layer CVD grown graphene is very promising for SEM based wet cell imaging, enabling dynamic imaging of Au-NP

undergoing brownian motion in aqueous solution and EDX measurements in liquid. In particular, our wet cell can be used in a conventional SEM without the need for instrument modification. In the future, opposed to previous graphene sandwitch studies, our wet-cell can be in principle adapted for nanofluidic experiments with nanochannels etched in place of the fluid reservoirs. Such systems might enable nanoconfinement based single molecule manipulation combined with SEM imaging, giving rise to new types of single-molecule analytical devices based on electronic as opposed to optical imaging. Our EDX results are particularly significant in this context: one can envision future experiments that use biomarkers with differential chemical composition to tag a range of DNA modifications enabling more efficient multiplexing.

CHAPTER 6
Graphene-Enabled Electron Microscopy: Part Two
– Graphene Liquid Cell for in *situ* Transmission Electron Microscopy

chapter 6 presents the fabrication and characterization of a novel liquid cell for TEM imaging using single layer graphene membrane as imaging window. Gold nanoparticle dynamics in liquid environment are successfully recorded and analyzed using the graphene TEM liquid cell.

Dynamic Imaging of DNA-Gold Conjugates via Transmission Electron Microscopy in a Micron Scale Graphene Liquid Cell

Yuning Zhang, Martin Lee, Carlos Ruiz-Vargas, Wayne Yang, Robert Sladek, Michael Hilke and Walter Reisner.

6.1 Abstract

We developed a novel graphene liquid cell for the study of nanoparticles and DNA molecules with in *situ* transmission electron microscopy (TEM). We demonstrate that with the mechanical support of pre-patterned TEM nitride windows, the graphene cell is able to provide a true micron-scale viewing window. With this technique we have observed dramatically different gold nanoparticles diffusive motions with a broad range distribution of the particle diffusion coefficients ranging from 1 to $100\,nm^2/s$ (differed by an order of 2). In order to explain this phenomena, we proposed a sandwich model

to describe the liquid layers in the cell. In addition, we also explored different DNA labeling techniques for electron microscopy.

6.2 Introduction

Nanoscale imaging in a liquid enviornment is crucial for a wide range of fields. The direct imaging of liquid-phase processes at the nanoscale has helped reveal fundamental biological activity in cells [77, 8], understand the growth kinetics of crystals [6, 143], and the study of biomineralization [169]. Conventional techniques, such as super resolution microscopy and cyro-electron microscopy (cryo-EM) are able to image specimens in liquid with nanometer resolution. However these methods are subject to obvious disadvantages: super resolution microscopy has limited resolution when compared with EM techniques and cryo-EM are not capable of recording specimen dynamics due to the flash-frozen process.

Given the disadvantages of conventional techniques, an alternative technique, termed as the in *situ* TEM technique, is proposed for improved imaging of samples in a hydrated environment. The in *situ* TEM technique images specimen through an artificial liquid cell constructed by sandwiching a thin layer of specimen containing liquid (10 nm – 200 nm) between a double stacked amorphous membranes [79]. The typical liquid cell schematic is shown in figure 6–1 a. The two amorphous window membranes are typically made of silicon nitride with a spacing ranging from tens to hundreds of nanometers. While the nitride membrane liquid cell has been successful in a broad range of applications including the direct observation of biological structures and real time dynamics of nanomaterials [77, 75], the resolution achieveable with a silicon nitride liquid cell is limited to a few nanometers due to the scattering of electrons by the relatively thick amorphous layer [2]. In addition, the TEM imaging can be degraded

by accumulated charge and excessive heat resulting from the relatively low electrical and thermal conductivity of silicon nitride.

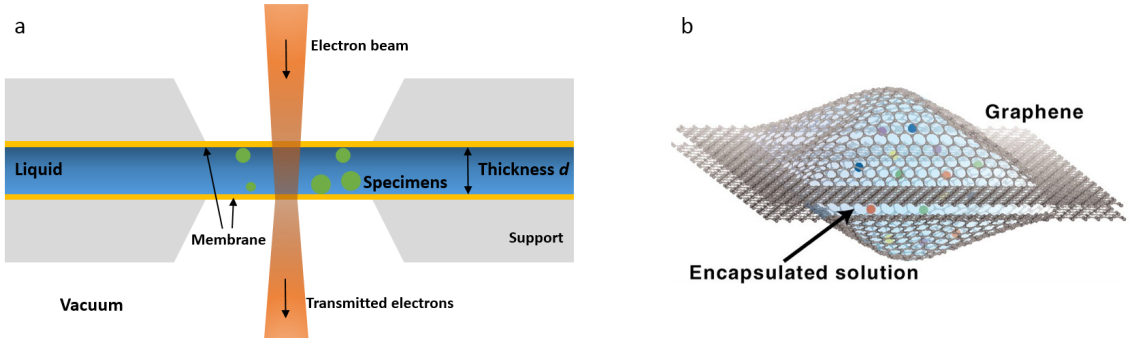

Figure 6–1: Liquid cell designs for TEM. (a) Conventional liquid cell design. Specimen containing liquid is sandwiched between two thin membranes (10–100 nm thick, typically made of silicon nitride supported by silicon). The thickness of the liquid layer (d) is controlled by the spacing of the membranes, ranging from tens to hundreds of nanometers. (b) Graphene based liquid cell design. Specimen containing liquid is encapsulated between two single layers of CVD graphene. The size of the graphene liquid cell typically ranges from several to hundreds of nanometers. Figure b is adapted from [6].

Recently, the Alivisatos group presented an alternative design: by replacing the silicon nitride membrane with single layer graphene, they were able to encapsulate Pt gorwth solution and observe colloidal platinum nanocrystal growth in a graphene liquid cell with atomic-level resolution [6], (see figure 6–1 b). The graphene liquid cell is straightforward to make as graphene membranes are highly flexible, with outstanding mechanical tensile strength and impermeable to small molecules [20, 21], making them ideal for encapsulating gas, liquid and soft materials either for ambient or high vacuum condition experiment. In addition, graphene is reported to have excellent electrical conductivity that helps discharge the surface and reduce free electrons in the liquid cell leading to less electron radiolysis damage to the specimen [22]. High thermal conductivity of graphene (5300 $\mathrm{W{\cdot}m^{-1}{\cdot}K^{-1}}$ [23]) will also help minimize heating effects

(e.g. liquid overheating, bubble generation) under electron beam imaging. However, due to the fundamental limitation of the graphene liquid cell design, the cell size is limited to the order of 10 – 100 nm. Once the cell is extended to micron size, the free standing CVD grown graphene, containing multiple domains, can be easily broken due to the weakness introduced by grain boundaries.

Here we report the development of a nitride/graphene hybrid liquid cell for TEM combining the outstanding mechanical stability of nitride cell with the atomic-level resolution of graphene. The new liquid cell is assembled by sandwiching two identical silicon nitride windows containing micropore arrays covered by single layer CVD graphene (see figure 6–4). With the new liquid cell, we were able to image and record both free and DNA-conjugated gold nanoparticles' dynamics. We observe dramatically different nanoparticle diffusive motions with diffusion coefficients ranging from 1 to 100 nm^2/s. We propose a possible "sandwich" model to understand the variation in particle diffusion constants we observe.

6.3 Sample Preparation

6.3.1 DNA Labeling for Electron Microscopy

In this section, I will introduce two labeling methods used for our experiments and also present the labeling results.

Heavy Atom Labeling

Bio-molecules, such as protein and DNA, are usually constructed from light elements (C,O,H,P and S, with low atomic number Z) that cannot be imaged with atomic level resolution in a TEM. To overcome this problem, DNA can be tagged with heavy elements. Typical labeling chemistries includes bromine (Br, Z=35), iodine (Ir, Z=53), osmium (Os, Z=76), iridium (Ir, Z=77) and uranium (U, Z=92). Uranium, usually in the form of uranyl acetate, $UO_2(CH_3COO)2{\cdot}2H_2O$), is the most widely used stain

for electron microscopy. Due to its high atomic weight, uranium can produce high electronic density and image contrast as well as to imparting a fine grain to the image [170]. The binding mechanism is principally electrostatic. Positively charged uranyl ions binds to the negatively charged phosphate backbone of DNA (figure 6–2 a). The heavy atom labeling technique is also termed "negative staining", because we see not the specimen itself, but rather an area empty of stain surrounded by stain.

We successfully labeled our DNA molecules (Hind3 digested λ-DNA from New England BioLabs Inc.) with 2 wt% uranyl acetate for dry specimen TEM imaging. The detailed labeling protocol is as follows:

Immobilization of biological sample. We first immobilize DNA molecules on an amorphous carbon-EM grid in order to produce a stable image. The amorphous carbon film typically has a membrane thickness ranging from 5 to 100 nm. The carbon film is mechanically robust, so it can support bio-molecules on surface, and sufficiently thin to provide contrast for imaging. We pipetted 5 μL Hind3 digested λ-DNA (10 μg/mL) onto a 50 nm thick carbon grid, waited for 1 minute and then washed the carbon grid three times gently with DI water in order to remove free DNA molecules.

Uranyl acetate surface staining. Prior to staining, we filtered the 2 wt% uranyl acetate with Whatman grade 1 filter to remove precipitated salt particles. We then pipetted 5 μL of uranyl acetate solution on to the grid and incubated for 1 minute. We washed the stained DNA with DI water for 3 times to remove excessive uranyl ions and precipitated salt.

Imaging. We imaged the stained DNA with a FEI Tecnal G2 F20 200 kV Cryo-STEM (TEM mode) at FEMR (Facility for Electron Microscopy Research, McGill University). The labeled DNA molecules are shown in figure 6–2 b-d (dark lines). DNA molecules shown in figure 6–2 have a total length of $\sim 1.4\,\mu$m and $\sim 2.3\,\mu$m. It is not

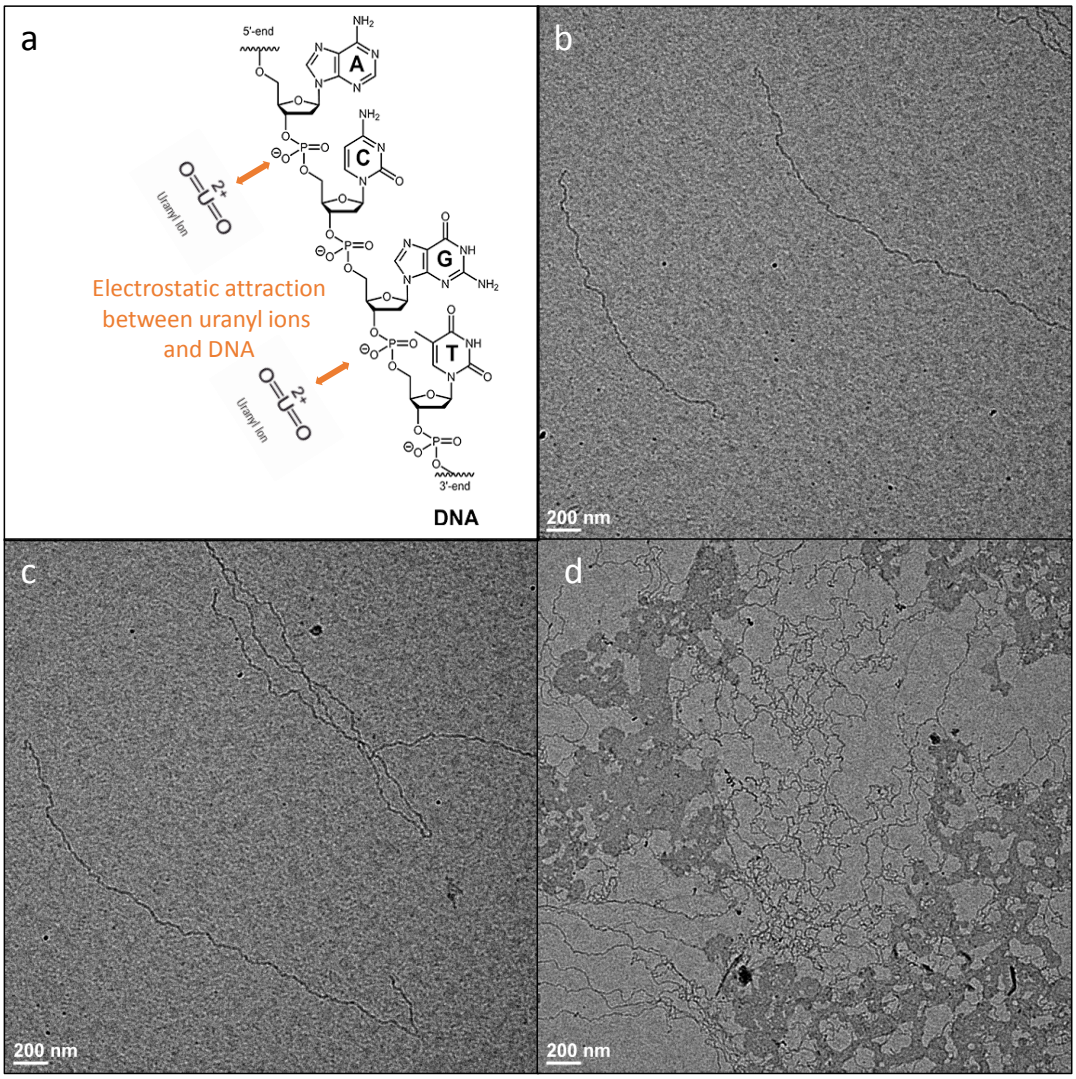

Figure 6–2: Uranyl acetate DNA labeling. (a) Schematic showing Uranyl ions binding to the negatively charged phosphate backbone of DNA. (b)&(c) TEM images of Uranyl acetate labeled Hind3 digested λ-DNA molecules. (d) Lower magnification TEM image showing multiple DNA molecules entangled by Uranyl acetate salt residuals.

surprising that the stained DNA molecules we observe have different lengths, since Hind3 digested λ-DNA has a length (fully extended) distribution ranging from 43 nm

to 7.9 μm. Figure 6–2 d shows a cluster of DNA molecules together with the uranyl acetate contamination.

The uranyl acetate labeling technique is straightforward, fast and inexpensive, however this technique only works on surface mounted and dry specimens. We tried sandwiching uranyl acetate labeled DNA solution in our newly developed ~ 100 nm thick liquid cell and imaged with TEM, but without success. This is possibly due to the excessive uranyl ions in the bulk solution. Imaging electrons are heavily scattered when transmitting through the solution resulting in a poor resolution and contrast, not enough to resolve individual DNA molecules.

Cationic Gold Nanoparticle Labeling

Instead of labeling DNA molecules with heavy atoms, Warner *et al* presented a straightforward technique of labeling DNA molecules with cationic gold nanoparticles [171]. Nanometer-sized cationic gold particles can be used to label double stranded DNA molecule, revealing the contour of a DNA molecule. In addition, by adjusting the particle-DNA incubation time [171], the cationic gold particles can be used to build complex structures such as ribbons and branches. The gold nanoparticles bind to the negatively charged DNA phosphate backbone and are spaced evenly along the chain due to electrostatic repulsion. The resolution of this technique is limited by the size of the cationic gold nanoparticle. Smaller particles will result in denser labeling (smaller average particle to particle distance).

Cationic gold nanoparticles used in our experiments are commercially available from TED PELLA (synthesized by British Biocell International solutions). The cationic gold nanoparticle have an average diameter of ~ 10 nm and a stock concentration of 1.7×10^{13} particles/mL. The gold nanoparticles are coated with Poly-L-Lysine, which contains a positively charged hydrophilic amino group. At neutral or low pH (7 or

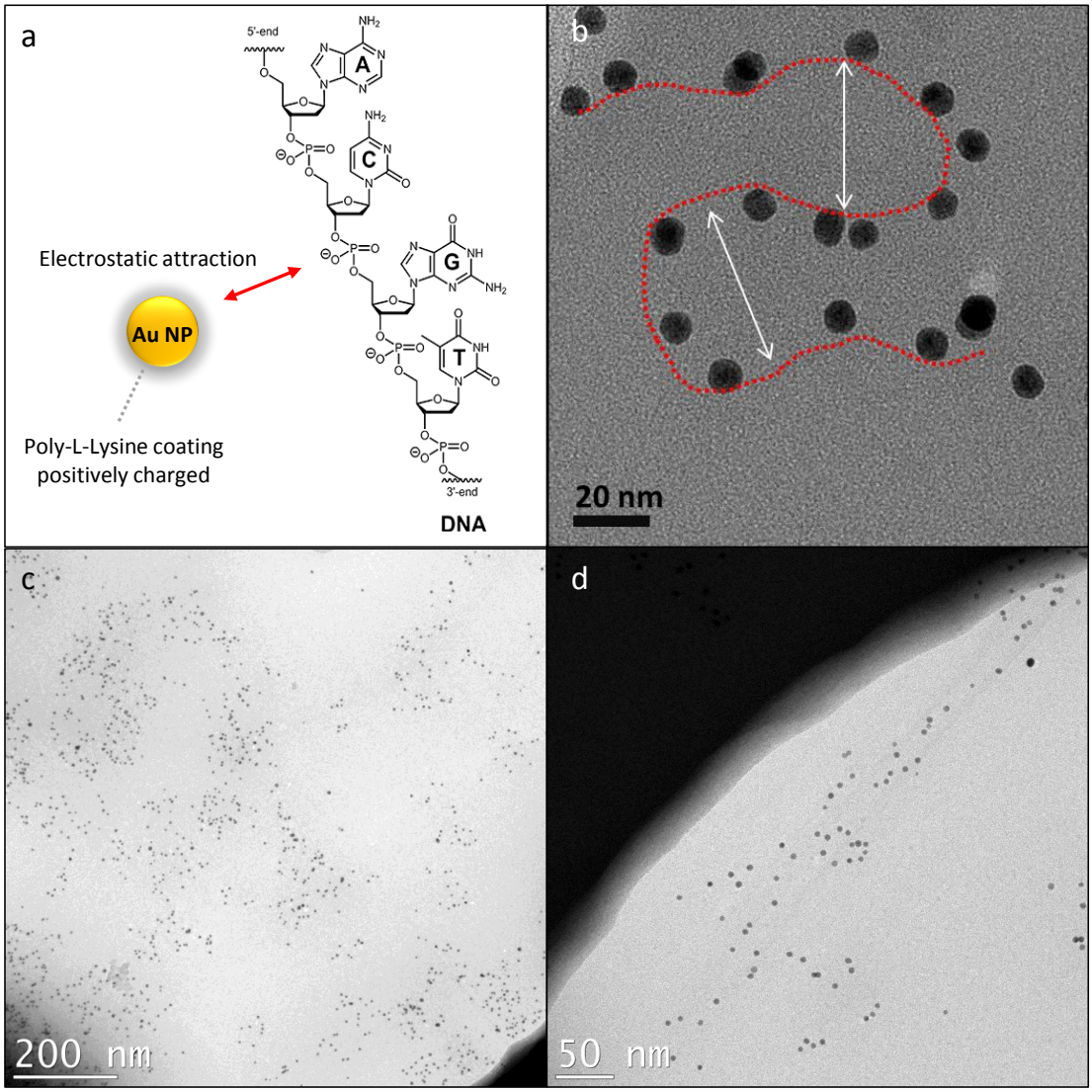

Figure 6–3: Cationic gold nanoparticle DNA labeling. (a) Schematic of cationic gold nanoparticle binding to the negatively charged phosphate backbone of DNA. (b) TEM images of cationic gold nanoparticle labeled molecules on a 50 nm nitride window. The curvature diameter is $\sim$50 nm, which is consistent with the DNA persistence length. (d) Lower magnification TEM image showing entangled DNA molecules together with Uranyl acetate salt residuals.

below), a net positive charge is introduced on the lysine coating due to its high isoelectric point, thus allowing the gold nanoparticle attach to the anionic site, which in

our case is the DNA phosphate backbone. Cationic gold nanoparticles are stored in a buffer consisting of 20 mM Tris (tris-hydroxymethyl-aminomethane), 20 mM sodium azide, 154 mM NaCl, 1% BSA(bovine serum albumin), 20% glycerol; pH 8.2. *DNA molecules* used in our experiments are Hind3 digested λ-DNA commercially available from NEB. T he stock DNA concentration is 500 μg/mL, stored in 10 mM Tris-HCl, 1 mM EDTA, pH 8.0.

To label the DNA with beads, we first dilute the DNA with DI water to a final concentration of 10 μg/mL. Then we mix 100 μL diluted DNA with 8 μL gold nanoparticles (stock concentration). The solution is carefully mixed in a 1 mL centrifuge tube and left for incubation. The incubation time varies from from 5 minutes to 24 hours. Longer incubation time leads to denser labeling, however complex DNA-nanoparticles conjugates are also formed, which are very challenging to distinguish under TEM. Figure 6–3 b-d are the TEM images of cationic gold nanoparticles labeled DNA after 5 minutes of incubation. The possible contour of DNA chain is indicated as red dashed line in figure 6–3 b. Accordingly, the curvature diameter of the chain is $\sim$ 50 nm, which is consistent with experimental observations of DNA persistence length [172, 173]. In addition, with longer gold nanoparticle-DNA incubation time (30 minutes), longer and more complex gold nanoparticle-DNA structures are presented in figure 6–3 c and d.

We introduce large silica spacer beads to control the thickness of the liquid cell. The silica beads have an average diameter of $\sim$ 100 nm and are mixed with the gold nanoparticle/DNA solution in the final step of our solution preparation. When sandwiched in the liquid cell, the beads keep the two graphene sheets separate. The thickness of the liquid cell is roughly defined by the diameter of the spacing silica beads, figure 6–4 f.

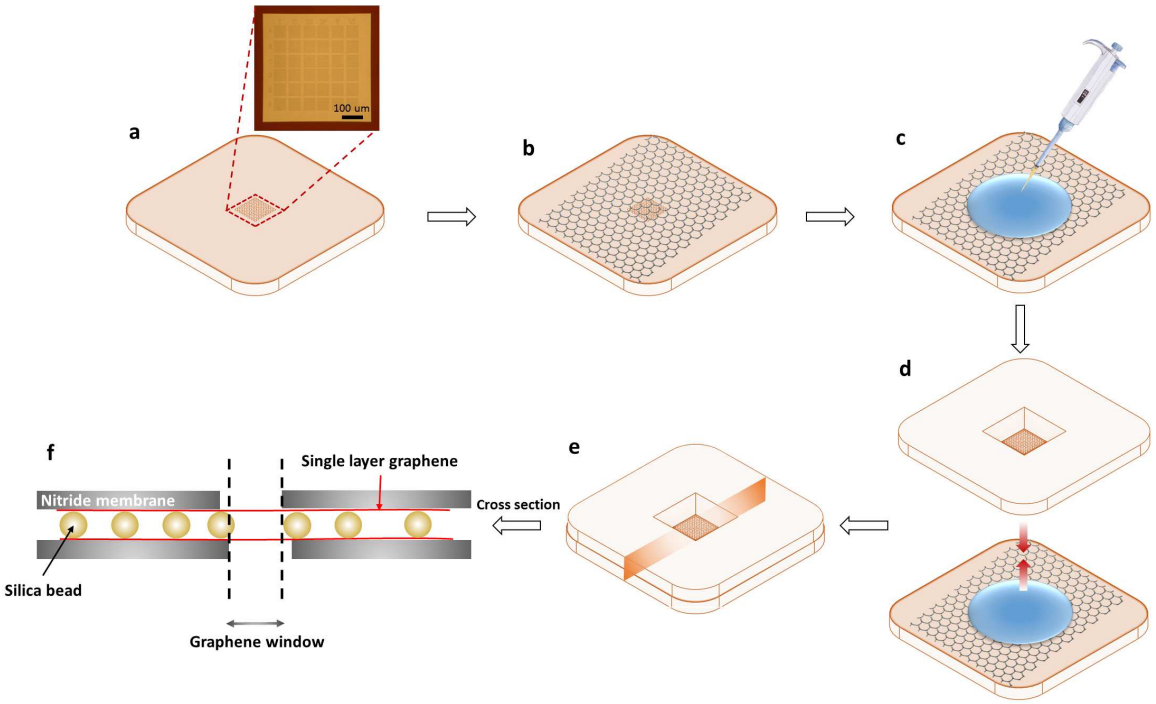

Figure 6–4: a) Cartoon of a nitride TEM grid with micron pore arrays. Inset shows optical microscope image of the central membranes. The scale bar is 100 μm. b) We transfer single layer graphene onto the grid and c) carefully pipette onto the pore arrays 2 μL of buffer containing gold nanoparticle-DNA conjugates and silica spacer beads. Then we d) carefully align two grids and press them together with tweezers. e) After desiccation, the graphene liquid cell is sealed, stabilized and ready for TEM imaging. f) Cell cross section showing spacer beads. (Figure not drawn to scale.

6.3.2 Graphene Liquid Cell Preparation

Liquid Cell Preparation

We prepare the liquid cell by sandwiching two identical nitride windows with pre-tranferred single layer CVD graphene. Figure 6–4 gives a detailed schematic of our assembly process. The nitride TEM window (Figure 6–4 a) has a membrane thickness of 50 nm and window size of 0.5 mm$\times$0.5 mm. The nitride window contains arrays of micron sized holes (2 μm diameter, 3 μm hole spacing) with location markings (I to VI, A to F) in both directions along the edges of membrane (Figure 6–4 a inset).

We first transfer single layer graphene onto the TEM grid, fully covering the window region (see figure 6–4 b). In order to ensure the grid does not move during construction of the cell, we then tape a corner of the grid onto filter paper (the filter paper also helps absorb any excess liquid). Afterwards, we pipette 2 μL of buffer containing DNA-nanogold conjugates and silica spacer beads onto the micropore arrays (figure 6–4 c). We then quickly position a second TEM grid, oriented upside down, on top of the first grid and press the two together with tweezers (figure 6–4 d). The alignment of the two grids is performed by hand so that the membrane region ($500\times500\,\mu m^2$) roughly overlaps. After assembly, we place the sandwiched grids into a desiccator and pump for 10 minutes in order to remove excessive liquid. This allows the two graphene layers to stick together forming a temporary seal. The desiccation process also stabilizes the sample and prevents leaking of water vapour during pump-down. Figure 6–5 is a top-down SEM image of the degassed graphene liquid cell.

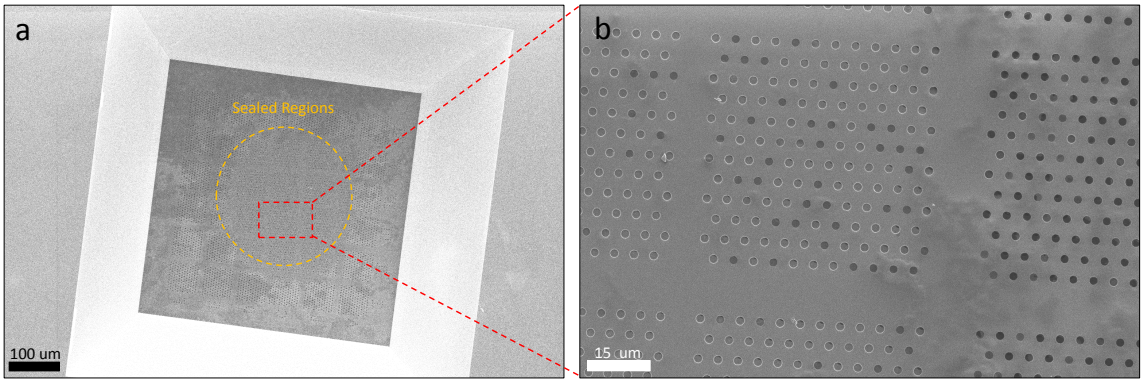

Figure 6–5: SEM images of the assembled liquid cell. (a) Top-down SEM image of the sandwiched liquid cell. The central square is the 0.5 mm×0.5 mm nitride membrane window with pore array. The yellow circle roughly indicates the sealed region. The scale bar is 100 μm. (b) Magnified SEM image of the micron sized window arrays; the scale bar is 15 μm.

6.4 Direct Observation of Gold Nanoparticle Dynamics in a Liquid Cell

The liquid cell is placed in a single tilt TEM holder and imaged with the FEI Tecnal G2 F20 Cryo-STEM under 200 kV TEM mode. We adjust the spot size of the electron beam so that the beam intensity is low in order to minimize electron beam induced hydrolysis and heating [24]. The nanoparticles' dynamics are recorded via two different methods: 1, We acquire and save images using the Gatan Microscopy Suite software with a certain time interval (around 5 s). 2, We capture the whole screen and record the video using a customized video recording program. In both cases, images are acquired at a magnification of 500× up to 800k× with a refresh rate of 1 Hz, acquisition time of 0.1 s per image. We set up the video recording system by splitting the original VGA signal from the TEM source computer and connect one of the output signal with a StarTech USB3HDCAP USB 3.0 video capture device. We record the videos at a resolution of 1440×900 and 60 FPS (frames per second) in AVI (audio video interleaved) format using a commercially available video capture program (StreamCatcher).

Figure 6–6 shows a demonstration of a successfully sealed graphene liquid cell. Two micron sized holes on the top and bottom TEM windows roughly overlap, allowing graphene layers to be directly exposed to the high vacuum ($< 10^{-7}$ Torr) and electron beam. In the overlap region, two free standing graphene layers sandwich a thin layer of liquid containing 10 nm cationic gold nanoparticles (black dots). The layer is around 100 nm thick, defined by the diameter of spacing silica beads. In this example we sandwich only free cationic gold nanoparticles. Figure 6–6 b–e shows a magnified image of the central overlap region (red rectangular) at t=0, 5, 10, 15 s. The relative position of the marked particles (indicated with dashed ellipses) varies over time, demonstrating

the successful recording of nanoparticle diffusive displacements at nanoscale with our liquid cell.

Free gold nanoparticles in the graphene liquid cell are expected to undergo diffusive motion. According to the Stokes-Einstein equation, the diffusion coefficient for a particle with radius R in water is

$$D = \frac{k_B T}{6\pi\eta \cdot R} \approx 4.4 \times 10^{-11}\, m^2 \cdot s^{-1} \tag{6.1}$$

where R is the nanoparticle radius, $R = 5\,nm$ and k_B is Boltzmann's constant. The temperature T = 300 K and the viscosity of water is $\eta = 1{\times}10^{-3}$ Pa·s. The mean diffusion length is $L_D = \sqrt{Dt}$, which characterize the average diffusion length of the particle over a certain period of time t. The particle dynamics acquisition rate for our experiment is 1 Hz (1 frame per second). Accordingly, the calculated diffusion length per frame will be $6.6 \times 10^{-6}\, m = 6.6\,\mu m$. And if we set the average diffusion length to be 1 nm, t=2.27 $\times 10^{-8}$ s. This means to record nanoparticle dynamics with an average step size of 1 nm, a sampling frequency of 4.4×10^7 Hz is required, which is far beyond the reach of our CCD. However, surprisingly, if we check the diffusion lengths of all particles in figure 6–6, the diffusion lengths over 5 s are in fact in the order of 1–10 nm, which are several orders of magnitude lower than theoretical prediction ($L_D = \sqrt{Dt} = 14.8\,\mu m$, $D = 4.4 \times 10^{-11}\, m^2 \cdot s^{-1}$, $t = 5\,s$).

6.5 Results and discussion

We performed a series of quantitative analysis on gold nanoparticle dynamics using our newly developed liquid cell technique. First we perform Pearson correlation analysis to conform the existence of DNA-nangold conjugates. Secondly, we analyze mean-square displacement (MSD) curves for single particles, quantifying single particle diffusion constants and investigating whether the diffusion is of normal or anomalous

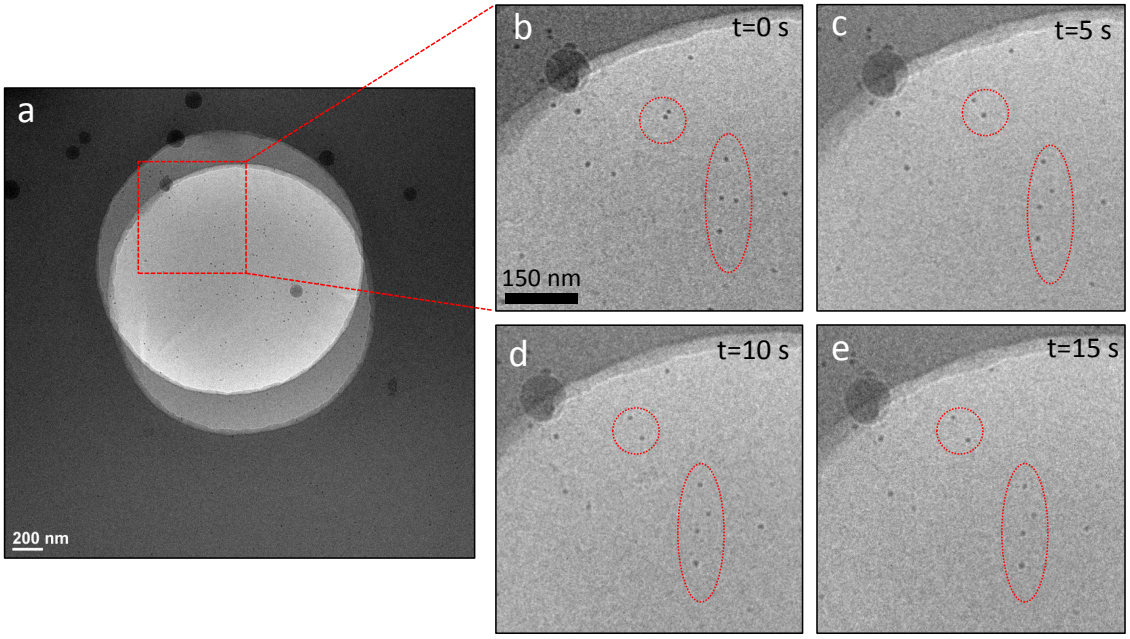

Figure 6–6: TEM images of gold nanoparticles in graphene liquid cell. a) TEM image of a successfully sealed graphene liquid cell. Graphene is directly exposed to the high vacuum of TEM ($< 10^{-7}$ Torr) in the micron scale overlap region. The black circles with ~ 100 nm diameter are the spacing silica beads. b) to e) Zoomed in TEM images showing a region ($600 \times 600\,\text{nm}^2$) of the liquid cell. Images are taken at $t = 0, 5, 10, 15$ s. The black dots are the 10 nm gold nanoparticles. Nanoparticles with displacements are indicated in the dashed circles. The scale bar is 150 nm.

character. To keep the experimental conditions consistent, we analyzed the particle dynamics in only one liquid cell. In this liquid cell, we sandwiched $2\,\mu L$ of cationic gold nanoparticles (10 nm)/Hind3 digested λ-DNA mixed solution. The thickness of the liquid cell is ~ 100 nm, controlled by the diameter of the spacing silica beads. We first recorded the trajectories of all nanoparticles through TEM. Then we performed the tracking and extracted the coordinates of each particle with a customer plugin through ImageJ [174]. We completed the analysis of the particle dynamics (particle trajectory reconstruction, MSD/anomalous diffusion analysis and Pearson correlation coefficient calculation) with MATLAB. All analysis results are presented as follows.

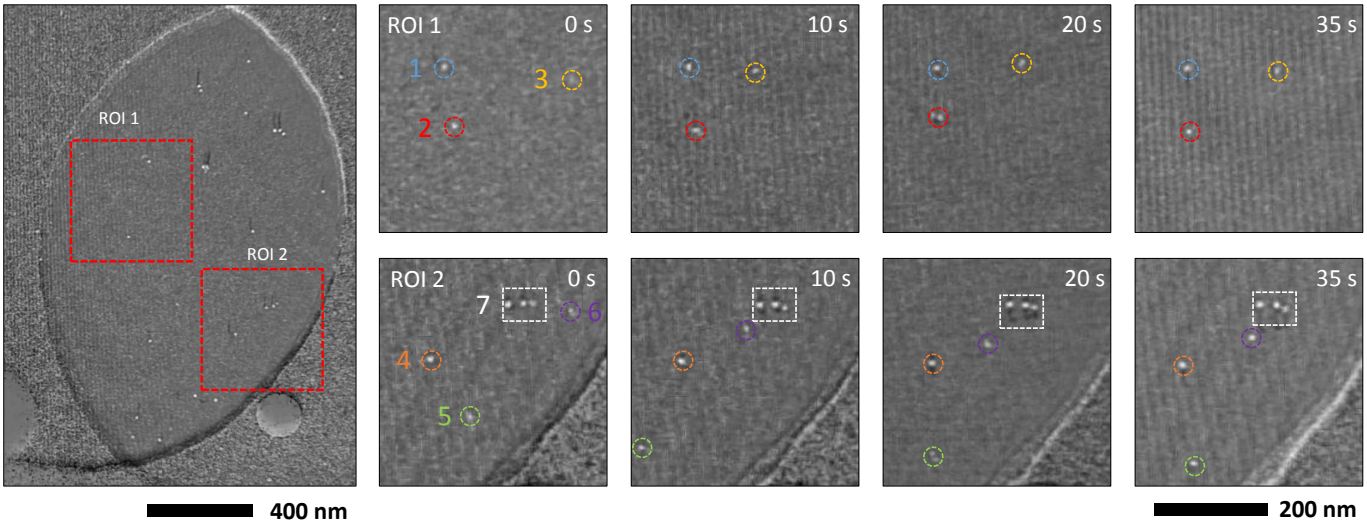

Figure 6–7: Processed TEM image of the graphene liquid cell. The intensity is inverted using Matlab for particle tracking. Gold nanoparticles are shown as white dots. Two regions of interest from the graphene overlaped region are selected for further analysis (marked as ROI1 and ROI2). ROI1 contains three free nanoparticles, labeled as 1, 2 and 3. ROI2 contains three free nanoparticles 4, 5, 6 and a trimer 7 (the trimer includes three gold nanoparticles linked by DNA).

Identification of DNA-Nanogold Conjugates. We first select two regions of interest from the overlap region (labeled ROI1 and ROI2, see figure 6–7). The dynamics of three 10 nm gold nanoparticles (labeled as 1, 2 and 3) are included in ROI1 and the dynamics three gold nanoparticles (labeled as 4, 5 and 6) are included in ROI2. In addition, in ROI2, we believe we see a DNA linked nanoparticle trimer (labeled as 7). Figure 6–8 shows the motion of single particles and the DNA-gold conjugate taken from RO1 and RO2.

We use Pearson correlation analysis [7] to rigorously distinguish free nanoparticles from the nanoparticle-DNA conjugates. The Pearson correlation coefficient is defined as

$$r_{X,Y} = \frac{cov(X,Y)}{\sigma_X \sigma_Y} \tag{6.2}$$

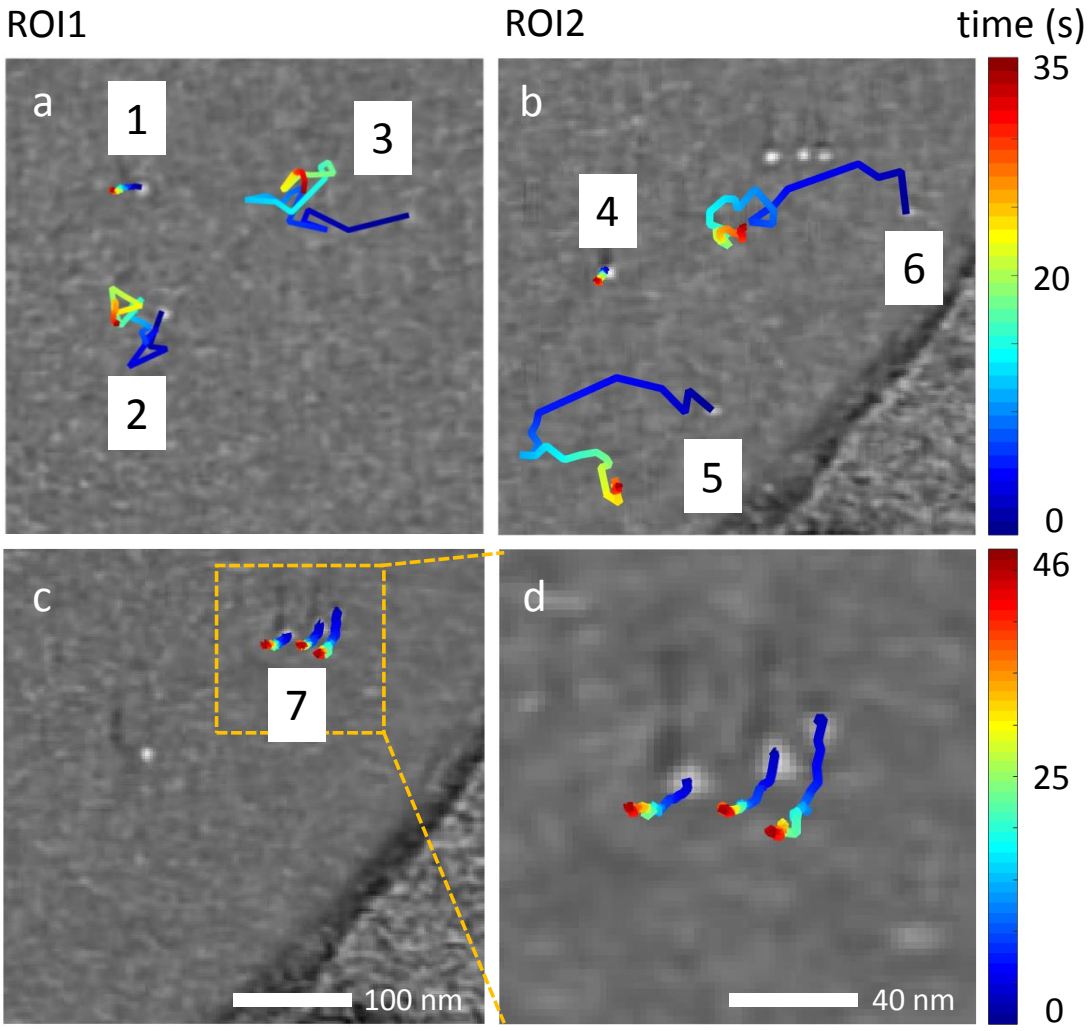

Figure 6–8: Gold nanoparticle diffusion in a graphene liquid cell. (a) Time series trajectories of three gold nanoparticles from ROI1 (see Fig. 6–7). The image shows time trajectories of each individual nanoparticle imaged for a total duration of 35 s (0 s to 35 s, frame rate 1 Hz). (b) Time series trajectories of three gold nanoparticles from ROI2 (see Fig. 6–7, the particles are imaged for a duration of 35 s). (c) Time series trajectories of a DNA linked nanoparticle trimer (imaged for a duration of 46 s). (d) Magnified view of the trimer trajectory. The scale bar in (c) is 100 nm, shared with (a) and (b). The scale bar in (d) is 40 nm.

where $cov(X, Y)$ is the covariance between variable X and Y, σ_X and σ_Y is the standard deviation of X and Y. The correlation coefficient is a measure of the linear dependence

between two variables X and Y, with a value between $+1$ and -1, where $+1$ means total positive linear correlation, -1 means total negative linear correlation and 0 means no linear correlation.

We calculated the Preason correlation coefficients for all particles (in pairs) in ROI1 and ROI2. Using this approach, we are able to distinguish a trimer (particle T1, T2 and T3) from the rest of particles (particle 1 to 6). The correlation coefficients of particles' (x, x) and (y, y) coordinates are listed in the table in figure 6–9 b. We find $r_{x,x}$ and $r_{y,y}$ for T1–T2, T1–T3 and T2–T3, are close to 1, indicating highly positive linear correlation between the trimer (presumably caused by the conjugation of DNA molecules). In contrast, $r_{x,x}$ and $r_{y,y}$ for particle 1 to 6 are far from ± 1, showing weak correlations. Figure 6–10 gives the average inter-particle spacing between the gold nanoparticles along the trimer. The spacing is roughly constant, additional evidence suggesting that the trimer constitutes a linked DNA nanoparticle assembly.

Analysis of Single Particle MSD Curves. The particle mean squared displacement (MSD) is defined:

$$MSD(\tau) = \langle (\Delta r(\tau))^2 \rangle = \langle [r(t+\tau) - r(t)]^2 \rangle \tag{6.3}$$

where τ is the time lag of the same particle at two different positions ($r(t+\tau)$ and $r(t)$) and $\Delta r(\tau)$ is the position displacement over time τ. Typically, Eq. 6.3 is evaluated by obtaining an ensemble of realizations of the random walk and then averaging over the ensemble. However, in our experiment, we measure single-particle trajectories. In order to obtain the MSD for a single-particle trajectory, we convert the trajectory into an ensemble of displacements occurring at fixed lag τ, averaging over all displacements

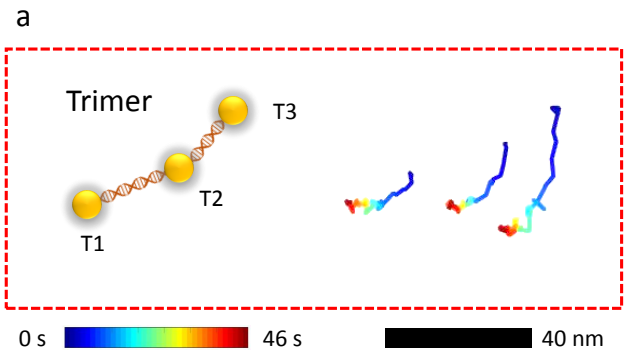

b

Particles	$r_{x,x}$	$r_{y,y}$
T1 - T2	0.9816	0.9451
T1 - T3	0.9713	0.9105
T2 - T3	0.9565	0.9672
1 - 2	0.8030	-0.5542
1 - 4	0.8341	0.7932
5 - 6	0.5694	0.7824

Figure 6–9: Particle trajectories and Pearson correlation analysis. (a) Cartoon showing the DNA gold nanoparticle conjugate trimer (labeled as 7 in figure 6–7 and figure 6–8, or T1, T2 and T3 in this figure) Time series trajectories of T1, T2 and T3 over a total time of 46 s. (b) A table of calculated Pearson correlation measuring the linear correlation coefficients between nanoparticles $x - x$ and $y - y$ coordinates. The correlation coefficients ($r_{x,x}$ and $r_{y,y}$) between T1, T2 and T3 are close to 1, indicating strong correlations. While the correlation coefficients between particle 1–2, 1–4 and 5–6 are far from ± 1, indicating weak correlations. Particle 1 to 6 are labeled in figure 6–7 and figure 6–8, randomly selected into pairs for the calculation of correlation coefficients from a total possible $C_6^2 = 15$ combinations.

n at fixed lag time (see figure 6–11):

$$MSD(\tau) = \langle(\Delta r(\tau))^2\rangle = \frac{1}{n}((\Delta r_1(\tau))^2 + (\Delta r_2(\tau))^2 + (\Delta r_3(\tau))^2 + ...) = \frac{1}{n}\sum_{i=1}^{n} \Delta r_i^2(\tau) \tag{6.4}$$

Note that the number of displacements will decrease as the lag-time increases, so statistics will worsen for increasing lag time.

For normal diffusion, the mean squared displacement (MSD) of the particles scales linearly with time

$$\langle r^2\rangle \sim Dt \tag{6.5}$$

Given a n dimensional isotropic diffusion, the mean squared displacement is

$$\langle r^2\rangle = 2nDt \tag{6.6}$$

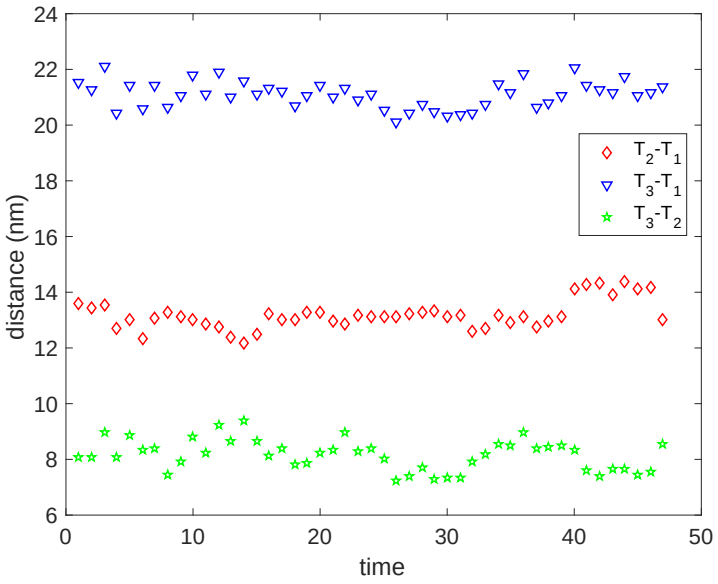

Figure 6–10: The fluctuation in inter-particle distance along the timer (T1, T2 and T3).

In our case, the trajectories of gold nanoparticles is projected to a two dimensional plane, giving us an $n = 2$. Thus the calculated diffusion coefficient will be

$$D = \frac{\langle r^2 \rangle}{4t} \tag{6.7}$$

However, a diffusion process can have a non-linear relationship with time, in which case it is called "anomalous." A more general form of the mean squared displacement can be written:

$$\langle r^2(t) \rangle \sim t^{\alpha} \tag{6.8}$$

Anomalous diffusion is classified through the scaling index or anomalous diffusion index α. For $\alpha = 1$, the diffusion is normal diffusion, figure 6–12 a. For α>1, the diffusion is termed as super-diffusive process, figure 6–12 b, including the special case $\alpha = 2$, which is called ballistic diffusion. For α<1, the diffusion is called sub-diffusive process [175].

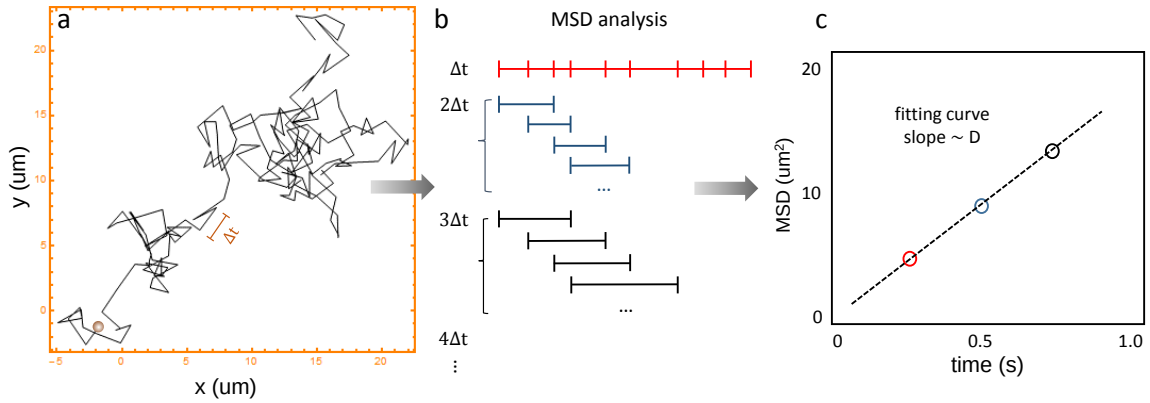

Figure 6–11: MSD analysis for single particle trajectory. (a) The trajectory of a single particle undergoes 2D Brownian motion (generated via Mathematica). (b) Ensembles of mean squared displacements corresponding to varying lag-time ($\Delta t, 2\Delta t, 3\Delta t \cdots$). (c) The diffusion coefficient is derived from the slope of the fitting curve.

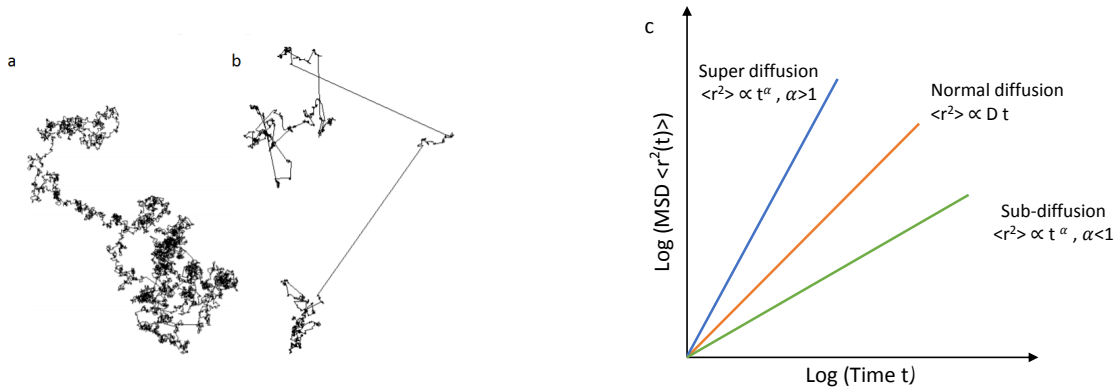

Figure 6–12: (a) The trajectory of a random walk for normal diffusion. (b) Random walk trajectories for anomalous diffusion, figure reproduced from [175]. (c) Log $\langle r^2 \rangle$ vs log t. In the case of normal diffusion, $\alpha = 1$. In the case of super diffusion, $\alpha > 1$. In the case of sub-diffusion, $\alpha < 1$.

We first assume all particles undergo normal diffusive movement and calculate the goodness of fit (R^2). If the goodness of fit for a certain particle is far from 1, the diffusive process is likely anomalous. Accordingly, for i = 1 to 6, the goodness of fit (R^2) for each fit is R_i^2 = 0.988, 0.606, 0.471, 0.991, 0.966 and 0.963. The R^2 of particle 1, 4, 5 and 6 are indeed very close to 1, indicating particles follow normal diffusion. However the R^2 of particle 2 and 3 deviate significantly from 1, suggesting these two particles do not follow normal diffusion. In addition, we can directly obtain the anomalous diffusion index (α) of the particles. Figure 6–14 presents the log-log scale MSD vs time latency plot. The slope of each linear fitting line corresponds to the anomalous diffusion index (α). We find α_1 = 1.146, α_2 = 0.571, α_3 = 0.504, α_4 = 0.913, α_5 = 0.933, α_6 = 0.875. The anomalous diffusive index for particle 1, 4, 5 and 6 are close to 1, indicating particles following normal diffusive movements (Brownian motion), while α_2 and α_3 are close to 0.5, demonstrating that particle 2 and 3 undergo sub-diffusive movement.

In addition to observing anomalous diffusion, we observe a large spread in the extracted diffusion constants with much smaller values than expected for bulk diffusion. The diffusion coefficient of each particle, extracted assuming normal diffusion, is D_i = 0.973, 17.025, 48.322, 0.495, 134.247 and 89.316 nm^2/s, figure 6–13. The diffusion coefficient ranges from 1 – 100 nm^2/s, which is 10^5 – 10^7 times lower, when compared with the theoretical value – $4.4 \times 10^7\, nm^2 \cdot s^{-1}$. Strongly damped diffusive movement is also reported for nanoparticles confined in a nanodroplet inside a nitride liquid cell by Lu *et al* in 2014 [176]. Lu reported an increase of 10^9 in corresponding effective viscosity (9 orders of magnitude lower in diffusion coefficient) comparing the nanodroplet with the bulk liquid. This observed damping effect is likely caused by the dominating surface effects in an untrathin film of liquid close to the surfaces [176]. The thin liquid film is

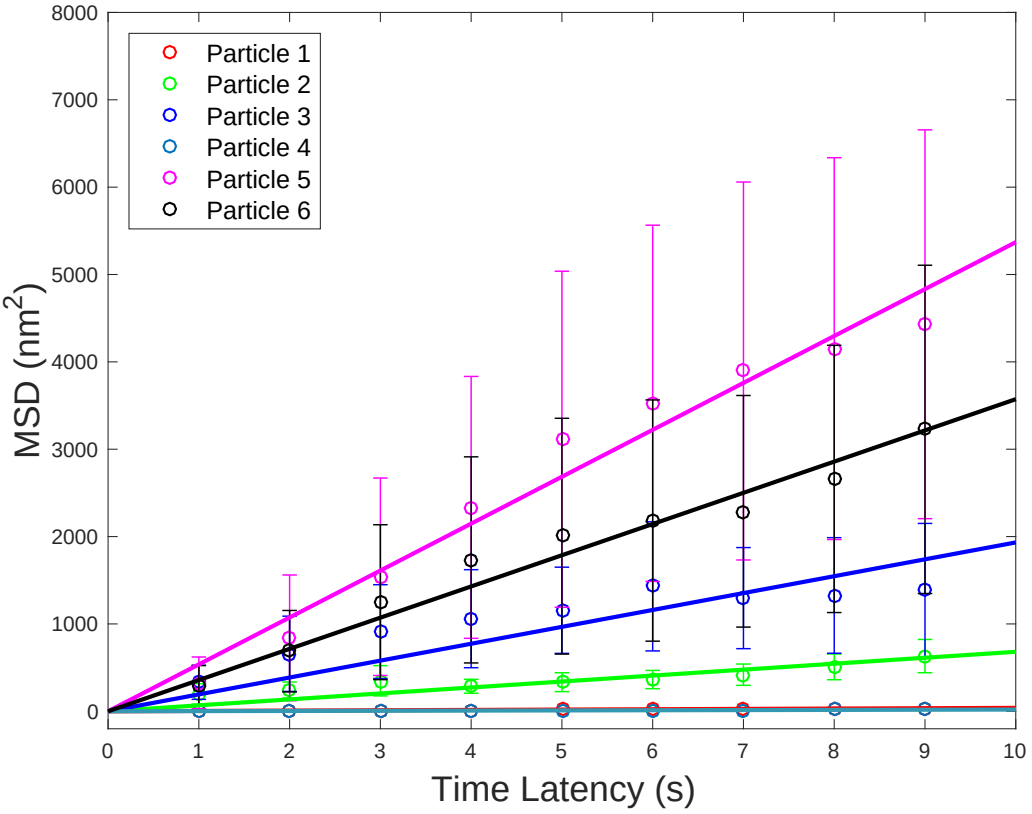

Figure 6–13: MSD/diffusion coefficient analysis. Linear scale MSD (nm^2) vs time latency (s) plot for particle 1 to 6. The diffusion coefficient (D) is obtained from extracting the slope of each linear fitting line ($D = slope/4$ for two dimensional diffusion). All lines are forced to to pass though the origin. For $i = 1$ to 6, the diffusion coefficient is $D_i = 0.973$, 17.025, 48.322, 0.495, 134.247 and $89.316\, nm^2/s$. The goodness of fit is $R_i^2 = 0.988$, 0.606, 0.471, 0.991, 0.966 and 0.963, respectively.

reported to have a typical thickness of 10 – 20 nm, which is comparable to the diameter of the nanoparticles [176]. The few monolayers of liquid molecules within this layer close to the membranes will have different properties (such as dramatic increase of viscosity and molecular friction) when compared with those of bulk liquid [177, 178, 179].

Here we speculate on possible physical origins of the observed anomalous diffusion and the large spread in observed diffusion constants in our system. One possibility

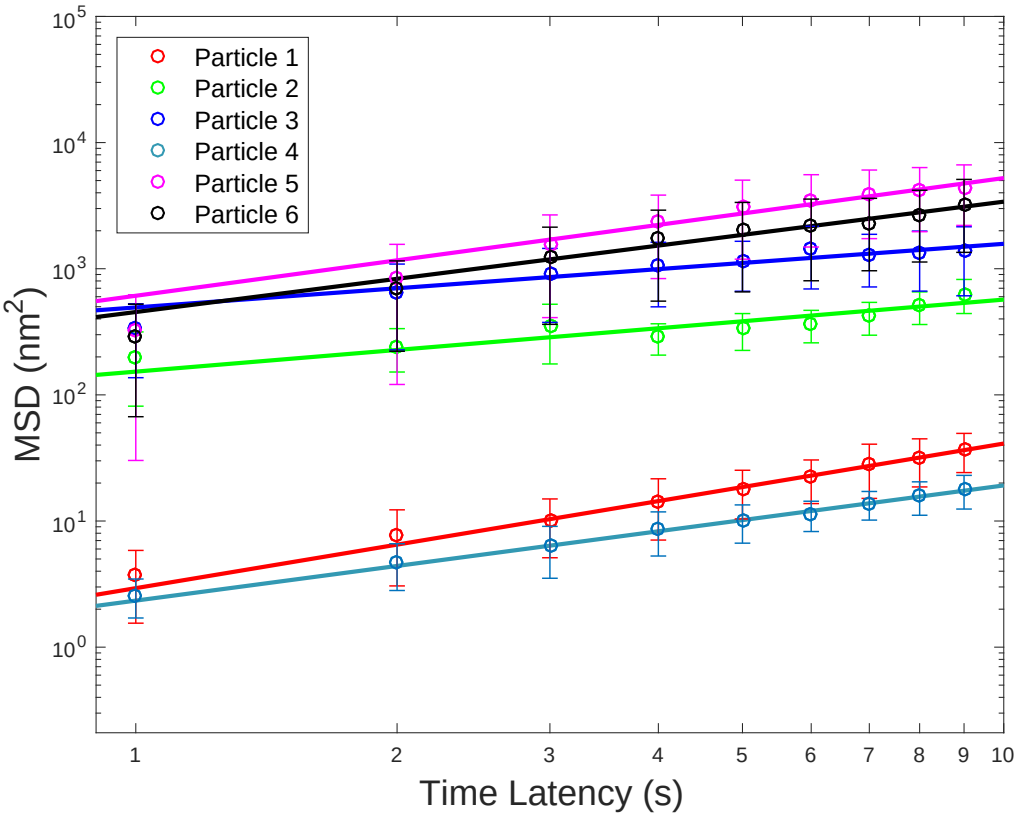

Figure 6–14: Anomalous diffusion analysis. Log-log scale MSD (nm^2) vs time lag (s) plot for particle 1 to 6. The anomalous diffusion index (α) is obtained from extracting the slope of each linear fitting line ($\alpha = slope$, $\alpha_1 = 1.146 \pm 0.037$, $\alpha_2 = 0.571 \pm 0.118$, $\alpha_3 = 0.504 \pm 0.077$, $\alpha_4 = 0.913 \pm 0.031$, $\alpha_5 = 0.933 \pm 0.091$, $\alpha_6 = 0.875 \pm 0.076$).

is that the viscosity is not spatially constant. In particular, thin boundary layers may exist, very close to the top and bottom surfaces and with typical thickness of 10 – 20 nm, that have dramatically increased viscosity such as observed in the liquid droplet [177, 178, 179]. The viscosity away from the boundary layers is similar to that of the bulk liquid (much lower viscosity when compared with the boundary layer). We expect our liquid cell to have a total thickness of ~ 100 nm, so that the boundary layers occupy a moderate fraction of the total volume, and the system can be modelled as a three

layer sandwich structure made up of the top viscous layer, normal middle layer and bottom viscous layer (see figure 6–15). While we access experimentally only the two dimensional projection of the nanoparticle diffusive motion, the particles also diffuse in z and sample the boundary layers. The spatial variation of viscosity then leads leads to a spatially varying nanoparticle diffusion coefficient D. It is plausible that particles get periodically trapped in the viscous boundary layers, leading to a spread of diffusion constants and anomalous diffusion. Particle surface interactions may also play a role. Recent studies report possible electrostatic interaction between the charged graphene layer and gold nanoparticles [140, 180]. Such surface-particle interactions might lead to a slow down of particle diffusion. A good way to minimize such effect is imaging at lower beam intensity and discharge the graphene layer.

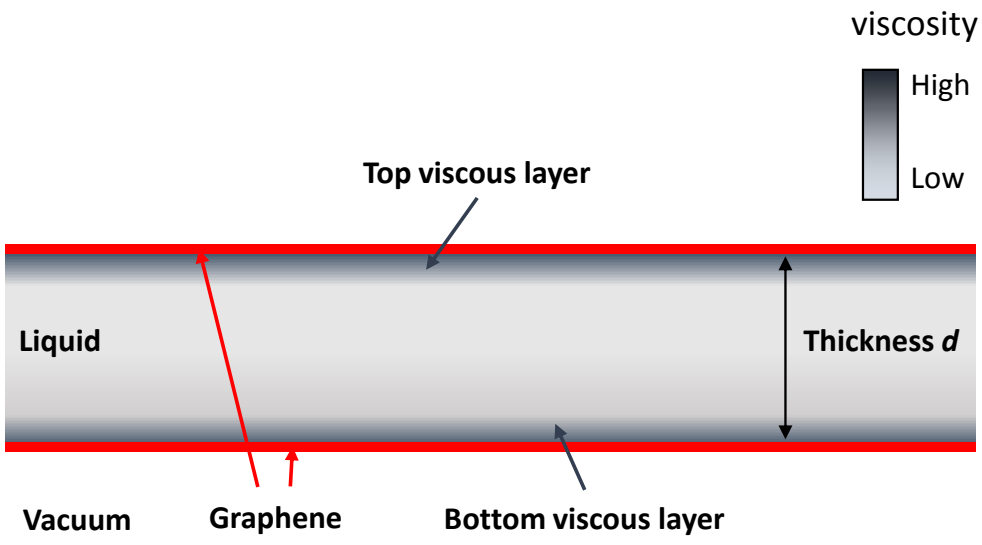

Figure 6–15: The sandwich model for liquid layers. We hypothesize that the liquid cell can be described via a sandwich model, including two viscous layers close to the graphene surfaces and a middle layer with viscosity closer to bulk.

6.6 Conclusion

To conclude, we have successfully developed a hybrid liquid cell with micron-scale viewing window for in *situ* TEM. The hybrid liquid cell combines the outstanding mechanical stability of a nitride liquid cell and the ultra high resolution of a graphene liquid cell. With this technique, we are able to record the dynamics of nanoparticles in liquid with nanometer resolution. In addition, our experimental observation shows that for nanoparticle confinement at a length-scale comparable to the size of its diameter (10 to 100 nm), the diffusion coefficient of the nanoparticle is decreased by several orders of magnitude ($10^5 \sim 10^7$) when compared with expected bulk diffusion.

CHAPTER 7
Conclusion

7.1 Summary

In this dissertation we combine nanofluidic features (nanopore, nanochannel) with thin membranes (nitride membrane, single layer graphene) to develop three novel devices for single molecular imaging and sensing. In addition, we develop a novel technique for creating solid state nanopore sensors on thin nitride membranes.

In chapter 3, we pioneered the integration of nanopores into complex nanochannel systems and developed a nanopore/nanochannel fluidic chip for single molecular DNA sensing and manipulation. We demonstrated the single molecule level manipulation of ds-DNA molecule in nanochanels and nanopores by tuning voltage and pneumatic pressure. The fluorescent microscopy compatibility of the system allows us to optically detect and analyze ds-DNA molecules. In addition, we developed a new nitride to glass low temperature bonding protocol. Bonding is the most challenging aspect of fabricating nanofliudic devices.

In chapter 4, we developed a novel nanopore fabrication technique based on conductive atomic force microscopy and dielectric breakdown. This technique combines the simplicity of dielectric breakdown technique and nanometer positioning, surface characterization capability of AFM. We demonstrated the successful fabrication of nanopore and nanopore arrays on nitride membranes. This technique may greatly reduce the cost per pore when compared with conventional high energy beam nanopore fabrication techniques as it does not require high vacuum systems. The technique also

preserves the capability of precise positioning of nanopore by simply moving the AFM tip, when compared with conventional electric breakdown technique.

In chapter 5, we invented a novel liquid cell for SEM using single layer CVD graphene as the window. We demonstrated that single layer CVD graphene is very promising for SEM based liquid cell imaging, enabling dynamic imaging of gold nanoparticles undergoing Brownian motion in aqueous solution with a sub 5 nm resolution and EDX measurements in liquid. We are the first to video nanoparticle dynamics in a micron wide graphene liquid cell using both secondary and backscattering electron mode.

In chapter 6, we invented a new liquid cell for in *situ* TEM technique combing the outstanding mechanical stability of nitride liquid cell and ultra high resolution of conventional graphene liquid cell. With the new cell, we were able to record the dynamics of nanoparticles in liquid with nanometer resolution across micron scale. We observed the dramatic slowing down of diffusive motions of nanoparticles when confined in nanoscale. We were the first to report the observation of broad distribution of nanoparticle diffusion coefficients ($1 - 100\, nm^2/s$) in the same liquid cell. We performed a series of quantitative analyses, including MSD, anomalous diffusion and Pearson correlation analysis to further quantify nanoparticle dynamics. We also proposed a "sandwich model" to describe the liquid layers for better explaining anomalous diffusive behaviours and the broad distribution of particle diffusion coefficients.

7.2 Future perspectives

This dissertation has demonstrated the successful development of new nanofluidic systems and techniques for single molecular sensing and imaging. In this final section of this dissertation I will discuss possible future improvements, extended experiments and potential applications based on the devices and techniques we have developed.

One way to improve the nanopore/nanochannel design (Chapter 3) would be to build local Ag/AgCl electrodes close to the nanopore and perform electric detection. With the capability of performing pico ampere (pA) level electric detection–separating sensing and control signal–the nanopore/nanochannel design might greatly improve the signal to noise ratio and gain control over DNA translocation speed. The ideal of combing nanochannels with embedded nanopores could potentially be a important future direction of nanopore based DNA/protein sequencing technology. In addition, the nanoscale "window" structure of the nanopore/nanochannel design allows us to probe and select a certain molecule and pull it through the nanopore into the membrane interfaced macro-reservoir (where chemical exchanges can be conveniently performed).

In chapter 4, we report the development of a novel nanopore fabrication technique based on conductive atomic force microscopy and dielectric breakdown. To further improve and extend this technology, we will need to demonstrate the fabrication of sub-10 nm pores. DNA sensing experiments with nanopores fabricated using our technique also need to be demonstrated. Another direction is to create nanopores in completely dry conditions using our technique. We believe that conductive AFM tip can be used as a local electrode on one side of a nitride coated silicon wafer, while applying a breakdown voltage between the tip and the silicon wafer, figure 4–15. After photolithography, RIE and KOH etching to remove the bulk silicon beneath the pores, we would form a potentially wafer scale nanopore/nanopore array. This dry nanopore fabrication technique will not only greatly simplify the nanopore fabrication process and be efficiently applied at low cost in industry but also enables the transverse nanopore design, high lighted in the editorial issue "Building a better nanopore" in Nature Nanotechnology [181].

In chapter 5 and 6, we demonstrate that single layer graphene is very promising for SEM/TEM based liquid cell imaging. In the future, instead of imaging specimen in a sandwich structure, we can incorporate graphene with nanofluidic structures (nanochannel, nanopore). Such combination would give rise to new types of single-molecule analytical graphene nanofluidic devices, with the capability of manipulating single molecules based on nanoconfinement as well as imaging molecules with nanometer resolution through electron microscopy.

References

[1] Cees Dekker. Solid-state nanopores. *Nature nanotechnology*, 2(4):209–215, 2007.

[2] Niels de Jonge and Frances M Ross. Electron microscopy of specimens in liquid. *Nature nanotechnology*, 6(11):695–704, 2011.

[3] John J Kasianowicz, Eric Brandin, Daniel Branton, and David W Deamer. Characterization of individual polynucleotide molecules using a membrane channel. *Proceedings of the National Academy of Sciences*, 93(24):13770–13773, 1996.

[4] Mohammad M Mohammad, Sumit Prakash, Andreas Matouschek, and Liviu Movileanu. Controlling a single protein in a nanopore through electrostatic traps. *Journal of the American Chemical Society*, 130(12):4081–4088, 2008.

[5] Yong Wang, Dali Zheng, Qiulin Tan, Michael X Wang, and Li-Qun Gu. Nanopore-based detection of circulating micrornas in lung cancer patients. *Nature nanotechnology*, 6(10):668–674, 2011.

[6] Jong Min Yuk, Jungwon Park, Peter Ercius, Kwanpyo Kim, Daniel J Hellebusch, Michael F Crommie, Jeong Yong Lee, A Zettl, and A Paul Alivisatos. High-resolution em of colloidal nanocrystal growth using graphene liquid cells. *Science*, 336(6077):61–64, 2012.

[7] Qian Chen, Jessica M Smith, Jungwon Park, Kwanpyo Kim, Davy Ho, Haider I Rasool, Alex Zettl, and A Paul Alivisatos. 3d motion of dna-au nanoconjugates in graphene liquid cell electron microscopy. *Nano letters*, 13(9):4556–4561, 2013.

[8] Jungwon Park, Hyesung Park, Peter Ercius, Adrian F Pegoraro, Chen Xu, Jin Woong Kim, Sang Hoon Han, and David A Weitz. Direct observation of wet biological samples by graphene liquid cell transmission electron microscopy. *Nano letters*, 15(7):4737–4744, 2015.

[9] BS Bull, MA Schneiderman, and George Brecher. Platelet counts with the coulter counter. *American journal of clinical pathology*, 44(6):678–688, 1965.

[10] M Koch, AGR Evans, and A Brunnschweiler. Design and fabrication of a micromachined coulter counter. *Journal of Micromechanics and Microengineering*, 9(2):159, 1999.

[11] Jiali Li, Marc Gershow, Derek Stein, Eric Brandin, and JA Golovchenko. Dna molecules and configurations in a solid-state nanopore microscope. *Nature materials*, 2(9):611–615, 2003.

[12] Bala Murali Venkatesan and Rashid Bashir. Nanopore sensors for nucleic acid analysis. *Nature nanotechnology*, 6(10):615–624, 2011.

[13] Yann Astier, Orit Braha, and Hagan Bayley. Toward single molecule dna sequencing: direct identification of ribonucleoside and deoxyribonucleoside 5 - monophosphates by using an engineered protein nanopore equipped with a molecular adapter. *Journal of the American Chemical Society*, 128(5):1705–1710, 2006.

[14] T Laver, J Harrison, PA ONeill, K Moore, A Farbos, K Paszkiewicz, and David J Studholme. Assessing the performance of the oxford nanopore technologies minion. *Biomolecular detection and quantification*, 3:1–8, 2015.

[15] Amit Meller, Lucas Nivon, Eric Brandin, Jene Golovchenko, and Daniel Branton. Rapid nanopore discrimination between single polynucleotide molecules. *Proceedings of the National Academy of Sciences*, 97(3):1079–1084, 2000.

[16] Christopher A Merchant, Ken Healy, Meni Wanunu, Vishva Ray, Neil Peterman, John Bartel, Michael D Fischbein, Kimberly Venta, Zhengtang Luo, AT Charlie Johnson, et al. Dna translocation through graphene nanopores. *Nano letters*, 10(8):2915–2921, 2010.

[17] Walter Reisner, Jason P Beech, Niels B Larsen, Henrik Flyvbjerg, Anders Kristensen, and Jonas O Tegenfeldt. Nanoconfinement-enhanced conformational response of single dna molecules to changes in ionic environment. *Physical review letters*, 99(5):058302, 2007.

[18] Walter Reisner, Niels B Larsen, Asli Silahtaroglu, Anders Kristensen, Niels Tommerup, Jonas O Tegenfeldt, and Henrik Flyvbjerg. Single-molecule denaturation mapping of dna in nanofluidic channels. *Proceedings of the National Academy of Sciences*, 107(30):13294–13299, 2010.

[19] Harold Kwok, Kyle Briggs, and Vincent Tabard-Cossa. Nanopore fabrication by controlled dielectric breakdown. *PloS one*, 9(3):e92880, 2014.

[20] Jong Min Yuk, Kwanpyo Kim, Benjamín Alemán, William Regan, Ji Hoon Ryu, Jungwon Park, Peter Ercius, Hyuck Mo Lee, A Paul Alivisatos, Michael F Crommie, et al. Graphene veils and sandwiches. *Nano letters*, 11(8):3290–3294, 2011.

[21] Ke Xu, Peigen Cao, and James R Heath. Graphene visualizes the first water adlayers on mica at ambient conditions. *Science*, 329(5996):1188–1191, 2010.

[22] Dan Li and Richard B Kaner. Graphene-based materials. *Nat Nanotechnol*, 3:101, 2008.

[23] Alexander A Balandin, Suchismita Ghosh, Wenzhong Bao, Irene Calizo, Desalegne Teweldebrhan, Feng Miao, and Chun Ning Lau. Superior thermal conductivity of single-layer graphene. *Nano letters*, 8(3):902–907, 2008.

[24] Dongha Shin, Jong Bo Park, Yong-Jin Kim, Sang Jin Kim, Jin Hyoun Kang, Bora Lee, Sung-Pyo Cho, Byung Hee Hong, and Konstantin S Novoselov. Growth dynamics and gas transport mechanism of nanobubbles in graphene liquid cells. *Nature communications*, 6, 2015.

[25] Hagan Bayley. Membrane-protein structure: Piercing insights. *Nature*, 459(7247):651–652, 2009.

[26] Adam R Hall, Andrew Scott, Dvir Rotem, Kunal K Mehta, Hagan Bayley, and Cees Dekker. Hybrid pore formation by directed insertion of [alpha]-haemolysin into solid-state nanopores. *Nature nanotechnology*, 5(12):874–877, 2010.

[27] Grégory F Schneider, Stefan W Kowalczyk, Victor E Calado, Grégory Pandraud, Henny W Zandbergen, Lieven MK Vandersypen, and Cees Dekker. Dna translocation through graphene nanopores. *Nano letters*, 10(8):3163–3167, 2010.

[28] Jiali Li, Derek Stein, Ciaran McMullan, Daniel Branton, Michael J Aziz, and Jene A Golovchenko. Ion-beam sculpting at nanometre length scales. *Nature*, 412(6843):166–169, 2001.

[29] A. J. Storm, J. H. Chen, X. S. Ling, H. W. Zandbergen, and C. Dekker. Fabrication of solid-state nanopores with single-nanometre precision. *Nat. Mat.*, 2(8):537–40, aug 2003.

[30] Sang Ryul Park, Hongbo Peng, and Xinsheng S Ling. Fabrication of nanopores in silicon chips using feedback chemical etching. *Small*, 3(1):116–119, 2007.

[31] Langzhou Song, Michael R Hobaugh, Christopher Shustak, Stephen Cheley, Hagan Bayley, and J Eric Gouaux. Structure of staphylococcal α-hemolysin, a heptameric transmembrane pore. *Science*, 274(5294):1859–1865, 1996.

[32] Ian M Derrington, Tom Z Butler, Marcus D Collins, Elizabeth Manrao, Mikhail Pavlenok, Michael Niederweis, and Jens H Gundlach. Nanopore dna sequencing with mspa. *Proceedings of the National Academy of Sciences*, 107(37):16060–16065, 2010.

[33] Complex Trait Consortium et al. The nature and identification of quantitative trait loci: a communitys view. *Nature reviews. Genetics*, 4(11):911, 2003.

[34] Farzin Haque, Jennifer Lunn, Huaming Fang, David Smithrud, and Peixuan Guo. Real-time sensing and discrimination of single chemicals using the channel of phi29 dna packaging nanomotor. *ACS nano*, 6(4):3251–3261, 2012.

[35] David Deamer, Mark Akeson, and Daniel Branton. Three decades of nanopore sequencing. *Nature biotechnology*, 34(5):518–524, 2016.

[36] James Clarke, Hai-Chen Wu, Lakmal Jayasinghe, Alpesh Patel, Stuart Reid, and Hagan Bayley. Continuous base identification for single-molecule nanopore dna sequencing. *Nature nanotechnology*, 4(4):265–270, 2009.

[37] David Wendell, Peng Jing, Jia Geng, Varuni Subramaniam, Tae Jin Lee, Carlo Montemagno, and Peixuan Guo. Translocation of double-stranded dna through membrane-adapted phi29 motor protein nanopores. *Nature nanotechnology*, 4(11):765–772, 2009.

[38] Peng Chen, Toshiyuki Mitsui, Damon B Farmer, Jene Golovchenko, Roy G Gordon, and Daniel Branton. Atomic layer deposition to fine-tune the surface properties and diameters of fabricated nanopores. *Nano letters*, 4(7):1333–1337, 2004.

[39] Bala Murali Venkatesan, Amish B Shah, Jian-Min Zuo, and Rashid Bashir. Dna sensing using nanocrystalline surface-enhanced al2o3 nanopore sensors. *Advanced functional materials*, 20(8):1266–1275, 2010.

[40] Liviu Movileanu, Stefan Howorka, Orit Braha, and Hagan Bayley. Detecting protein analytes that modulate transmembrane movement of a polymer chain within a single protein pore. *Nature biotechnology*, 18(10):1091, 2000.

[41] Stephen Cheley, Li-Qun Gu, and Hagan Bayley. Stochastic sensing of nanomolar inositol 1, 4, 5-trisphosphate with an engineered pore. *Chemistry & biology*, 9(7):829–838, 2002.

[42] Dilani A Jayawardhana, Jeffrey A Crank, Qitao Zhao, Daniel W Armstrong, and Xiyun Guan. Nanopore stochastic detection of a liquid explosive component and sensitizers using boromycin and an ionic liquid supporting electrolyte. *Analytical chemistry*, 81(1):460–464, 2008.

[43] Jeff Nivala, Douglas B Marks, and Mark Akeson. Unfoldase-mediated protein translocation through an [alpha]-hemolysin nanopore. *Nature biotechnology*, 31(3):247–250, 2013.

[44] Shazia Yasin, DG Hasko, and H Ahmed. Fabrication of¡ 5 nm width lines in poly (methylmethacrylate) resist using a water: isopropyl alcohol developer and

ultrasonically-assisted development. *Applied Physics Letters*, 78(18):2760–2762, 2001.

[45] Laurent D Menard and J Michael Ramsey. Fabrication of sub-5 nm nanochannels in insulating substrates using focused ion beam milling. *Nano letters*, 11(2):512–517, 2010.

[46] Stephen Y Chou, Peter R Krauss, and Preston J Renstrom. Nanoimprint lithography. *Journal of Vacuum Science & Technology B: Microelectronics and Nanometer Structures Processing, Measurement, and Phenomena*, 14(6):4129–4133, 1996.

[47] Matthew Colburn, Stephen C Johnson, Michael D Stewart, S Damle, Todd C Bailey, Bernard Choi, M Wedlake, Timothy B Michaelson, SV Sreenivasan, John G Ekerdt, et al. Step and flash imprint lithography: a new approach to high-resolution patterning. In *Microlithography'99*, pages 379–389. International Society for Optics and Photonics, 1999.

[48] Walter Reisner, Jonas N Pedersen, and Robert H Austin. Dna confinement in nanochannels: physics and biological applications. *Reports on Progress in Physics*, 75(10):106601, 2012.

[49] Takashi Ito, Li Sun, and Richard M Crooks. Observation of dna transport through a single carbon nanotube channel using fluorescence microscopy. *Chemical Communications*, (13):1482–1483, 2003.

[50] Haitao Liu, Jin He, Jinyao Tang, Hao Liu, Pei Pang, Di Cao, Predrag Krstic, Sony Joseph, Stuart Lindsay, and Colin Nuckolls. Translocation of single-stranded dna through single-walled carbon nanotubes. *Science*, 327(5961):64–67, 2010.

[51] Reto B Schoch, Jongyoon Han, and Philippe Renaud. Transport phenomena in nanofluidics. *Reviews of modern physics*, 80(3):839, 2008.

[52] RP Abendroth. Behavior of a pyrogenic silica in simple electrolytes. *Journal of Colloid and Interface Science*, 34(4):591–596, 1970.

[53] Patrick Abgrall, Lee-Ngo Low, and Nam-Trung Nguyen. Fabrication of planar nanofluidic channels in a thermoplastic by hot-embossing and thermal bonding. *Lab on a Chip*, 7(4):520–522, 2007.

[54] J Lyklema. Fundamentals of interface and colloid science. volume 2: Solid-liquid interfaces. with special contributions by a. de keizer, bh bijsterbosch, gj fleer and ma cohen stuart. 1995.

[55] Brian J Kirby and Ernest F Hasselbrink. Zeta potential of microfluidic substrates: 1. theory, experimental techniques, and effects on separations. *Electrophoresis*, 25(2):187–202, 2004.

[56] TJ Schmidt, HA Gasteiger, GD Stäb, PM Urban, DM Kolb, and RJ Behm. Characterization of high-surface-area electrocatalysts using a rotating disk electrode configuration. *Journal of The Electrochemical Society*, 145(7):2354–2358, 1998.

[57] Brian J Kirby. *Micro-and nanoscale fluid mechanics: transport in microfluidic devices*. Cambridge University Press, 2010.

[58] Zhijie Sui and Joseph B Schlenoff. Controlling electroosmotic flow in microchannels with ph-responsive polyelectrolyte multilayers. *Langmuir*, 19(19):7829–7831, 2003.

[59] Alexander R Klotz, Lyndon Duong, Mikhail Mamaev, Hendrick W de Haan, Jeff ZY Chen, and Walter W Reisner. Measuring the confinement free energy and effective width of single polymer chains via single-molecule tetris. *Macromolecules*, 48(14):5028–5033, 2015.

[60] Michael E Fisher. Shape of a self-avoiding walk or polymer chain. *The Journal of Chemical Physics*, 44(2):616–622, 1966.

[61] Sam F Edwards et al. *The theory of polymer dynamics*. Oxford Univ. Press, 1986.

[62] Pierre-Gilles de Gennes. Scaling concepts in polymer physics. 1979.

[63] Alexander R Klotz. *DNA Polymer Physics in Complex Nanofluidic Environments*. PhD thesis, McGill University Montreal, Quebec, 2015.

[64] Mathieu Foquet, Jonas Korlach, Warren Zipfel, Watt W Webb, and Harold G Craighead. Dna fragment sizing by single molecule detection in submicrometer-sized closed fluidic channels. *Analytical Chemistry*, 74(6):1415–1422, 2002.

[65] Robert Riehn, Manchun Lu, Yan-Mei Wang, Shuang Fang Lim, Edward C Cox, and Robert H Austin. Restriction mapping in nanofluidic devices. *Proceedings of the National Academy of Sciences of the United States of America*, 102(29):10012–10016, 2005.

[66] YanMei Wang, Jonas O Tegenfeldt, Walter Reisner, Robert Riehn, Xiao-Juan Guan, Ling Guo, Ido Golding, Edward C Cox, James Sturm, and Robert H Austin. Single-molecule studies of repressor–dna interactions show long-range

interactions. *Proceedings of the National Academy of Sciences of the United States of America*, 102(28):9796–9801, 2005.

[67] Walter Reisner, Keith J Morton, Robert Riehn, Yan Mei Wang, Zhaoning Yu, Michael Rosen, James C Sturm, Stephen Y Chou, Erwin Frey, and Robert H Austin. Statics and dynamics of single dna molecules confined in nanochannels. *Physical Review Letters*, 94(19):196101, 2005.

[68] Kyubong Jo, Dalia M Dhingra, Theo Odijk, Juan J de Pablo, Michael D Graham, Rod Runnheim, Dan Forrest, and David C Schwartz. A single-molecule barcoding system using nanoslits for dna analysis. *Proceedings of the National Academy of Sciences*, 104(8):2673–2678, 2007.

[69] Maximilian Haider, Herald Rose, Stephan Uhlemann, Bernd Kabius, and Knut Urban. Towards 0.1 nm resolution with the first spherically corrected transmission electron microscope. *Journal of electron microscopy*, 47(5):395–405, 1998.

[70] Hitachi. Hitachi SU9000 SEM, 2016.

[71] Scott D Russell and Charles P Daghlian. Scanning electron microscopic observations on deembedded biological tissue sections: comparison of different fixatives and embedding materials. *Journal of Electron Microscopy Technique*, 2(5):489–495, 1985.

[72] Fultz Brent and J Howe. Transmission electron microscopy and diffractometry of materials, 2007.

[73] Avetik R Harutyunyan, Gugang Chen, Tereza M Paronyan, Elena M Pigos, Oleg A Kuznetsov, Kapila Hewaparakrama, Seung Min Kim, Dmitri Zakharov, Eric A Stach, and Gamini U Sumanasekera. Preferential growth of single-walled carbon nanotubes with metallic conductivity. *Science*, 326(5949):116–120, 2009.

[74] BJ Kim, J Tersoff, S Kodambaka, MC Reuter, EA Stach, and FM Ross. Kinetics of individual nucleation events observed in nanoscale vapor-liquid-solid growth. *Science*, 322(5904):1070–1073, 2008.

[75] Haimei Zheng, Rachel K Smith, Young-wook Jun, Christian Kisielowski, Ulrich Dahmen, and A Paul Alivisatos. Observation of single colloidal platinum nanocrystal growth trajectories. *Science*, 324(5932):1309–1312, 2009.

[76] James E Evans, Katherine L Jungjohann, Nigel D Browning, and Ilke Arslan. Controlled growth of nanoparticles from solution with in situ liquid transmission electron microscopy. *Nano letters*, 11(7):2809–2813, 2011.

[77] Niels De Jonge, Diana B Peckys, GJ Kremers, and DW Piston. Electron microscopy of whole cells in liquid with nanometer resolution. *Proceedings of the National Academy of Sciences*, 106(7):2159–2164, 2009.

[78] L Marton. La microscopie electronique des objets biologiques. *Bull. Acad. Roy. Med. Belg*, 21:600–617, 1935.

[79] MJ Williamson, RM Tromp, PM Vereecken, R Hull, and FM Ross. Dynamic microscopy of nanoscale cluster growth at the solid–liquid interface. *Nature materials*, 2(8):532–536, 2003.

[80] Hong-Gang Liao, Likun Cui, Stephen Whitelam, and Haimei Zheng. Real-time imaging of pt3fe nanorod growth in solution. *science*, 336(6084):1011–1014, 2012.

[81] Haimei Zheng, Shelley A Claridge, Andrew M Minor, A Paul Alivisatos, and Ulrich Dahmen. Nanocrystal diffusion in a liquid thin film observed by in situ transmission electron microscopy. *Nano letters*, 9(6):2460–2465, 2009.

[82] Utkur Mirsaidov, Claus-Dieter Ohl, and Paul Matsudaira. A direct observation of nanometer-size void dynamics in an ultra-thin water film. *Soft Matter*, 8(27):7108–7111, 2012.

[83] Edward R White, Matthew Mecklenburg, Scott B Singer, Shaul Aloni, and Brian Christopher Regan. Imaging nanobubbles in water with scanning transmission electron microscopy. *Applied Physics Express*, 4(5):055201, 2011.

[84] Dongsheng Li, Michael H Nielsen, Jonathan RI Lee, Cathrine Frandsen, Jillian F Banfield, and James J De Yoreo. Direction-specific interactions control crystal growth by oriented attachment. *Science*, 336(6084):1014–1018, 2012.

[85] Yuning Zhang and Walter Reisner. Fabrication and characterization of nanopore-interfaced nanochannel devices. *Nanotechnology*, 26(45):455301, 2015.

[86] Bala Murali Venkatesan and Rashid Bashir. Nanopore sensors for nucleic acid analysis. *Nat. Nanotech.*, 6:615–624, 2011.

[87] Walter Reisner, Niels B Larsen, Asli Silahtaroglu, Anders Kristensen, Niels Tommerup, Jonas O Tegenfeldt, and Henrik Flyvbjerg. Single-molecule denaturation mapping of dna in nanofluidic channels. *Proceed. Nat. Acad. of Sci. USA*, 107(30):13294–9, jul 2010.

[88] Walter Reisner, Jonas N Pedersen, and Robert H Austin. Dna confinement in nanochannels: physics and biological applications. *Rep. Prog. Phys.*, 75(10):106601, 2012.

[89] Harold Kwok, Kyle Briggs, and Vincent Tabard-Cossa. Nanopore fabrication by controlled dielectric breakdown. *PLos ONE*, 9(3):e92880, 2012.

[90] W. Reisner, N. B. Larsen, H. Flyvbjerg, J. O. Tegenfeldt, and A. Kristensen. Directed self-organization of single dna molecules in a nanoslit via embedded nanopit arrays. *Proced. Nat. Acad. Sci. USA*, 106:79–84, 2009.

[91] Kaimeng Zhou, Michelle L. Kovarik, and Stephen C. Jacobson. Surface-charge induced ion depletion and sample stacking near single nanopores in microfluidic devices. *JACS Communcations*, 130:8614–8616, 2008.

[92] Radin Tahvildari, Eric Beamish, Vincent Tabard-Cossa, and Michel Godin. Integrating nanopore sensors within microfluidic channel arrays using controlled breakdown. *Lab-on-a-Chip*, 15:1407–1411, 2015.

[93] D Pedone, M Langecker, A. M. Munzer, R Wei, R. D. Nagel, and Rant U. Fabrication and electrical characterization of a pore-cavity device. *J. Phys. Condensed Matter*, 22:454115, 2010.

[94] Xu Liu, Mirna Mihovilovic Skanata, and Derek Stein. Entropic cages for trapping dna near a nanopore. *Nat. Comm.*, 6:6222, 2015.

[95] Aleksandar P Ivanov, Emanuele Instuli, Catriona M McGilvery, Geoff Baldwin, David W McComb, Tim Albrecht, and Joshua B Edel. Dna tunneling detector embedded in a nanopore. *Nano Lett.*, 11(1):279–85, January 2011.

[96] H Wang. Low temperature bonding for microfabrication of chemical analysis devices. *Sens. Act. B.*, 45(3):199–207, dec 1997.

[97] Douglas R Tree, Yanwei Wang, and Kevin D Dorfman. Extension of dna in a nanochannel as a rod-to-coil transition. *Physical review letters*, 110(20):208103, 2013.

[98] Daniel Branton, David W Deamer, Andre Marziali, Hagan Bayley, Steven A Benner, Thomas Butler, Massimiliano Di Ventra, Slaven Garaj, Andrew Hibbs, Xiaohua Huang, et al. The potential and challenges of nanopore sequencing. *Nature biotechnology*, 26(10):1146–1153, 2008.

[99] Jay Shendure and Hanlee Ji. Next-generation dna sequencing. *Nature biotechnology*, 26(10):1135–1145, 2008.

[100] Min Jun Kim, Meni Wanunu, David C Bell, and Amit Meller. Rapid fabrication of uniformly sized nanopores and nanopore arrays for parallel dna analysis. *Advanced materials*, 18(23):3149–3153, 2006.

[101] Itaru Yanagi, Rena Akahori, Toshiyuki Hatano, and Ken-ichi Takeda. Fabricating nanopores with diameters of sub-1 nm to 3 nm using multilevel pulse-voltage injection. *Scientific reports*, 4:5000, 2014.

[102] Johan Lagerqvist, Michael Zwolak, and Massimiliano Di Ventra. Fast dna sequencing via transverse electronic transport. *Nano letters*, 6(4):779–782, 2006.

[103] Norcada. Norcada TEM Windows Specification Sheet http://www.norcada.com/wp-content/uploads/2013/07/tem-grid-specsheet.pdf, 2016.

[104] Martin Moskovits. Surface-enhanced spectroscopy. *Reviews of modern physics*, 57(3):783, 1985.

[105] Norihiko Hayazawa, Yasushi Inouye, Zouheir Sekkat, and Satoshi Kawata. Metallized tip amplification of near-field raman scattering. *Optics Communications*, 183(1):333–336, 2000.

[106] Roy S Bass Jr, Arup Bhattacharyya, and Gary D Grise. Non-volatile memory cell having si rich silicon nitride charge trapping layer, September 26 1989. US Patent 4,870,470.

[107] Kyle Briggs, Martin Charron, Harold Kwok, Timothea Le, Sanmeet Chahal, José Bustamante, Matthew Waugh, and Vincent Tabard-Cossa. Kinetics of nanopore fabrication during controlled breakdown of dielectric membranes in solution. *Nanotechnology*, 26(8):084004, 2015.

[108] Cuifeng Ying, Yuechuan Zhang, Yanxiao Feng, Daming Zhou, Deqiang Wang, Yinxiao Xiang, Wenyuan Zhou, Yongsheng Chen, Chunlei Du, and Jianguo Tian. 3d nanopore shape control by current-stimulus dielectric breakdown. *Applied Physics Letters*, 109(6):063105, 2016.

[109] Fu-Chien Chiu. A review on conduction mechanisms in dielectric films. *Advances in Materials Science and Engineering*, 2014, 2014.

[110] RH Fowler and LW Nordheim. Field emission from metallic surfaces. In *Proc. R. Soc. London, Ser. A*, volume 119, pages 173–181, 1928.

[111] M Lenzlinger and EH Snow. Fowler-nordheim tunneling into thermally grown sio2. *Journal of Applied physics*, 40(1):278–283, 1969.

[112] Yee Chia Yeo, Qiang Lu, Wen Chin Lee, Tsu-Jae King, Chenming Hu, Xiewen Wang, Xin Guo, and TP Ma. Direct tunneling gate leakage current in transistors with ultrathin silicon nitride gate dielectric. *IEEE Electron Device Letters*, 21(11):540–542, 2000.

[113] YT Hou, MF Li, Y Jin, and WH Lai. Direct tunneling hole currents through ultrathin gate oxides in metal-oxide-semiconductor devices. *Journal of applied physics*, 91(1):258–264, 2002.

[114] H Sasaki, Mizuki Ono, Takashi Yoshitomi, Tatsuya Ohguro, S-I Nakamura, M Saito, and H Iwai. 1.5 nm direct-tunneling gate oxide si mosfet's. *IEEE Transactions on Electron Devices*, 43(8):1233–1242, 1996.

[115] Myung-Ho Jung, Kwan-Su Kim, Goon-Ho Park, and Won-Ju Cho. Dependence of charge trapping and tunneling on the silicon-nitride (si3n4) thickness for tunnel barrier engineered nonvolatile memory applications. *Applied Physics Letters*, 94(5):3508, 2009.

[116] DJ DiMaria, E Cartier, and D Arnold. Impact ionization, trap creation, degradation, and breakdown in silicon dioxide films on silicon. *Journal of Applied Physics*, 73(7):3367–3384, 1993.

[117] DJ DiMaria, E Cartier, and DA Buchanan. Anode hole injection and trapping in silicon dioxide. *Journal of applied physics*, 80(1):304–317, 1996.

[118] DJ DiMaria. Defect production, degradation, and breakdown of silicon dioxide films. *Solid-State Electronics*, 41(7):957–965, 1997.

[119] James H Stathis. Reliability limits for the gate insulator in cmos technology. *IBM Journal of Research and Development*, 46(2-3):265–286, 2002.

[120] Salvatore Lombardo, James H Stathis, Barry P Linder, Kin Leong Pey, Felix Palumbo, and Chih Hang Tung. Dielectric breakdown mechanisms in gate oxides. *Journal of Applied Physics*, 98(12):121301, 2005.

[121] S Ikonopisov and N Elenkov. Field and temperature dependence of the electronic conduction from electrolytes through the barrier anodic film on niobium. *Journal of Electroanalytical Chemistry and Interfacial Electrochemistry*, 88(3):417–420, 1978.

[122] KC Kalra, KC Singh, and Mohinder Singh. Electrical breakdown of anodic films on titanium in aqueous electrolytes. *Journal of Electroanalytical Chemistry*, 371(1-2):73–78, 1994.

[123] JM Albella, I Montero, and JM Martinez-Duart. A theory of avalanche breakdown during anodic oxidation. *Electrochimica Acta*, 32(2):255–258, 1987.

[124] JH Stathis. Percolation models for gate oxide breakdown. *Journal of applied physics*, 86(10):5757–5766, 1999.

[125] DJ DiMaria. Explanation for the oxide thickness dependence of breakdown characteristics of metal-oxide-semiconductor structures. *Microelectronic engineering*, 36(1-4):317–320, 1997.

[126] WAP Claassen, WGJN Valkenburg, FHPM Habraken, and Y Tamminga. Characterization of plasma silicon nitride layers. *Journal of The Electrochemical Society*, 130(12):2419–2423, 1983.

[127] Zhijun Jiang and Derek Stein. Electrofluidic gating of a chemically reactive surface. *Langmuir*, 26(11):8161–8173, 2010.

[128] ZA Weinberg, MV Fischetti, and Y Nissan-Cohen. Sio2-induced substrate current and its relation to positive charge in field-effect transistors. *Journal of Applied Physics*, 59(3):824–832, 1986.

[129] Klaus F Schuegraf and Chenming Hu. Hole injection sio/sub 2/breakdown model for very low voltage lifetime extrapolation. *IEEE Transactions on Electron Devices*, 41(5):761–767, 1994.

[130] Yee-Chia Yeo, Qiang Lu, and Chenming Hu. Mosfet gate oxide reliability: Anode hole injection model and its applications. *International Journal of High Speed Electronics and Systems*, 11(03):849–886, 2001.

[131] IC Chen, S Holland, KK Young, C Chang, and C Hu. Substrate hole current and oxide breakdown. *Applied physics letters*, 49(11):669–671, 1986.

[132] Klaus F Schuegraf and Chenming Hu. Metal-oxide-semiconductor field-effect-transistor substrate current during fowler–nordheim tunneling stress and silicon dioxide reliability. *Journal of applied physics*, 76(6):3695–3700, 1994.

[133] Robert Entner. *Modeling and simulation of negative bias temperature instability*. na, 2007.

[134] Ih-Chin Chen, S Holland, and C Hu. Electron-trap generation by recombination of electrons and holes in sio2. *Journal of Applied Physics*, 61(9):4544–4548, 1987.

[135] S Chiang, R Wang, T Speers, J McCollum, E Hamdy, and C Hu. Conductive channel in ono formed by controlled dielectric breakdown. In *VLSI Technology, 1992. Digest of Technical Papers. 1992 Symposium on*, pages 20–21. IEEE, 1992.

[136] Takayuki Tomita, Hiroto Utsunomiya, Yoshinari Kamakura, and Kenji Taniguchi. Hot hole induced breakdown of thin silicon dioxide films. *Applied physics letters*, 71(25):3664–3666, 1997.

[137] Javier Martinez, Ramses Valentin Martinez, and Ricardo Garcia. Silicon nanowire transistors with a channel width of 4 nm fabricated by atomic force microscope nanolithography. *Nano letters*, 8(11):3636–3639, 2008.

[138] Ricardo Garcia, Ramses V Martinez, and Javier Martinez. Nano-chemistry and scanning probe nanolithographies. *Chemical Society Reviews*, 35(1):29–38, 2006.

[139] Phaedon Avouris, Tobias Hertel, and Richard Martel. Atomic force microscope tip-induced local oxidation of silicon: kinetics, mechanism, and nanofabrication. *Applied Physics Letters*, 71(2):285–287, 1997.

[140] Wayne Yang, Yuning Zhang, Michael Hilke, and Walter Reisner. Dynamic imaging of au-nanoparticles via scanning electron microscopy in a graphene wet cell. *Nanotechnology*, 26(31):315703, 2015.

[141] C Ackerley, C Nielsen, and C Hawkins. Experiences with wet capsule imaging exploring the potential for live cell imaging. *Microscopy and Microanalysis*, 12(S02):428–429, 2006.

[142] Masahiko Ishii, Hiroshi Nakamura, Hideyuki Nakano, Azusa Tsukigase, and Masashi Harada. Large-domain colloidal crystal films fabricated using a fluidic cell. *Langmuir*, 21(12):5367–5371, 2005.

[143] Wenxin Niu, Ling Zhang, and Guobao Xu. Seed-mediated growth of noble metal nanocrystals: crystal growth and shape control. *Nanoscale*, 5(8):3172–3181, 2013.

[144] Andrei Kolmakov, Dmitriy A Dikin, Laura J Cote, Jiaxing Huang, Majid Kazemian Abyaneh, Matteo Amati, Luca Gregoratti, Sebastian Günther, and Maya Kiskinova. Graphene oxide windows for in situ environmental cell photoelectron spectroscopy. *Nature nanotechnology*, 6(10):651–657, 2011.

[145] Tetsuya Tsuda, Noriko Nemoto, Koshi Kawakami, Eiko Mochizuki, Shoko Kishida, Takako Tajiri, Toshihiro Kushibiki, and Susumu Kuwabata. Sem observation of wet biological specimens pretreated with room-temperature ionic liquid. *ChemBioChem*, 12(17):2547–2550, 2011.

[146] A Bogner, P-H Jouneau, Gilbert Thollet, D Basset, and Catherine Gauthier. A history of scanning electron microscopy developments: towards wet-stem imaging. *Micron*, 38(4):390–401, 2007.

[147] Livio Muscariello, Francesco Rosso, Gerardo Marino, Antonio Giordano, Manlio Barbarisi, Gennaro Cafiero, and Alfonso Barbarisi. A critical overview of esem applications in the biological field. *Journal of cellular physiology*, 205(3):328–334, 2005.

[148] D Peckys, U Werner, and N de Jonge. Detection of epidermal growth factor receptor dimers on wet and intact eukaryotic cells in an environmental scanning electron microscope. *Microscopy and Microanalysis*, 19(S2):138–139, 2013.

[149] Athene M Donald. The use of environmental scanning electron microscopy for imaging wet and insulating materials. *Nature materials*, 2(8):511–516, 2003.

[150] Li Yang, Zihua Zhu, Xiao-Ying Yu, Eugene Rodek, Lax Saraf, Theva Thevuthasan, and James P Cowin. In situ sem and tof-sims analysis of igg conjugated gold nanoparticles at aqueous surfaces. *Surface and Interface Analysis*, 46(4):224–228, 2014.

[151] Christina Mueller, Maher Harb, Jason R Dwyer, and RJ Dwayne Miller. Nanofluidic cells with controlled pathlength and liquid flow for rapid, high-resolution in situ imaging with electrons. *The Journal of Physical Chemistry Letters*, 4(14):2339–2347, 2013.

[152] Stephan Thiberge, Amotz Nechushtan, David Sprinzak, Opher Gileadi, Vered Behar, Ory Zik, Yehuda Chowers, Shulamit Michaeli, Joseph Schlessinger, and Elisha Moses. Scanning electron microscopy of cells and tissues under fully hydrated conditions. *Proceedings of the National Academy of Sciences of the United States of America*, 101(10):3346–3351, 2004.

[153] Birgit Päivänranta, Andreas Langner, Eugenie Kirk, Christian David, and Yasin Ekinci. Sub-10 nm patterning using euv interference lithography. *Nanotechnology*, 22(37):375302, 2011.

[154] Matthias Firnkes, Daniel Pedone, Jelena Knezevic, Markus Doblinger, and Ulrich Rant. Electrically facilitated translocations of proteins through silicon nitride nanopores: conjoint and competitive action of diffusion, electrophoresis, and electroosmosis. *Nano letters*, 10(6):2162–2167, 2010.

[155] Daniel R Cooper, Benjamin DAnjou, Nageswara Ghattamaneni, Benjamin Harack, Michael Hilke, Alexandre Horth, Norberto Majlis, Mathieu Massicotte, Leron Vandsburger, and Eric Whiteway. Experimental review of graphene. *International Scholarly Research Notices*, 2012, 2012.

[156] Hidetoshi Nishiyama, Mitsuo Suga, Toshihiko Ogura, Yuusuke Maruyama, Mitsuru Koizumi, Kazuhiro Mio, Shinichi Kitamura, and Chikara Sato. Atmospheric scanning electron microscope observes cells and tissues in open medium through silicon nitride film. *Journal of structural biology*, 169(3):438–449, 2010.

[157] Mark Krueger, Shannon Berg, DArcy Stone, Evgheni Strelcov, Dmitriy A Dikin, Jaemyung Kim, Laura J Cote, Jiaxing Huang, and Andrei Kolmakov. Drop-casted self-assembling graphene oxide membranes for scanning electron microscopy on wet and dense gaseous samples. *ACS nano*, 5(12):10047–10054, 2011.

[158] Xuesong Li, Weiwei Cai, Jinho An, Seyoung Kim, Junghyo Nah, Dongxing Yang, Richard Piner, Aruna Velamakanni, Inhwa Jung, and Emanuel Tutuc. Large-area synthesis of high-quality and uniform graphene films on copper foils. *Science*, 324(5932):1312–1314, 2009.

[159] Mathieu Massicotte, Victor Yu, Eric Whiteway, Dan Vatnik, and Michael Hilke. Quantum hall effect in fractal graphene: growth and properties of graphlocons. *Nanotechnology*, 24(32):325601, 2013.

[160] V Yu, E Whiteway, J Maassen, and M Hilke. Raman spectroscopy of the internal strain of a graphene layer grown on copper tuned by chemical vapor deposition. *Physical Review B*, 84(20):205407, 2011.

[161] Prashant K Jain, Ivan H El-Sayed, and Mostafa A El-Sayed. Au nanoparticles target cancer. *nano today*, 2(1):18–29, 2007.

[162] Bernd Winter and Manfred Faubel. Photoemission from liquid aqueous solutions. *Chemical reviews*, 106(4):1176–1211, 2006.

[163] Pinshane Y Huang, Carlos S Ruiz-Vargas, Arend M van der Zande, William S Whitney, Mark P Levendorf, Joshua W Kevek, Shivank Garg, Jonathan S Alden, Caleb J Hustedt, and Ye Zhu. Grains and grain boundaries in single-layer graphene atomic patchwork quilts. *Nature*, 469(7330):389–392, 2011.

[164] SM Moghimi and J Szebeni. Stealth liposomes and long circulating nanoparticles: critical issues in pharmacokinetics, opsonization and protein-binding properties. *Progress in lipid research*, 42(6):463–478, 2003.

[165] Srigokul Upadhyayula, Timothy Quinata, Stephen Bishop, Sharad Gupta, Noah Ray Johnson, Baharak Bahmani, Kliment Bozhilov, Jeremy Stubbs, Pamela Jreij, and Pratima Nallagatla. Coatings of polyethylene glycol for suppressing adhesion between solid microspheres and flat surfaces. *Langmuir*, 28(11):5059–5069, 2012.

[166] Yung-Chang Lin, Chun-Chieh Lu, Chao-Huei Yeh, Chuanhong Jin, Kazu Suenaga, and Po-Wen Chiu. Graphene annealing: how clean can it be? *Nano letters*, 12(1):414–419, 2011.

[167] Vidya Kochat, Atindra Nath Pal, ES Sneha, Arjun Sampathkumar, Anshita Gairola, SA Shivashankar, Srinivasan Raghavan, and Arindam Ghosh. High contrast imaging and thickness determination of graphene with in-column secondary electron microscopy. *Journal of Applied Physics*, 110(1):014315, 2011.

[168] Marijke Welvaert and Yves Rosseel. On the definition of signal-to-noise ratio and contrast-to-noise ratio for fmri data. *PloS one*, 8(11):e77089, 2013.

[169] Michael H Nielsen, Shaul Aloni, and James J De Yoreo. In situ tem imaging of caco3 nucleation reveals coexistence of direct and indirect pathways. *Science*, 345(6201):1158–1162, 2014.

[170] Jeanne Ayache, Luc Beaunier, Jacqueline Boumendil, Gabrielle Ehret, and Danièle Laub. *Sample preparation handbook for transmission electron microscopy: techniques*, volume 2. Springer Science & Business Media, 2010.

[171] Marvin G Warner and James E Hutchison. Linear assemblies of nanoparticles electrostatically organized on dna scaffolds. *Nature materials*, 2(4):272–277, 2003.

[172] Jan Bednar, Patrick Furrer, Vsevolod Katritch, Alicja Stasiak, Jacques Dubochet, and Andrzej Stasiak. Determination of dna persistence length by cryo-electron microscopy. separation of the static and dynamic contributions to the apparent persistence length of dna. *Journal of molecular biology*, 254(4):579–594, 1995.

[173] C Bouchiat, MD Wang, J-F Allemand, T Strick, SM Block, and V Croquette. Estimating the persistence length of a worm-like chain molecule from force-extension measurements. *Biophysical journal*, 76(1):409–413, 1999.

[174] Daniel Sage, Franck R Neumann, Florence Hediger, Susan M Gasser, and Michael Unser. Automatic tracking of individual fluorescence particles: application to the study of chromosome dynamics. *IEEE Transactions on Image Processing*, 14(9):1372–1383, 2005.

[175] Loukas Vlahos, Heinz Isliker, Yannis Kominis, and Kyriakos Hizanidis. Normal and anomalous diffusion: A tutorial. *arXiv preprint arXiv:0805.0419*, 2008.

[176] Jingyu Lu, Zainul Aabdin, N Duane Loh, Dipanjan Bhattacharya, and Utkur Mirsaidov. Nanoparticle dynamics in a nanodroplet. *Nano letters*, 14(4):2111–2115, 2014.

[177] Yingxi Zhu and Steve Granick. Viscosity of interfacial water. *Physical Review Letters*, 87(9):096104, 2001.

[178] Jianping Gao, Robert Szoszkiewicz, Uzi Landman, Elisa Riedo, et al. Structured and viscous water in subnanometer gaps. *Physical Review B*, 75(11):115415, 2007.

[179] KB Jinesh and JWM Frenken. Capillary condensation in atomic scale friction: how water acts like a glue. *Physical review letters*, 96(16):166103, 2006.

[180] Hong-Gang Liao and Haimei Zheng. Liquid cell transmission electron microscopy. *Annual review of physical chemistry*, 67:719–747, 2016.

[181] Building a better nanopore. *Nat Nano*, 11(2):105–105, Feb 2016. Editorial.